Coherent Probes of Strong Field Atomic Dynamics

A Thesis Presented

by

Uvo Christoph Hölscher

to

The Graduate School

in Partial Fulfillment of the Requirements

for the Degree of

Master of Arts

in

Physics

Stony Brook University

August 2008

Stony Brook University

The Graduate School

Uvo Christoph Hölscher

We, the Thesis committee for the above candidate for the Master of Arts degree, hereby recommend acceptance of the Thesis.

Thomas C. Weinacht, Thesis Advisor

Assistant Professor, Department of Physics and Astronomy

Thomas H. Bergeman, Chairperson of Defense

Adjunct Professor, Department of Physics and Astronomy

Axel K. Drees

Professor, Department of Physics and Astronomy

Harold J. Metcalf

Professor, Department of Physics and Astronomy

This Thesis is accepted by the Graduate School.

Lawrence Martin

Dean of the Graduate School

Abstract of the Thesis

Coherent Probes of Strong Field Atomic Dynamics

by

Uvo Christoph Hölscher

Master of Arts

in

Physics

Stony Brook University

2008

The work presented in this thesis studies the effect of ultrafast electromagnetically induced transparency (EIT) in a time domain picture. We demonstrate that ultrafast EIT is not only a version of CW laser EIT experiments scaled in time and field strength but shows a new dynamic. Time dependent Rabi frequencies of the light fields in conjunction with a short interaction time cause a suppression of absorption at the transition frequency and a redistribution of light among the spectrum.

A second experiment in the thesis discusses excitation mechanisms like adiabatic rapid passage (ARP) for a four level system. We demonstrate a strong chirp dependence of the excitation paths and explain the behavior in the dressed states picture. The preparation of the system leads to a collective emission of excited atoms called superfluorescence. We study the phenomenon and measure its characteristics.

To Julia and my Family

Contents

List of Figures

List of Tables

Acknowledgements

I am very glad to have a long list of persons I need to thank for their support and help during the last year.

First of all I owe great a debt of gratitude to Tom my advisor, theoretician, partner for discussion, helping hand and much more. I will never forget these moments when he was standing on the blackboard - a kind of enthusiasm in his eyes - and pointing out the quintessence of your measurement. I will never forget these moments when he came into the lab at 11pm and was helping to the take the right data. I will never forget these moments when he was finding the right words to squeeze out at least one positive aspect of every failed experiment. Thank you Tom for having gone through all the ups and downs of research with me, for your extraordinary class on quantum electronics and all your support, encouragement and expertise during my work.

Steve was a great help for me to get my hands dirty on the experiments in the first days. He has introduced me to all the secrets of ultrafast lasers which you cannot find in books and articles but have to learn by doing. We have spend some of these famous long nights in the lab trying our best to get the sodium to lase. We have spend hours and hours on the blackboard discussing back and forth many topics we both work on.

I also owe my warmest thanks to the other group members who have always helped out with words and deeds. Sarah has been there for advice on every single part of the laser. Coco has helped me a lot with my LabVIEW code and the spectrometers. Dominik and Marija have fixed the laser with me during long days of disassembling and assembling the amplifier. And finally Seth has debugged the software to automate the data runs. Not to forget Marty whose decades of experience have solved so many problems.

Furthermore I need to acknowledge many others who have not been in the lab but have their share in my work as well. My girlfriend Julia has been there for me with her never ending love and her great support throughout the whole time. She has helped me overcoming many ups and downs in life. I am particularly thankful for her appreciation of me spending a year abroad and

leaving her in Germany. My parents and my sister have been always there to talk to and have brought my home a little closer to Stony Brook. Thank your for those wonderful hours in Skype. I have always been astonished when talking to my grandparents how much interest they have shown in my progress and I really appreciate their support. Furthermore I like to acknowledge my roommate Simon. We have spent some great time here in the US and will continue so.

There are some persons and institutions in Germany who have made possible my studies abroad. First of all I want to thank Prof. Assaad and the Julius-Maximilian-Universität Würzburg for their support of the exchange program and their connections to Stony Brook. The DAAD has helped me to overcome the financial burdens of my studies.

Here in Stony Brook I have experienced great support from Laszlo, Pat and Sara. Thank your for all your work around research and classes. I also want to acknowledge the AMO group for being such a friendly community and giving so much inspiration.

Chapter 1

Introduction

The development of ultrafast lasers opened a new magnificent field for physics and chemistry. Research groups throughout the whole world in the atomic, molecular and optical community are carrying out experiments to explore the regime of ultrafast and intense light-matter interaction. Since significant progress with broadband Ti:Sapphire lasers in the 1990s [39, 40] the manifold applications of short light pulses have introduced a whole new field of studies. With Ahmed H. Zewail's Nobel prize for femtosecond spectroscopy chemistry in 1999 ultrafast phenomena gained public interest.

Laser pulses in the femtosecond regime provide an excellent tool for time resolved experiments in a huge field of applications. Their extremely short durations establish the possibility of monitoring atomic and molecular dynamics and chemical reactions. Many processes like vibrational evolution of a molecule and changes in molecule structure take place on time scales of 100s of femtoseconds or a few picoseconds and can be optimally explored by short femtosecond laser pulses. Other processes such as spectral collisional broadening are of comparable time scale or even much longer like in the case of spontaneous emission.

Optical laser amplifiers are able to produce field strengths on the order of several 10^8V/m which is orders of magnitude higher than in usual CW applications. For many experiments ultrafast lasers provide the potential to exceed the limits of the weak field regime which is described by perturbation theory. High field strengths have opened the possibilities to absorb multiple photons, drive non-linear interactions and strongly influence energy levels of atoms and molecules.

The shorter the laser pulses the stronger arose the need for elaborate time measuring and shaping techniques. Many different devices have been developed [2, 24, 38, 47] to use autocorrelation of the pulse to determine its field and phase in time. Pulse shapers [14] increased the variety of possible experiments with ultrafast pulses even more.

A new way of influence arises from coherent processes [45]. Controlling interference between different excitation paths with the phase of the light field yields new means to prepare systems. Selective use of absorption and stimulated emission leads to a powerful tool to tailor the interaction of light field and matter.

Various experiments reveal new characteristics when carried over from the weak field to strong field regime as assumptions and approximations do not hold true any more. New dynamics like non-resonant absorption in multiphoton processes, splittings and shifts in quantum mechanical states and nonlinear responses occur.

The aim of my work presented in this thesis is the understanding of two experiments influenced by strong field atomic dynamics:

Electromagnetically induced transparency (EIT) has only been studied so far in the weak field regime. We concentrate on a time domain perspective and explore the dynamics arising from a time dependent amplitude of fields and Rabi frequencies. Additionally ultrashort pulses allow to study EIT with a dephasing time much longer than the excitation.

Superfluorescence is a coherent, collective response of an excited system of atoms. Our measurements reveal insight into the mechanisms of coherent strong field multiphoton absorption leading to highly populated states. The excited system develops a macroscopic dipole moment and induces strong lasing.

Chapter 2 about the Experimental Setup introduces the reader to general devices used in experiments in this thesis. Pulse generation with its different stages, pulse shaping and characterization are discussed in basic terms. The section on characterization leads over to chapter 3 about the GRENOUILLE. Configuration and calibration of this time measurement device have been carried out in the beginning of the work in the group.

Chapter 4 on the Theoretical Background discusses in detail the theoretical fundamentals for EIT and strong field excitation mechanisms. It focuses on two-level atoms and the dressed state picture presenting the basis for a three-level picture of EIT.

The main work of my thesis is discussed in chapter 5 about EIT in rubidium. Starting from the properties of rubidium and EIT in the weak field

regime we approach the case of EIT in the strong field regime. The setup of the experiment is discussed with an section on the Pulse Applicator Program. A simulation for EIT as three-level system gives insight into the dynamics of the population in the system. We present our results and analyze them.

Chapter 6 on broadband excitation in Rb presents further experiments carried out on rubidium. We observe strong coherent light at three different transitions at 420 nm, 780 nm and 795 nm to the ground state. The underlying dynamics are explained in the interaction picture. The last two chapters 7 and 8 give a perspective on Future Work and conclude the thesis.

Chapter 2

Experimental Setup

This chapter describes the various parts of the experimental apparatus. The setup can be divided into several functional groups which comprise the generation of pulses, the shaping of pulses, the characterization of pulses and the rubidium cell.

2.1 Pulse Generation

The generation of the pulses is based on a Ti:Sapphire laser system emitting pulses with durations down to 30 fs and with an average energy of 1 mJ. A broad bandwidth of the gain medium in combination with mode locking of many frequencies is key to obtain the desired ultra short pulses. The setup is made up of two components: The oscillator produces the pulses and sends them to the amplifier which increases the energy of single pulses by a factor of approximately 10^6.

To obtain the required broadband lasing the oscillator uses a Ti:Sapphire crystal which is known for its tunability and its broad emission spectrum. Pumped with a 532 nm green ©Verdi5 laser the crystal lases around 780 nm with 50 nm bandwidth. The central frequency of the oscillator can be tuned within a range of more than 10 nm. The resulting pulses with the repetition rate of 85 kHz are short and weak in energy.

Mode locking of the frequencies implies a fixed phase relationship between all modes of the broad spectrum. To obtain this a dispersion control setup of two prisms is introduced into the beam path. They compensate for all dispersive effects in the cavity such that the phase relation between different frequencies stays constant. In conjunction with the phase control a self focusing effect in the crystal (Kerr effect) suppresses the constant wave (CW) modes

in favor of the mode locked (ML) operation. Due to the higher intensities in pulses the self focusing effect is much stronger in ML than in CW.

Two mirrors of the cavity are curved and guide the beam in its spatial mode. In addition to the radii of the mirrors the extra focusing effect of the ML operation of the crystal is taken into account. This results in a perfectly matched cavity for ML. In contrast in the CW operation the mirrors will be too far apart and hence the quality factor is smaller and favors a stable ML operation.

A Pockels cell with a 1 kHz repetition rate picks out pulses from the oscillator output and sends them to the amplifier.

To decrease the peak intensity of the light in the amplifying crystal the pulses are stretched in time before they enter the gain setup. A stretcher increases the temporal width of the pulse. The process is a dispersion control which introduces a temporal phase into the pulses. This causes the time duration of the pulse to prolong and hence the peak intensity to decrease. A combination of dispersive gratings, curved mirrors and a retro reflector allows us to create a chirp (see chapter 3.1 about chirped pulses) without having a spread in k-vectors for different frequencies. After the amplification a similar compressor, reversing the effect, removes the chirp and brings the pulses to their original temporal width.

The gain setup is a multi pass amplifier pumped by a pulsed ©Quantronix YLF laser. It increases the pulse energy of a single pulse up to 1 mJ within 12 amplification passes through the crystal. The seed pulses from the oscillator travel through a ring cavity with a slightly displaced path for every pass. This leads to a fan of beams which all intersect in the active region of the amplification crystal. The last pass in this ring cavity falls onto a pick up mirror and is sent to the compressor.

In every pass the seed travels through a crystal region with high inversion and hence is multiplied in its energy. The spectral response of this process is not flat and power dependent so that the spectrum's shape slightly changes. A pellicle in the ring cavity can partly compensate as it acts as band filter. Good alignment of the multi pass and proper spatial and temporal overlap of pump and seed beam are critical for operation.

After the complete amplification the resultant pulse has almost a Gaussian shape in time with a FWHM of 30 fs and a flat spectral phase. It can be directed to following various setups like pulse measurements, experiments or pulse shaper. A more detailed description of the amplifier is given by Kapteyn and Murnane [5, 6].

2.2 Pulse Shaping

An acousto-optical modulator (AOM) is used for shaping the pulses. One general problem in ultrafast optics is that no electrical or mechanical physical effects is fast enough to measure or change the pulses in the time domain. Therefore the principle of the pulse shaping is based on manipulation of the pulse in the frequency domain. A good introduction to the setup and theory is given by Warren *et al.* [14]. Short pulses are hence mapped to the frequency domain, where they can be handled and manipulated much easier.

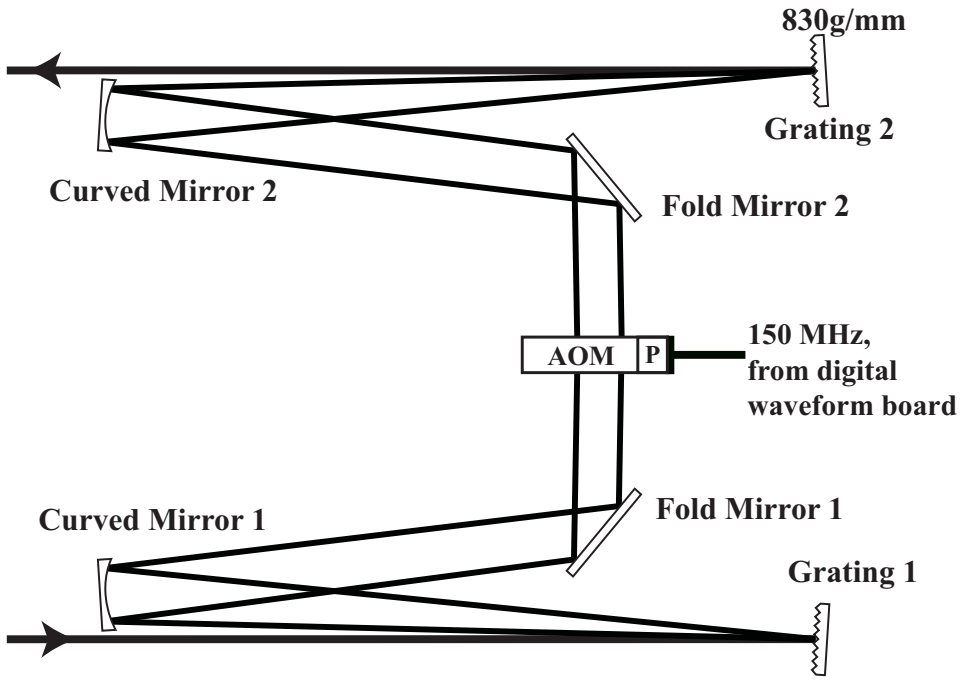

Figure 2.1: Scheme of a Pulse Shaper Setup. The beam is decomposed by the first grating and mapped onto the acousto-optical modulator where it is shaped. The diffracted beam is recomposed in opposite way.

The beam in the shaper is steered onto a grating (830 grooves/mm) which decomposes the pulse into its frequencies. A following curved mirror collimates the dispersed beam and focuses it into the AOM which is placed exactly in the Fourier plane of the setup. The acousto-optical modulator is a crystal in which an acoustic wave is induced at one side by a high frequency signal. The

wave runs through the crystal and alternates the local index of refraction. By the time the laser pulse arrives the crystal, the wave has created a pattern of regions of higher and lower index of refraction which diffract the incoming beam. This process can be described as Bragg diffraction at an object which is in motion. Detailed calculation on the process can by found in Boyd [8].

The velocity of the acoustic wave is so slow in comparison to the short pulse that the propagation during the passage of the light is neglectable. Nevertheless energy and momentum conservation have to hold true. Hence the diffracted beam will change its frequency, amplitude, k-vector and phase.

Working with acoustic waves around 150 MHz the light frequency is only changed by a small amount which does not play any role in the broadband regime. The amplitude of the diffracted light is to first order proportional to the amplitude of the acoustic wave. This will allow us to tailor the intensity of every single frequency by varying the acoustic wave's amplitude in time.

The phase $\Phi(t)$ of a sinusoidal signal is the non constant part of the temporal derivative of the argument of a function

$$f(t) = \sin(\omega_t \cdot t) \tag{2.2.1}$$

$$\omega_t = \omega_0 + \Phi(t) \tag{2.2.2}$$

In the AOM every frequency is diffracted by a specific part of the acoustic wave in the crystal. The phase of a diffracted frequency is proportional to the phase of the corresponding part of the acoustic wave. Hence a spectral phase of the pulse can be tailored by the phase of the high frequency signal. The detailed mechanism is discussed with the introduction of a linear phase in chapter 5.5 about the Pulse Applicator. The influence of phases on the pulses is treated in chapter 3.1.

The limits of the process are mainly given by technical constraints. The crystal's diffraction efficiency is optimal for the carrier frequency of 150 MHz and falls off for higher and lower frequencies. Additionally the optical diffraction limit of the setup restricts the minimal bandwidth for a shaped pulse. Results are shown in chapter 5.5. Conservation of momentum determines that beams with different phase acquired slightly diverge. The effect is called space time coupling. Overall efficiencies up to 36% have been recorded. Changes in the phase can be put on reliable up to a linear phase of 20 ps and quadratic chirp rates of about $0.02\,\mathrm{ps}^2$.

It is hard to imagine how of a complex amplitude and phase shaping will influence the temporal shape of the electric field. The mathematical description is the Fourier transformation of the pulse into the frequency domain, following manipulation of the frequencies and inverse Fourier transformation.

The signal for the acoustic wave is created by an arbitrary waveform generator and can be modulated in amplitude and phase by various computer programs. From this implementation arises a broad variety of shaping techniques like chirp scans, π-phase-scans and genetic algorithms.

2.3 Pulse Characterization

Pulse characterization is the process of retrieving the electric field and the phase of the pulse in time and frequency. This task is done by a FROG [47] and a GRENOUILLE [2]. Detailed information on the principles of pulse measurement is given in the following chapter Configuration and Calibration of the GRENOUILLE 3.

The GRENOUILLE usually is used for fast monitoring of the pulse attributes. Its temporal resolution is not as high as the FROG but it reveals enough information to roughly decide on the pulse quality. The main advantage is that its alignment is very simple and the signal processing happens in real time. For reasons mentioned later and missing reconstruction software the phase cannot be retrieved by the GRENOUILLE.

The FROG is used for more precise measurements of phase and electric field. Up to a certain pulse complexity its results are robust and reliable. The alignment process is crucial and the data taking time consuming. It is mainly used to characterize pulses tailored in the pulse shaper.

Chapter 3

Configuration and Calibration of the GRENOUILLE

The characterization of intensity and phase of an ultra short laser pulse is a challenge. Since 1993 a multitude of technologies to measure fs-pulses have been introduced like the FROG [47], SPIDER [38], MIIPS [24] and GRENOUILLE [2]. As mentioned earlier, conventional techniques are not able to resolve temporal structures in the fs-regime. The only measure which is available on the same timescale is the pulse itself, hence all characterization methods are based on nonlinear optics.

The first two sections of this chapter introduce to the mathematical background of chirped pulses and the general way an autocorrelation measurement is carried out. In the following the exact mechanism of the GRENOUILLE is explained in detail. The last section reports on the calibration of the GRENOUILLE device.

3.1 Chirped Pulses

It is convenient to describe the electric field of a pulse in such a way that the wave is formed by an envelope which jackets the oscillations. The advantages of this formalism are obviously its easy mathematical description and the separation of average amplitude and instantaneous frequency.

Short light pulses are superpositions of many different frequencies. For a few cycles (in the fs-regime) these frequencies add constructively and form the pulse whereas for most of the time the frequencies add destructively. This mechanism to generate short pulses is called phase matching.

For optimal short pulse durations the overall spectral phase has to be constant. This means that all different frequencies will add up perfectly in the

temporal middle of the pulse. The result is an electric field which oscillates at one constant carrier frequency during the whole pulse duration. Such an optimal pulse has a Gaussian shape. This property can be proven by Fourier transforming a normal distribution of frequencies with constant phase. The widths of the two distributions in frequency and time domain is reciprocal and their product constant respectively (for Gaussian pulses: $\Delta\omega \cdot \Delta t \approx 0.44$).

In practice the overall phase is never perfectly flat such that the oscillations change their frequency during the pulse. The underlying carrier frequency of the field envelope is not constant any more. The reason is that every passage of light through matter adds dispersion to the pulse. Dispersion is caused by an index of refraction which depends on the frequencies. This results in quadratic and higher order spectral phase causing the carrier frequency of the pulse to change in time.

Assuming a Gaussian pulse with flat phase the field is

$$E(t) = E_0 \exp(-i\omega_0 t) \exp(-gt^2) \tag{3.1.1}$$

where the factor g describes its temporal width.

The corresponding spectrum is the Fourier transform with the carrier frequency ω_0

$$E(\omega) = \mathfrak{F}(E(t)) = E_0 \sqrt{\frac{\pi}{\alpha}} \exp\left[-\frac{(\omega-\omega_0)^2}{4\alpha}\right] \tag{3.1.2}$$

Dispersion occurs as linear and higher order phase dependency of the frequency. For linear dispersion the inverse Fourier transformation of the pulse results in a uniform displacement in time. This is easy to understand as all frequencies are retarded by the same amount of phase in the media.

The linear phase is introduced as imaginary term

$$\tilde{E}(\omega) = E_0 \exp\left[-i\tau(\omega+\omega_0)\right] \sqrt{\frac{\pi}{\alpha}} \exp\left[-\frac{(\omega-\omega_0)^2}{4\alpha}\right] \tag{3.1.3}$$

where τ is the displacement in time.

For higher orders like quadratic dispersion (so called chirp) the frequencies change their relative phase. The resulting field in the time domain shows two characteristics. As mentioned before the quadratic chirp causes the carrier frequency to change during the pulse duration from higher to lower frequencies (or the other way round). Furthermore the temporal width of the pulse broadens. In general the amplitude of the field becomes complex.

(a) (b)

Figure 3.1: Influences of Linear Phase on a Gaussian Pulse. The original Gaussian pulse (a) is centered at $t = t_0$ whereas the pulse with linear phase (b) is shifted in time and is centered at $t = t_0 + \tau$.

The quadratic phase is introduced similarly

$$\tilde{E}(\omega) = E_0 \exp\left[-i\beta(\omega+\omega_0)^2\right] \sqrt{\frac{\pi}{\alpha}} \exp\left[-\frac{(\omega+\omega_0)^2}{4\alpha}\right] \tag{3.1.4}$$

where β is called the spectral chirp rate.

The inverse Fourier transform gives the resulting field

$$E(t) = E_0' \exp\left[-i(\omega_0 t + bt^2)\right] \exp(-at^2) \tag{3.1.5a}$$

$$E_0' = E_0 \sqrt{\frac{1}{1+i4\alpha\beta}} \tag{3.1.5b}$$

$$a = \frac{\alpha}{1+16\alpha^2\beta^2} \tag{3.1.5c}$$

$$b = -\frac{4\alpha^2\beta}{1+16\alpha^2\beta^2} \tag{3.1.5d}$$

The parameter α describes the width of the spectrum (comp. 3.1.4) and the parameter β is a measure of quadratic change in spatial phase leading to a non constant carrier frequency. Depending on the sign of the chirp rate β the frequency sweep starts at higher or lower frequencies. The pulse duration as a function of β is

$$\Delta t' = \sqrt{1+16\alpha^2\beta^2}\ \Delta t \tag{3.1.6}$$

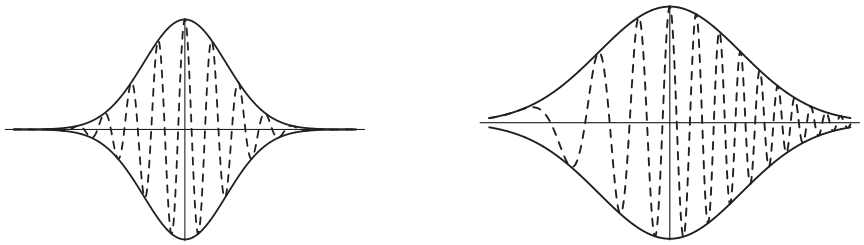

(a) (b)

Figure 3.2: Influences of Quadratic Phase on a Gaussian Pulse. The original Gaussian pulse (a) is has the shortest time duration. A quadratic chirp broadens the pulse (b) in the time domain and causes the carrier frequency to change during the pulse.

3.2 Pulse Characterization Background

The characterization of an ultra short laser pulse is a challenge. As mentioned earlier, conventional techniques are not able to resolve temporal structures in the fs -regime. The only measure which is available on this timescale is the pulse itself, hence all characterization methods are based on nonlinear optics.

Autocorrelation is the process of "comparing" a signal with some processed copy of itself. In most cases the processing is a simple shift in time so that the autocorrelation function $A(\tau)$ could be defined as

$$A(\tau) = \int f(t) \cdot f(t+\tau) dt \tag{3.2.1}$$

The Wiener-Khinchin theorem relates the autocorrelation to the power spectral density $\rho(\omega)$ via Fourier transformation:

$$A(\tau) = \mathfrak{F}(\rho(\omega)) \tag{3.2.2}$$

In an experimental apparatus this equation could be satisfied by splitting a beam in a beam splitter, shifting one beam in time by a variable path length and creating a second harmonic signal in a nonlinear optic (compare figure 3.3).

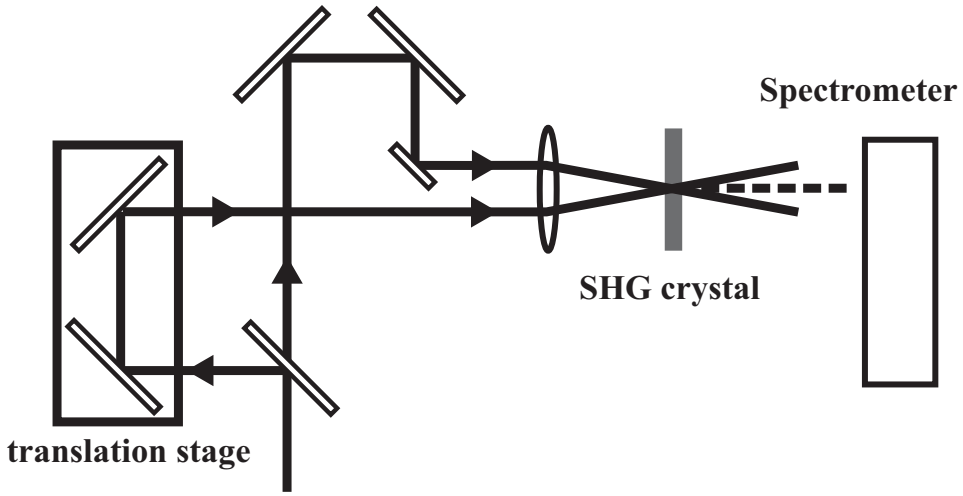

Figure 3.3: Schematic Drawing of FROG Setup. The light is split by a beam splitter and travels different path lengths due to the translation stage. In the crystal the recombined beams produces a SHG signal measured by a spectrometer.

Nonlinear responses like second harmonic generation (SHG) are proportional to the intensity of the mixed signal which is the sum of the two merged beams $I \propto |E_a + E_b|^2 = |E_a|^2 + |E_b|^2 + 2|E_a \cdot E_b|$. When the cooperative signal ($|E_a \cdot E_b|$) can be separated its intensity will be proportional to $|E(t) \cdot E(t-\tau)|$ which is the needed quantity.

The signal is measured with a spectrometer. Scanning the parameters delay time τ and frequency ω results in a two dimensional (τ, ω) trace which contains all information about intensity and phase of the pulse. The resulting data reads:

$$S(\omega, \tau) \propto \left| \int E(t)E(t-\tau)e^{i\omega t}dt \right|^2 \tag{3.2.3}$$

Several different mathematical algorithms can retrieve the pulse by iteration of Fourier transformations between time and frequency domains. The mathematical discussion is very complex and can be found in [47].

Many different technical realizations have been build. The first and maybe best known is the FROG[1] [47]. Further modified approaches follow the "naming convention" and are called GRENOUILLE[2] [2], SPIDER[3] [38] and MIIPS[4] [24].

The configuration and calibration of the GRENOUILLE is described in chapter 3.

3.3 Design of the GRENOUILLE

The GRENOUILLE [2] is one possible experimental apparatus to measure the field and phase of an ultrafast laser pulse. Its name is the French name for frog and stands for "**Gr**ating-**E**liminated **N**o-nonsense **O**bservation of **U**ltrafast **I**ncident **L**aser **L**ight **E**-fields".

The goal of this particular realization is to record the autocorrelation (compare equation 3.2.1) trace with a CCD[5] camera in one shot. Its setup can be divided into two functional groups, one which resolves the time and one which resolves the frequency. In the FROG approach, time is resolved by a variable path length and the frequency is measured with a spectrometer. The GRENOUILLE performs both tasks in a nonlinear crystal, the time resolution in the horizontal plane (top view) and the spectral analysis in the vertical plane (side view). A key feature is the thick second harmonic generation (SHG) crystal (3).

Figure 3.4 shows a sketch of both views allowing to demonstrate the purpose of every single element. Before the beam enters the apparatus the beam is enlarged to a diameter of about one centimeter.

Following the top view path illustrates the time resolution mechanism. The broadened beam passes through the cylindrical lens (1) without change. This lens becomes important in the frequency resolution path. Subsequent the beam enters the Fresnel biprism (2) with an apex angle of 170°. It is creating two crossing beams coming to complete overlap in the thick SHG crystal (3) in the horizontal plane. The beams could be regarded as plane waves at this point so that they meet each other at a fixed angle in the crystal. This leads to a situation in which the path length difference of two crossing parts of the beams

[1] Frequency Resolved Optical Gating

[2] GRating-Eliminated No-nonsense Observation of Ultrafast Incident Laser Light E-fields

[3] Spectral Phase Interferometry for Direct Electric field Reconstruction

[4] Multiphoton Intrapulse Interference Phase Scan

[5] charge-coupled device, electronic light sensor

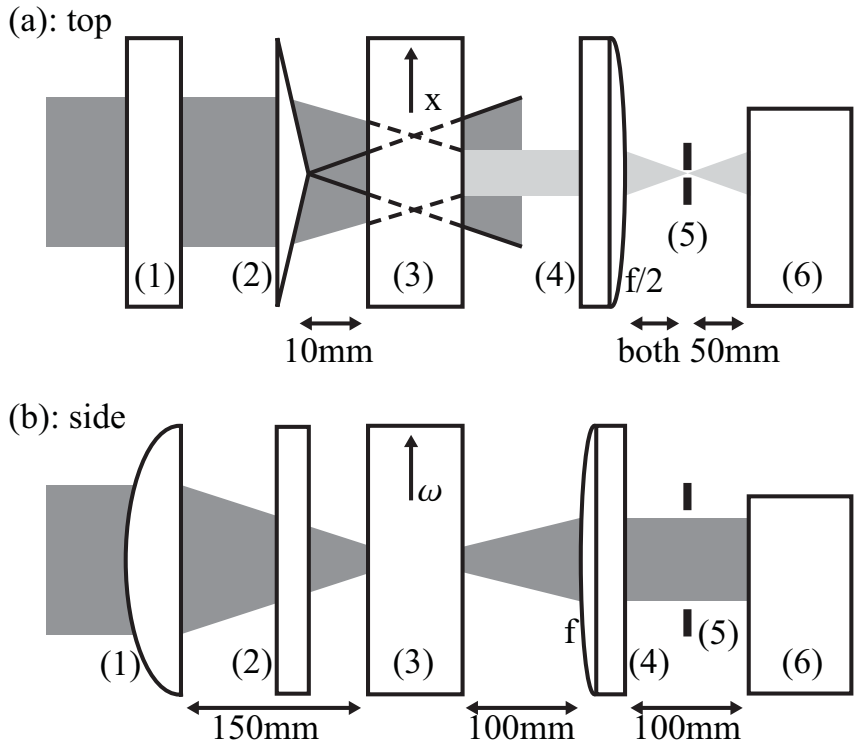

Figure 3.4: Side and Top View of a GRENOUILLE Setup. The figure part (a) with the top view shows the time resolution beam path, the figure part (b) the frequency resolution beam path. The elements are the following: (1) cylindrical lens, (2) Fresnel biprism, (3) thick SHG crystal, (4) imaging lens with focii $f/2$ for top view and f for side view, (5) slit and (6) CCD camera

only depends on their horizontal position in the crystal. Along the middle of the crystal the difference is zero and scales linear towards the edges.

Therefore the width of the beam in the crystal (about 4 mm) in conjunction with the biprism apex angle determines the possible path differences between the two beams. Knowing the speed of light in the crystal (index of refraction given in figure 3.5) one can derive the maximum time delay between the beams.

The thick crystal is made from a material with a high nonlinear response. Potassium Dihydrogen Phosphate (KDP) with a length of 10 mm is used in our setup. Three different beams of second harmonic light will come out of the crystal. Two are parallel to the incoming beams. They are created by frequency doubling in the single beams. They do not comprise any information about the autocorrelation, hence these beams are filtered by the slit (5).

The third signal is the cooperative one being created by one photon of each beam. Due to conservation of momentum this beam comes out parallel to the beam before the biprism. It is the autocorrelation between the pulses. Depending on where in the crystal the process takes place, the incoming pulses are shifted in time. Hence the outcoming light provides the time resolution mapped to space in the horizontal plane. The signal can be imaged with an additional lens (4) (focal length of 50 mm in this plane) to a CCD chip (6). Images can be taken with a resolution of 1280×1024 pixel.

The spectral resolution (side view) works differently. To create SH light in a non-linear crystal, both the incoming and the SH beam must be phase matched as the group velocities of the two beams in the crystal usually differ due to dispersion. This is especially the case if the crystal is thick.

Birefringence nevertheless allows to phase match the beams by choosing different projections of ordinary and extraordinary polarization for the beams. The condition on the refractive indices n_1 and n_2 for matching the group velocities of the frequencies ω and 2ω is

$$c/n_1(\omega) = c/n_2(2\omega) \tag{3.3.1}$$

This can be satisfied by tilting the crystal by some angle, namely the phase-matching angle α. The beams then see a combination of n_o and n_{eo}. The formula to calculate the right angle for a frequency ω is

$$\sin\left(\alpha(\omega, 2\omega)\right)^2 = \frac{n_o(\omega)^{-2} - n_o(2\omega)^{-2}}{n_{eo}(2\omega)^{-2} - n_o(2\omega)^{-2}} \tag{3.3.2}$$

for a negative birefringent crystal. The tolerance within the angle for a certain wavelength mainly depends on the thickness of the crystal. Longer paths in the crystal imply more destructive interference for imperfectly matched SH light and therefore a smaller tolerance.

The issue of phase matching is the key to the spectral resolution. Every single wavelength has a certain phase matching angle. A single wavelength going into the crystal at its phase matching angle produces constructively interfering SH photons whereas every different wavelengths has destructive interference at this angle.

Therefore a thick crystal produces spectrally resolved SH light by mapping wavelength to different angles. The setup is designed such that the beams come in focused by an angle large enough to cover all phase matching angles. For wavelengths between 720 nm and 850 nm the beam focusing angle has to be greater than 5.6° and the crystal axis tilted by 46.1°. A cylindrical lens (1)

in front of the biprism which only influences the vertical plane will guarantee this focus. Afterwards the SH signal is imaged onto the CCD chip with the lens (4). The imaging lens has a different focal length of 100 mm for the vertical plane.

The thickness of the crystal is to be chosen with care. If the crystal is too thin, it will have a low frequency resolution. If the crystal is too thick, it will disperse the incoming pulses during its passage so that the pulse length increases. To calculate an appropriate thickness the two following relations should be fulfilled. The group velocity mismatch ($GVM = \frac{1}{v_g(2\omega)} - \frac{1}{v_g(\omega)}$) between SH and fundamental beam multiplied by the length of the crystal L must be greater than the temporal pulse width τ to maintain good frequency resolution.

On the other hand the group velocity dispersion ($GVD = \frac{\partial}{\partial\omega}\frac{1}{v_g(\omega)}$) multiplied by the frequency bandwidth of the pulse $\Delta\omega$ and the length of the crystal L should be smaller than the the temporal pulse width τ

$$GVM \cdot L > \tau > GVD \cdot \Delta\omega \cdot L \tag{3.3.3}$$

Detailed exemplary calculations have been carried out by Trebino *et al.* [32] for Beta Barium Borate (BBO)-crystals. For an ultrafast system with pulses centered at 780 nm a 1 mm thick crystal can handle pulse durations between 30 fs and 80 fs. Longer pulses need thicker crystals.

3.4 Calibration of the GRENOUILLE

The components of our setup have been chosen by a former student of the group. The KDP crystal has a thickness of 10 mm which is much too long. KDP has a slightly lower index of refraction for ordinary and and extraordinary polarization than BBO, its GVD is almost the same as in BBO (compare figure 3.5).

The optimal thickness for the KDP crystal would be between 1 mm and 2 mm. With the given crystal the dispersion is so high that pulses are prolonged in time significantly.

To calibrate the axes of the data traces a set of different pulses is measured with the FROG and with the GRENOUILLE. The FROG gives reliable information about time and frequency. Comparing the GRENOUILLE traces with the FROG values allows us to determine the scales of the axes.

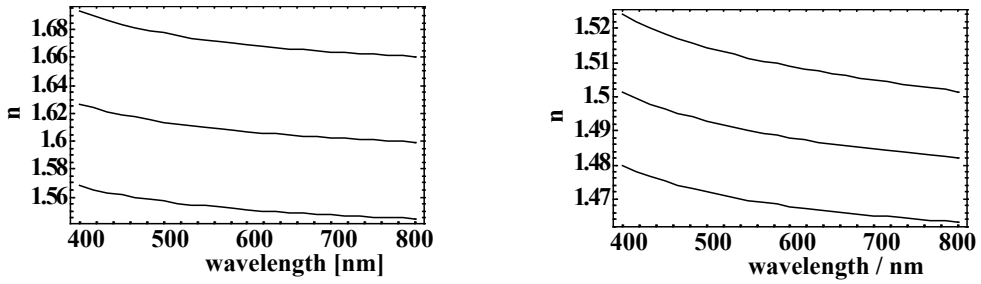

(a) (b)

Figure 3.5: Indices of Refraction for BBO and KDP. The graphs show the dispersion curves of BBO (a) and KDP (b) for ordinary (highest line), extraordinary (lowest line) and 45° (middle line) polarization. The values have been calculated with the Sellmeier equations.

A GRENOUILLE trace of a transform limited pulse looks like a two dimensional Gaussian distribution. Its relation between horizontal and vertical expansion depends on the setup. In our setup the traces have a cigar shape. Typical autocorrelation shapes can be found in [47]. For pulses with a spatial chirp the trace is tilted [1]. The angle indicates for a specific apparatus the amount of spatial chirp.

Figure 3.6 shows the GRENOUILLE trace of a 36 fs pulse taken by a CCD camera. Pixels in the horizontal dimension represent the time scale and pixels the vertical dimension the frequency scale. The shape is the predicted cigar shape with some small distortions. Dust on the CCD chip produces dark spots. Some other spots show an Airy pattern. They might come from diffraction by small distortions or dust on the optics. The inserted line in the lower part illustrates the shape of the projection onto the time axis.

For the calibration it is important to recall the reasons for different pulse duration with equal frequency bandwidth. Most pulses in experiments do not have the minimal temporal width they could have comparing with the transform limited pulse duration. The reason is that every pulse picks up a positive second order phase (compare chapter 3.1 about chirped pulses) by traveling through optics. Pulse durations prolong with the absolute amount of the phase (hence are independent from its sign).

For the calibration of the GRENOUILLE a set of pulses with different pulse duration is created by actively introducing such a second order phase. The FROG, which has very small internal dispersion (there are no lenses and just a

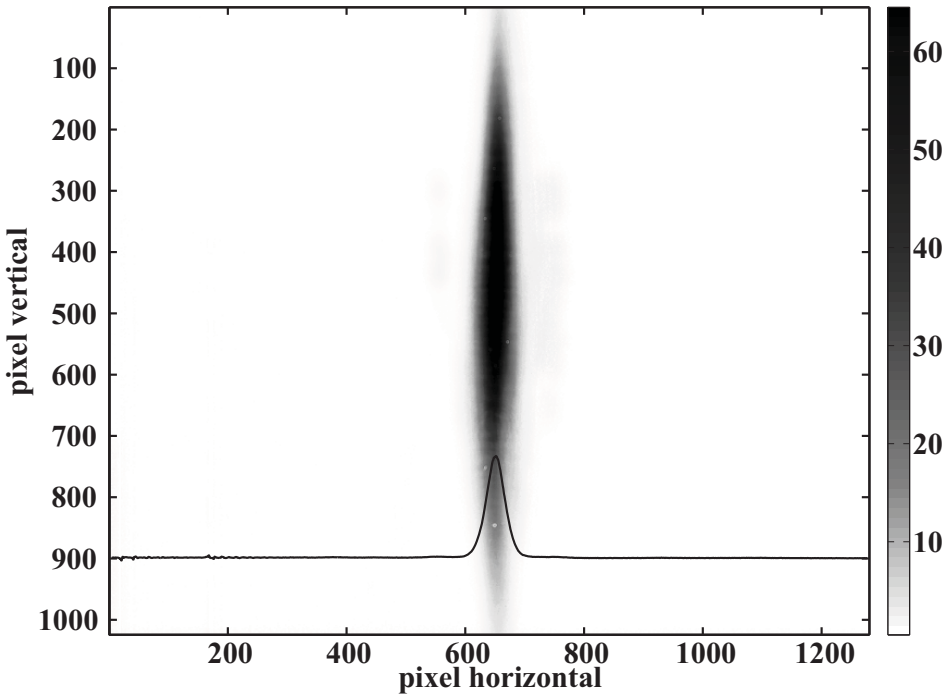

Figure 3.6: GRENOUILLE Trace of Short Pulse. The trace of a 36 fs pulse taken with a CCD camera looks like a cigar and is almost symmetric. The horizontal dimension represents the time scale, the vertical dimension the frequency scale. Dust on the optics produces the dark spots. The inserted line illustrates the shape of the projection onto the time axis.

very thin crystal) does not change the phase during measurement. In contrast to this, the GRENOUILLE introduces a fixed amount of positive chirp. For a transform limited pulse this leads to a longer duration but for pulses with negative phase distortion the GRENOUILLE compensates to some amount and can even shorten the pulse.

As result the relation between the pulse duration in the FROG and the pulse duration in the GRENOUILLE is not linear. There even occurs an ambiguity in the calibration. With a thinner crystal this problem would be much smaller but the current setup has to take it into account.

There is no way to use the CCD camera data for reconstruction. The algorithm can not compensate for the ambiguity. Nevertheless the width of the autocorrelation is a reliable measure of the pulse duration for simple pulses.

It is important to find a robust way to measure the width of the pixel

distribution. We chose to take the average FWHM of all horizontal lines. This value represents the mean of all frequencies. Thus the algorithm is not influenced much by distortions as seen in the image above. The inserted line in figure 3.6 allows us to determine the FWHM.

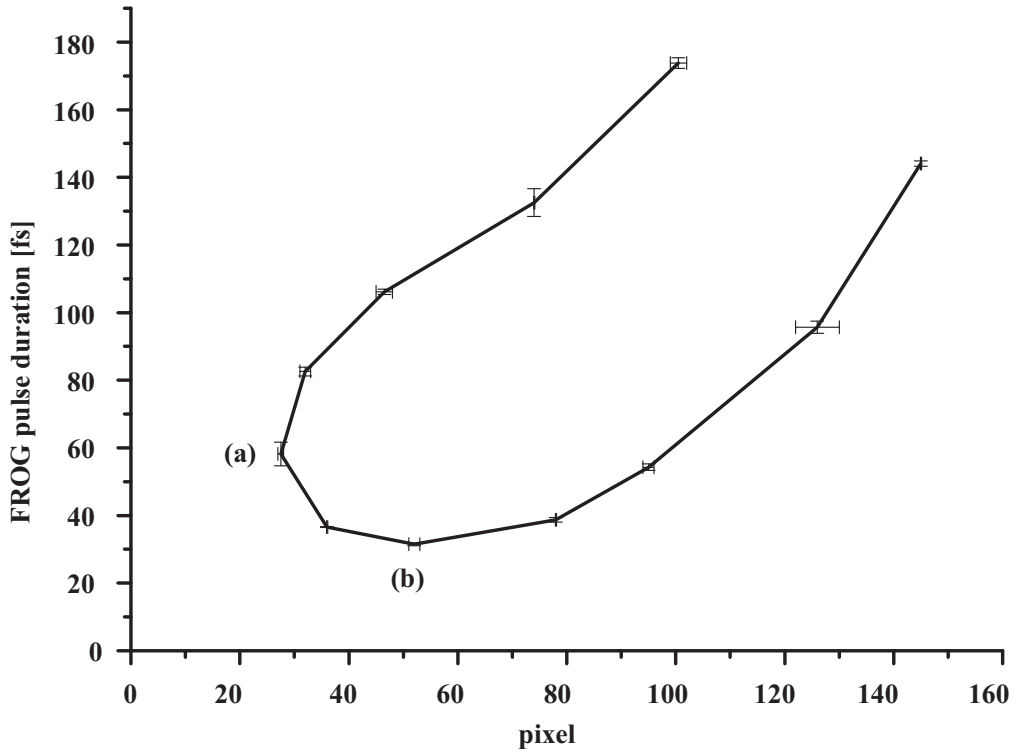

Figure 3.7: GRENOUILLE Pulse Duration Calibration. The calibration trace shows the FROG pulse durations measured in dependence of the pixel width of the distribution from the CCD camera. Due to the dispersion in the thick KDP crystal the curve is not linear and shows an ambiguity. Phases for data points (a) and (b) are shown in figure 3.9.

Figure 3.7 shows the calibration data. The run of the curve shows clearly that minimal pulse duration in the FROG and narrowest pixel distribution do not coincide.

The shortest pulse (30 fs) has a width of 54 px whereas the smallest pixel width (28 px) has a pulse duration of 58 fs. A pulse of 58 fs has exactly the amount of negative chirp which the crystal and the lenses introduces positively. Hence the pixel width becomes minimal. Every measured value broader than 28 pixels corresponds to two possible pulses: one is longer than 58 fs, has negative chirp and is compressed (upper branch) and the other one is shorter

than 58 fs, has positive chirp and is stretched (lower branch).

Figure 3.8 shows a reconstructed pulse with its intensity and phase. One can see that the pulse has a flat temporal phase. This pulse corresponds to the FROG minimum with 28 fs.

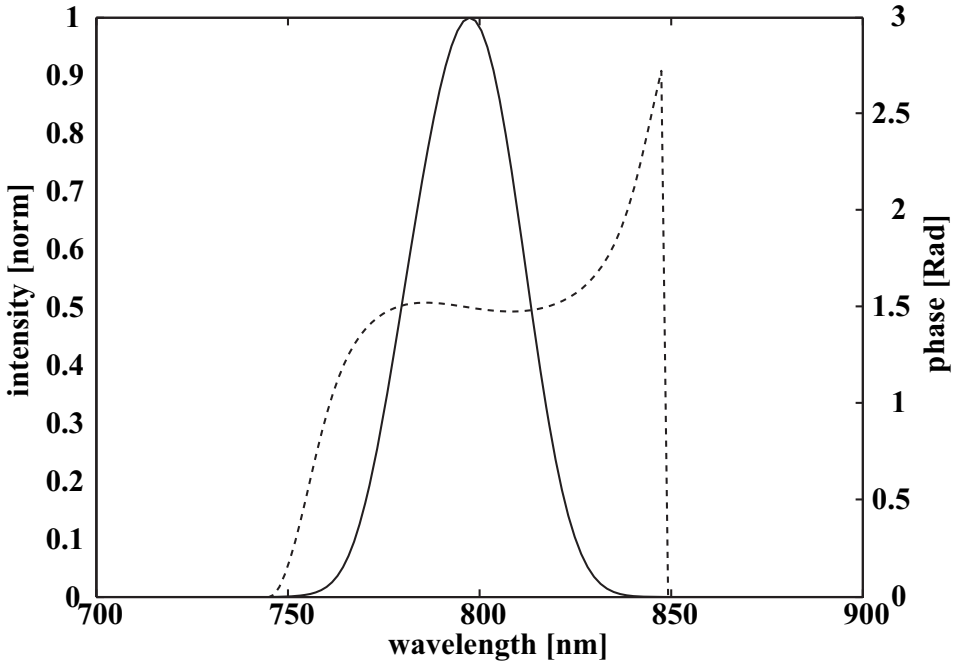

Figure 3.8: Pulse with Flat Phase. This pulse is the shortest FROG measure and has a flat phase throughout its intense parts. The solid line shows the intensity in time, the dashed line indicates the phase. It is flat in the main region of the pulse. The wings of the pulse have a small influence on the pulse.

The second pulse shown in figure 3.9 has a negative chirp though it is shown positively. SHG reconstruction does not allow us to determine the sign of the phase so that the algorithm picks it randomly. This pulse corresponds to the GRENOUILLE minimum. It has exactly the right amount of negative chirp to be compensated in the crystal. The result is a narrowest in pixels.

To use the GRENOUILLE as a fast measure for the pulse duration, the lower branch of the calibration data is fitted. Assuming that the pulse is already close to its optimal duration (which means it is on this branch) the fitted function allows us to determine the pulse duration in real time. Another student (Brendan Keller) of the group has written the LabVIEW code for the

CCD camera.

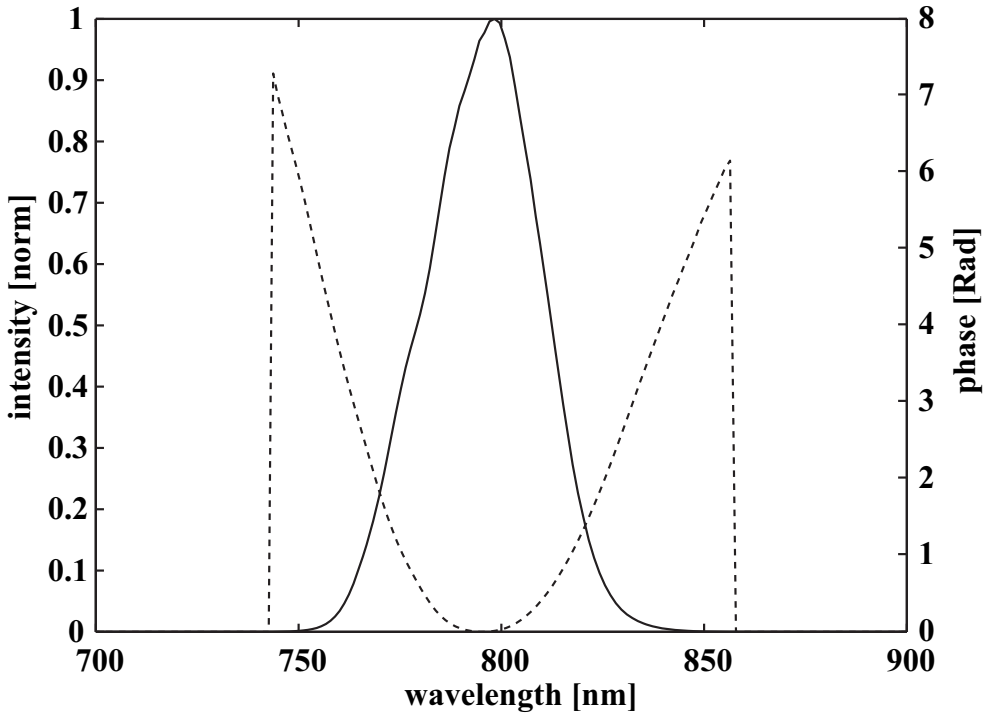

Figure 3.9: Pulse with Quadratic Phase. This pulse has the narrowest pixel width in the GRENOUILLE and a negative phase which is compensated by the crystal. The solid line shows the intensity and the dashed line the phase in time. (The phase is shown positively as the retrieval algorithm cannot determine its sign.)

The fitted function is

$$\tau(\Delta x) = (593.68 - 46.542\Delta x + 1.559(\Delta x)^2 - 0.02703(\Delta x)^3 + 0.00026(\Delta x)^4)\,\text{fs} \tag{3.4.1}$$

where τ is the pulse duration in fs and Δx the pixel width.

The error bars in figure 3.7 indicate the spread of three different traces taken for every data point. For short and simple pulses the results of the GRENOUILLE measurement are well reproducible. The mean error in the pulse duration is $\pm$ 1.5 fs. This error adds to the unknown error of the FROG. The guess for the overall error is $< \pm$ 3 fs. Determining the pulse duration is rather insensitive to the alignment. Misaligned beams are displaced on the

CCD camera but their width stays almost constant.

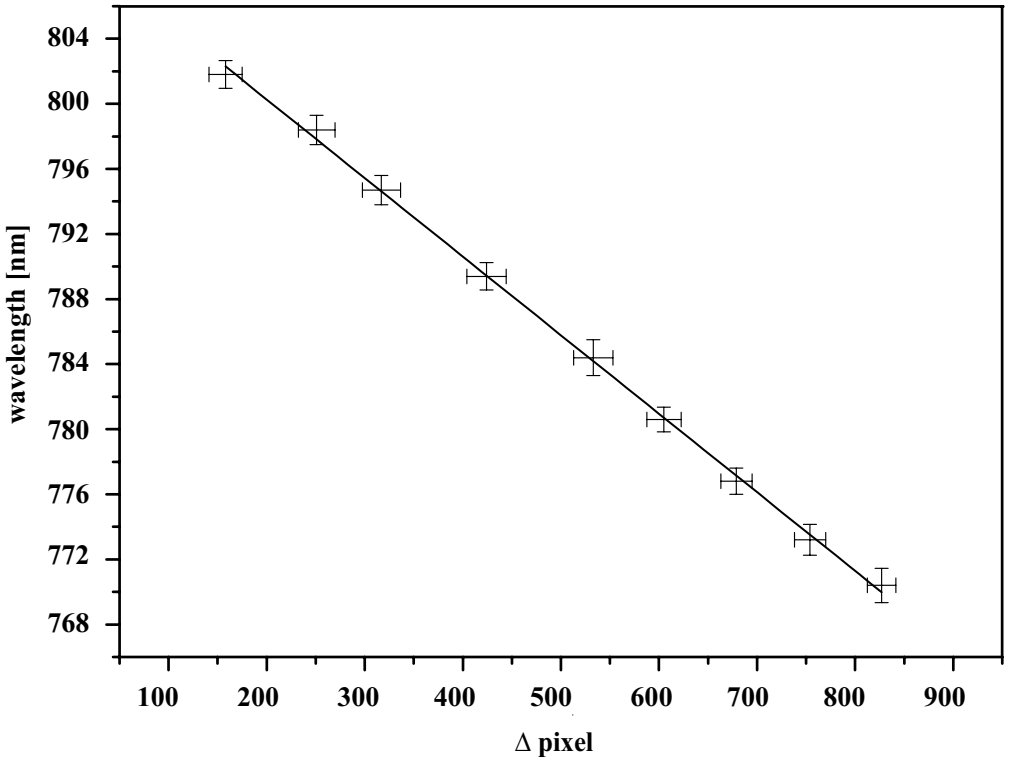

Figure 3.10: GRENOUILLE Wavelength Calibration. The curve shows the measured frequency dependence from the position on the CCD camera.

Shaped pulses with complicated phases cannot been measured with the GRENOUILLE. For this reason it is mainly used to check the amplifier output.

A wavelength calibration is carried out with the pulse shaper. Narrow bandwidth pulses are measured in the GRENOUILLE. Reference spectra have been measured with a spectrometer. The relation between the position on the CCD camera and the wavelength is to good approximation linear. Figure 3.10 shows the data. It was fitted to

$$\lambda(x) = (808.9 - 0.024x)\,\mathrm{nm} \tag{3.4.2}$$

with the wavelength λ in nm and the position x on the CCD camera in pixel. This calibration is less important as it does not give more information than a usual spectrometer. Furthermore it is highly dependent on correct alignment.

With the time calibration the GRENOUILLE is used on an every day basis

for monitoring the pulse duration.

Chapter 4

Theoretical Background

The understanding of ultrafast pulses and their interaction with matter requires a detailed description of the electric field and its interplay with atomic states. Many assumptions known from "traditional" optics do not hold true in the fs-regime. Therefore the following chapter will discuss the most important features of ultrafast pulses interacting with atoms. Furthermore the chemical element Rubidium is presented with its important properties.

4.1 Two-Level-Atoms

Real atoms usually have very complex internal structures with numerous energy levels. Nevertheless most experiments are designed to limit the amount of states which take part in the processes. In a lot of cases the number of relevant levels can be reduced to two or else two levels mainly determine the dynamics of the atomic system. So the behavior of two-level-atoms has been studied comprehensively.

The following chapter explains one approach to two-level-atoms. It is important to notice that the process of spontaneous emission is not taken into account in this picture. Introducing the concept of Rabi cycling leads to a description of these systems in terms of intensity and detuning. The treatment of two-level-atoms follows Tannor [43]. A similar derivation can be found in Boyd [8].

The Hamiltonian for these two-level-atoms has the two eigenstates Ψ_a and Ψ_b with the energies $E_a = \hbar\omega_a$ and $E_b = \hbar\omega_b$ respectively. The transition frequency is $\omega_0 = \omega_b - \omega_a$.

The general wave function for the two-level-atoms thus reads:

$$\Psi(t) = a(t)e^{-i\omega_a t}\Psi_a + b(t)e^{-i\omega_b t}\Psi_b \tag{4.1.1}$$

The square of the coefficients $|a(t)|^2$ and $|b(t)|^2$ represent the probabilities of finding an electron in state Ψ_a or Ψ_b respectively. A light field interacts with the states via the dipole moment μ and produces the coupling term $V = -\mu_{ab}\varepsilon(t)$. Writing the time-dependent Schrödinger equation in matrix form leads to

$$i\hbar\frac{d}{dt}\begin{pmatrix} a(t)e^{-i\omega_a t} \\ b(t)e^{-i\omega_b t}\end{pmatrix} = \begin{pmatrix} E_a & -\mu_{ab}\varepsilon(t) \\ -\mu_{ba}\varepsilon(t) & E_b\end{pmatrix}\begin{pmatrix} a(t)e^{-i\omega_a t} \\ b(t)e^{-i\omega_b t}\end{pmatrix} \tag{4.1.2}$$

The electric field is considered to be CW field with a single frequency so that it can be written as $\varepsilon(t) = 1/2\ \varepsilon\cdot(e^{i\omega t} + e^{-i\omega t})$ and the two dipole moments are equal $\mu_{ab} = \mu_{ba} = \mu$. This results in a system of coupled differential equations

$$\dot{a}(t) = i\frac{\mu\varepsilon}{2\hbar}\left(e^{+i(\omega-\omega_0)t} + e^{-i(\omega+\omega_0)t}\right)b(t) \tag{4.1.3a}$$

$$\dot{b}(t) = i\frac{\mu\varepsilon}{2\hbar}\left(e^{-i(\omega-\omega_0)t} + e^{+i(\omega+\omega_0)t}\right)a(t) \tag{4.1.3b}$$

The detuning is defined as $\Delta = \omega - \omega_0$. For the next step the rotating wave approximation is applied. This means that all fast oscillating terms like $e^{+i(\omega+\omega_0)t}$ are considered to average to zero. In this case the RWA is a very good approximation as the detuning is orders of magnitudes smaller than the transition frequency. Hence we ignore the term.

$$\dot{a}(t) = i\frac{\mu\varepsilon}{2\hbar}e^{+i\Delta t}b(t) \tag{4.1.4a}$$

$$\dot{b}(t) = i\frac{\mu\varepsilon}{2\hbar}e^{-i\Delta t}a(t) \tag{4.1.4b}$$

A good trial for the solution for the state Ψ_a is made by

$$a(t) = C_a e^{-i\beta t} \tag{4.1.5}$$

which results in the equation for state Ψ_b

$$b(t) = -C_a\frac{2\hbar\beta}{\mu\varepsilon}e^{-i(\Delta+\beta)t} \tag{4.1.6}$$

Using the last two equations with 4.1.4b leads to the condition

$$\beta(\Delta+\beta) = \left(\frac{\mu\varepsilon}{2\hbar}\right)^2 \tag{4.1.7}$$

The Rabi frequency is introduced as $\Omega = \mu\varepsilon/\hbar$ so that the solution for β is given by

$$\beta_\pm = 1/2\left(\Delta \pm \sqrt{\Delta^2+\Omega^2}\right) = 1/2\left(\Delta \pm \tilde{\Omega}\right) \tag{4.1.8}$$

The generalized Rabi frequency $\tilde{\Omega} = \sqrt{\Delta^2+\Omega^2}$ plays the central role in this description of the two-level-atoms.

Substituting back β into equations 4.1.4 leads to the general solutions

$$a(t) = -\frac{1}{\Omega}e^{+\frac{i}{2}\Delta t}\left(A(\Delta-\tilde{\Omega})e^{+\frac{i}{2}\tilde{\Omega}t} + B(\Delta+\tilde{\Omega})e^{-\frac{i}{2}\tilde{\Omega}t}\right) \tag{4.1.9a}$$

$$b(t) = e^{-\frac{i}{2}\Delta t}\left(Ae^{+\frac{i}{2}\tilde{\Omega}t} + Be^{-\frac{i}{2}\tilde{\Omega}t}\right) \tag{4.1.9b}$$

Choosing the initial conditions to be $|a(t_0)|^2 = 1$ and $|b(t_0)|^2 = 0$ defines the constants $A = -B = \mu\varepsilon/(2\hbar\tilde{\Omega})$. To obtain the populations the solutions are squared and read

$$|a(t)|^2 = \left(\frac{\Delta}{\tilde{\Omega}}\right)^2 + \left(\frac{\Omega}{\tilde{\Omega}}\right)^2 \cos^2(\tilde{\Omega}t/2) \tag{4.1.10}$$

$$|b(t)|^2 = \left(\frac{\Omega}{\tilde{\Omega}}\right)^2 \sin^2(\tilde{\Omega}t/2) \tag{4.1.11}$$

The population of excited state Ψ_b is plotted in figure 4.1. It rises from zero to a maximal amount and oscillates between these two values. The maximal population transfer is given by the ratio $\Omega/\tilde{\Omega}$, its frequency is given by $\tilde{\Omega}/(4\pi)$. The population transfer is unity for a light field without detuning and smaller for all fields with non-zero detuning.

Figure 4.1 illustrates this behavior for two different generalized Rabi frequencies. As the frequencies of the sinusoidal parts depend on $\tilde{\Omega}$ the two cases have different transfer rates.

It is important to keep in mind that this picture does not take into account the spontaneous emission which would decrease the population of state Ψ_b and hence lead to some kind of steady state behavior (treated for instance in Metcalf [28]).

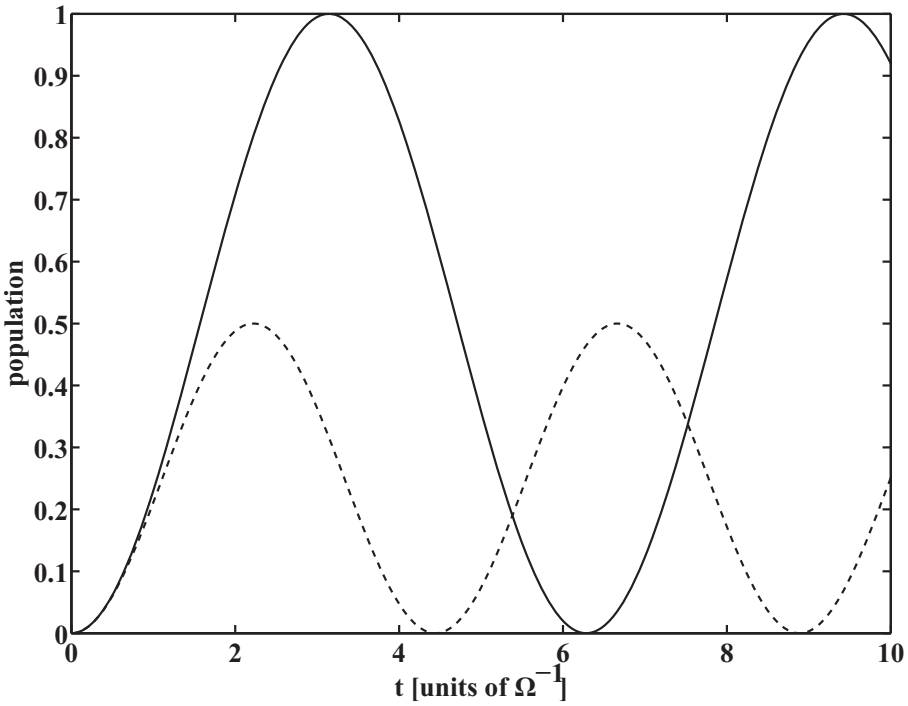

Figure 4.1: Rabi Oscillations. The oscillations for two detunings differ in frequency and amplitude. The full line shows the case of zero detuning, the dashed line has a detuning of $\Delta = \tilde{\Omega}$.

In the limit of short times and weak field the sine function can be approximated to be linear. It turns out that the population transfer is proportional to the intensity ($\propto \varepsilon^2$) and does not depend on the detuning.

$$|a(t)|^2 = \left(\frac{\Omega}{2}\right)^2 t^2 \tag{4.1.12}$$

Considering the case that the light field does not have a detuning but is changing in time the solutions (equations 4.1.14) depend on the "area" of the pulse. This solution is known as Area Theorem. The area of a pulse is defined by

$$A = \int_0^t \tilde{\Omega}(t')dt' \tag{4.1.13}$$

such that the populations read

$$a(t) = \cos\left(\frac{1}{2}\int_0^t \tilde{\Omega}(t')dt'\right) \tag{4.1.14a}$$

$$b(t) = i\sin\left(\frac{1}{2}\int_0^t \tilde{\Omega}(t')dt'\right) \tag{4.1.14b}$$

The importance of the area theorem is that the Rabi cycling in the case of varying fields does not depend on the particular field shape but just on its integral. It is easy to see from equations 4.1.14 that total inversion happens in the case when the ares is equal to π - a so called π-pulse.

4.2 Dressed States

In the dressed state picture, the influence of the presence of a light field is treated. As long as two-level-atoms are situated in the dark the previously described states Ψ_a and Ψ_b (see chapter 4.1) are the bare eigenstates of the system. The Hamiltonian is a diagonal matrix and its elements are the eigenenergies. This does not hold true any more when the coupling terms appear in the off-diagonal matrix elements of the Hamiltonian. New eigenstates which are superpositions of Ψ_a and Ψ_b occur with new eigenenergies.

This chapter introduces the most important changes when taking into account a combined system of atom and field. The calculations follow Tannor [43].

To address this problem we first calculate the expectation value of the dipole moment with the solutions of the two-level-atoms. This treatment shows that new transition frequencies occur at $\omega \pm \tilde{\Omega}$.

For determining the expectation value of the dipole moment we evaluate

$$\langle \mu(t) \rangle = \langle \Psi(t) \, |\mu| \, \Psi(t) \rangle \tag{4.2.1}$$

The dipole moment depends linearly on the integration coordinate r so that $\langle \Psi_a \, |\mu| \, \Psi_a \rangle = \langle \Psi_b \, |\mu| \, \Psi_b \rangle = 0$. Going back to the definition of the wave function Ψ in equation 4.1.1 the expectation value reads

$$\langle \mu(t) \rangle = a^*(t)b(t)\mu e^{-i\omega_{ba}t} + c.c. \tag{4.2.2}$$

with the coefficients $a(t)$ and $b(t)$.

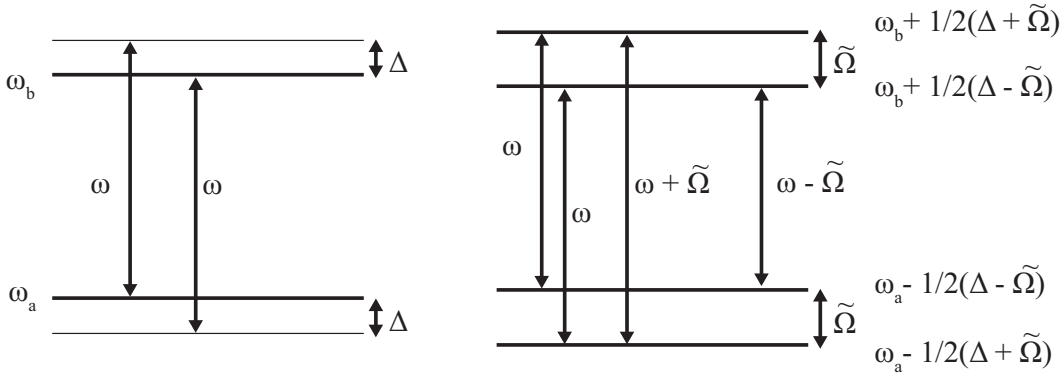

(a) Dressed State Weak Field (b) Dressed State Strong Field

Figure 4.2: Dressed State Spectrum. (a) In the weak field regime two new levels occur with an offset of Δ such that the light field is resonant with them. (b) In the strong field regime there are three different transition frequencies ω, $\omega \pm \tilde{\Omega}$ between the two dressed states. Both figures assume that the detuning is positive.

Plugging in solutions 4.1.9 from the two-level-derivation for $a(t)$ and $b(t)$, with the given integration parameters A and B, leads to the expression

$$\langle \mu(t) \rangle = -\frac{\Omega}{4\tilde{\Omega}^2} \left[2\Delta e^{-i\omega_{ba}t} - \left(\Delta - \tilde{\Omega}\right) e^{-i(\omega_{ba}+\tilde{\Omega})t} - \left(\Delta + \tilde{\Omega}\right) e^{-i(\omega_{ba}-\tilde{\Omega})t} \right] \mu_{ab} + c.c. \quad (4.2.3)$$

This solution shows that the dipole moment oscillates at the fundamental and two new frequencies $\omega \pm \tilde{\Omega}$. The reason for the behavior is that already the coefficients $a(t)$ and $b(t)$ oscillate at frequencies different from the light field. This is called Mollow triplet [30]. Figure 4.2(b) draws a sketch of the transitions.

In the case of zero detuning the dipole moment oscillates just at the two new different frequencies

$$\langle \mu(t) \rangle = -\frac{\Omega}{4\tilde{\Omega}} \left[e^{-i(\omega_{ba}+\Omega)t} - e^{-i(\omega_{ba}-\Omega)t} \right] \mu_{ab} + c.c. \quad (4.2.4)$$

There is no oscillation at the original frequency. The absorption line is split into two lines with a spacing proportional to the Rabi frequency.

As mentioned above, the dressed states can be regarded as superposition

of the atom's bare eigenstates. Going back to the solutions for $a(t)$ and $b(t)$ in equations 4.1.9 one can choose the integration parameters A and B to fit different initial conditions. One possible case is the combination $A = 0$ and $B = 1$ which is identified as Ψ_+. Likewise the combination $A = 1$ and $B = 0$ is also possible and is labeled Ψ_-.

Equation 4.1.9 read now

$$a_+(t) = -\frac{\Delta + \tilde{\Omega}}{\Omega} e^{-\frac{i}{2}(\tilde{\Omega}-\Delta)t} \tag{4.2.5a}$$

$$b_+(t) = e^{-\frac{i}{2}(\Delta+\tilde{\Omega})t} \tag{4.2.5b}$$

$$a_-(t) = -\frac{\Delta - \tilde{\Omega}}{\Omega} e^{\frac{i}{2}(\tilde{\Omega}+\Delta)t} \tag{4.2.5c}$$

$$b_-(t) = e^{-\frac{i}{2}(\Delta-\tilde{\Omega})t} \tag{4.2.5d}$$

We plug these coefficients into the definition of the wave function Ψ 4.1.1 and normalize the solutions. The resultant wave function composes of Ψ_a and Ψ_b.

$$\Psi_\pm = \mp\sqrt{\frac{\tilde{\Omega} \pm \Delta}{2\tilde{\Omega}}} \exp\left[+i\left(\frac{\Delta \mp \tilde{\Omega}}{2} - \omega_a\right)t\right]\Psi_a \pm\sqrt{\frac{\tilde{\Omega} \mp \Delta}{2\tilde{\Omega}}} \exp\left[-i\left(\frac{\Delta \pm \tilde{\Omega}}{2} + \omega_b\right)t\right]\Psi_b \tag{4.2.6}$$

These functions are the new eigenstates of the combined system of atom and field. The can be regarded as the eigenvector of the instantaneous Hamiltonian. Note that they do not give the eigenenergies as the Hamiltonian is explicitly time-dependent.

Projecting the functions $\Psi_\pm$ onto the bare eigenstates shows that the probability of finding the system in $\Psi_{a/b}$ is constant in time and hence that they are stationary states

$$|\langle\Psi_a|\Psi_\pm\rangle|^2 = \frac{\tilde{\Omega} \pm \Delta}{2\tilde{\Omega}} \tag{4.2.7a}$$

$$|\langle\Psi_b|\Psi_\pm\rangle|^2 = \frac{\tilde{\Omega} \mp \Delta}{2\tilde{\Omega}} \tag{4.2.7b}$$

For weak fields ($\Omega << \Delta$) one can approximate the generalized Rabi frequency to

$$\tilde{\Omega} \approx |\Delta| \left[1 + \left(\frac{\Omega}{\Delta} \right)^2 \right] \tag{4.2.8}$$

Assuming positive detuning the dressed states reduce to

$$\Psi_+ = -\sqrt{1 - \frac{\Omega^2}{2\Delta^2}} e^{-i\omega_a t} \Psi_a + \frac{\Omega}{\sqrt{2}\Delta} e^{-i(\omega_b + \Delta)t} \Psi_b \tag{4.2.9a}$$

$$\Psi_- = \frac{\Omega}{\sqrt{2}\Delta} e^{-i(\omega_a - \Delta)t} \Psi_a + \sqrt{1 - \frac{\Omega^2}{2\Delta^2}} e^{-i\omega_b t} \Psi_b \tag{4.2.9b}$$

Solution Ψ_+ is dominated by the bare eigenstate Ψ_a and Ψ_- by Ψ_b respectively. Both have small corrections of the other bare eigenstate with a new frequency associated which can be regarded as newly introduced level (compare figure 4.2(a)).

For some quantum mechanical problems it can be convenient to work in the interaction picture. This picture is intermediate between the Heisenberg and Schrödinger picture and evolves from them by an unitary transformation U. In the interaction picture the Hamiltonian is split into two parts $H = H_0 + V$ where H_0 denotes a well known Hamiltonian which is exactly solvable. The part V usually contains new terms which make the Hamiltonian more complex. Any arbitrary choice of the two parts is valid. When chosen properly the time evolution in the new picture can be much slower than in the other ones.

The new wave function reads

$$\Psi_i(t) = e^{i/\hbar H_0 t} \Psi_s(t) = e^{i/\hbar H_0 t} e^{-i/\hbar H_t} \Psi_s(0) \tag{4.2.10}$$

where Ψ_s represents the wave function in the Schrödinger picture.

The Hamiltonian in the Schrödinger picture is

$$H_s = \begin{pmatrix} E_a & -\frac{\mu\varepsilon(t)}{2} e^{-i\omega t} \\ -\frac{\mu\varepsilon(t)}{2} e^{-i\omega t} & E_b \end{pmatrix} \tag{4.2.11}$$

In our case it is advantageous to split the Hamiltonian into time-independent atomic and time-dependent field parts. We define the rotation of the frame (to go from Schrödinger to interaction picture) by the matrix

$$U = \begin{pmatrix} e^{-i(\omega_a - \Delta/2)t} & 0 \\ 0 & e^{-i(\omega_b + \Delta/2)t} \end{pmatrix} \tag{4.2.12}$$

Now the interaction Hamiltonian for a time dependent system reads (with applying the rotating wave approximation)

$$\begin{aligned} H_i &= U^{-1}(t) H_s(t) U(t) - i\hbar U(t)\dot{U}^{-1}(t) \\ &= \begin{pmatrix} E_a & -\mu\varepsilon(t)/2 \\ -\mu\varepsilon(t)/2 & E_b \end{pmatrix} + \begin{pmatrix} -\hbar\omega_a + \hbar\Delta/2 & 0 \\ 0 & -\hbar\omega_b - \hbar\Delta/2 \end{pmatrix} \\ &= \frac{\hbar}{2}\begin{pmatrix} \Delta & -\Omega \\ -\Omega & -\Delta \end{pmatrix} \end{aligned} \tag{4.2.13}$$

The physical meaning of this interaction picture is that one of the atomic levels has been shifted by the energy $\pm\hbar\omega$ so that the energy difference between them changes from $\hbar\omega_{ab}$ to $\hbar\Delta = \hbar\omega_{ab} - \hbar\omega$. The zero point of the energy has been redefined in the middle of the two new energies such that they are at $\pm(1/2)\hbar\Delta$. In the coupling terms only the envelope of the field remains in form of the Rabi frequency Ω. This is the main reason for going into the new picture. All fast oscillating terms have been eliminated and the time evolution just cares about the field envelope. Hence the new interaction Hamiltonian is much more convenient for further calculations.

To obtain the eigenenergies of the system we diagonalize the matrix H_i. The corresponding rotation matrix R can be classified by a rotation angle $\alpha = 1/2 \arctan \Omega/\Delta$

$$R = \begin{pmatrix} \cos(\alpha) & -\sin(\alpha) \\ -\sin(\alpha) & -\cos(\alpha) \end{pmatrix} \tag{4.2.14}$$

Like in equation 4.2.13 the transformation with matrix R reads

$$\begin{aligned} \tilde{H}_i &= R^{-1}(t) H_i(t) R(t) - i\hbar R(t)\dot{R}^{-1}(t) \\ &= \begin{pmatrix} E_+ & 0 \\ 0 & E_- \end{pmatrix} - i\hbar R(t)\dot{R}^{-1}(t) \end{aligned} \tag{4.2.15}$$

If the term $-i\hbar R(t)\dot{R}^{-1}(t)$ is small the system can be regarded to behave adiabatically, otherwise it behaves diabatically. The solution for the adiabtaic

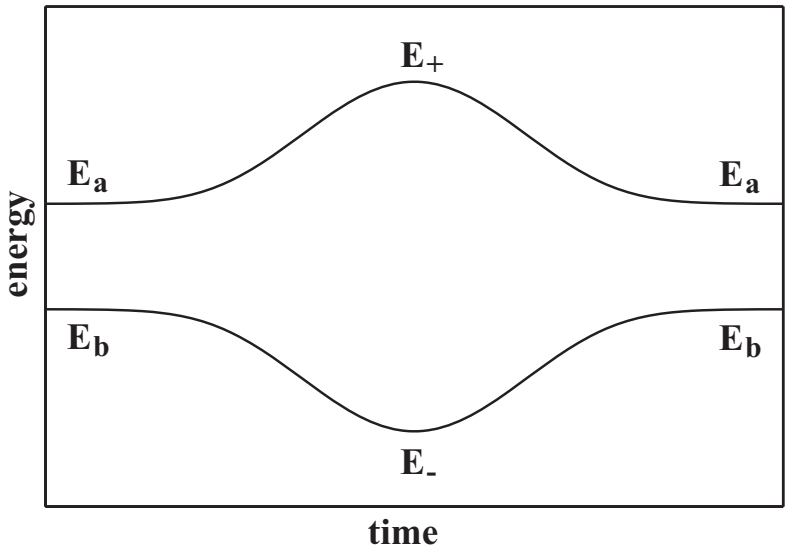

Figure 4.3: Eigenenergies of Dressed States. The adiabatic eigenenergies of dressed states for a detuned light pulse start in the bare eigenstates with energies $E_{a/b}$, evolves in the dressed states with energies $E_{\pm}$ and returns to the bare eigenstates.

eigenenergies $E_{\pm}$ reads

$$E_{\pm} = \pm\frac{\hbar}{2}\sqrt{\Delta^2 + \Omega^2} = \pm\frac{\hbar}{2}\tilde{\Omega} \tag{4.2.16}$$

Figure 4.3 shows the time evolution of the the energies $E_{\pm}$ for a detuned light pulse. In case the detuning Δ is much larger than the Rabi frequency Ω the eigenenergies can be developed as

$$E_{\pm} \approx \pm\frac{\hbar}{2}\left(\Delta + \frac{\Omega^2}{2\Delta} + ...\right) \tag{4.2.17}$$

The second term of the development (without the prefactor $\hbar$) is the frequency AC Stark shift

$$S_{AC} = \frac{\Omega^2}{4\Delta} \tag{4.2.18}$$

Chapter 5

Electromagnetically Induced Transparency in Rubidium

Electromagnetically induced transparency (EIT) is a mechanism to render an optically dense system transparent. It has been observed in many different experiments and can be used for a broad variety of applications. Stephen Harris *et al.* were the first to both describe theory [20] and carry out experiments [7, 19]. EIT has mainly been observed in atomic systems and but there are experiments in solids as well by Ham *et al.* [18].

Most experiments up to now have been carried out in the perturbative field strength regime and many aspects of the phenomena are well understood. In this domain the dynamics of the system are described with a perturbation theory solution of the three-level-atom.

However the exploration of EIT with strong and ultrafast fields has just started. Our experiments introduce a time domain perspective to EIT. The new aspects in this picture are based on two circumstances: On the one hand dephasing mechanisms are much slower than the excitation such that coherence between states can be maintained during the whole interaction. On the other hand field envelopes vary very rapidly in time and for this reason influence the dynamics.

5.1 Properties of Rubidium

Rubidium (Rb) is a silvery-white looking alkali metal. It is very soft and like most of the alkali metal highly reactive with oxygen and water. Two natural isotopes occur with 85 (72.17%) and 87 (27.83%) nucleons.

Rb-87 is slightly radioactive with a nuclear life time of $4.88 \cdot 10^{10}$ years. The melting point at atmospheric pressure is 39.31° C, the boiling point is at 668° C. Its atomic mass is 86.91u = $1.443 \cdot 10^{-25}$ kg. Ionization is observed for energies larger than 4.177 eV $\widehat{=}$ 33690 cm^{-1}.

Rubidium has 37 electrons which all except one are located in fully occupied orbitals. Almost all physical and chemical processes comprise just this single valence electron leading to an easy hydrogen like description. The ground state is $5^2S_{1/2}$ with the configuration $4p^6 5s$. The following energy diagram 5.1 (taken from NIST Atomic Spectra Database [34]) shows the atomic levels.

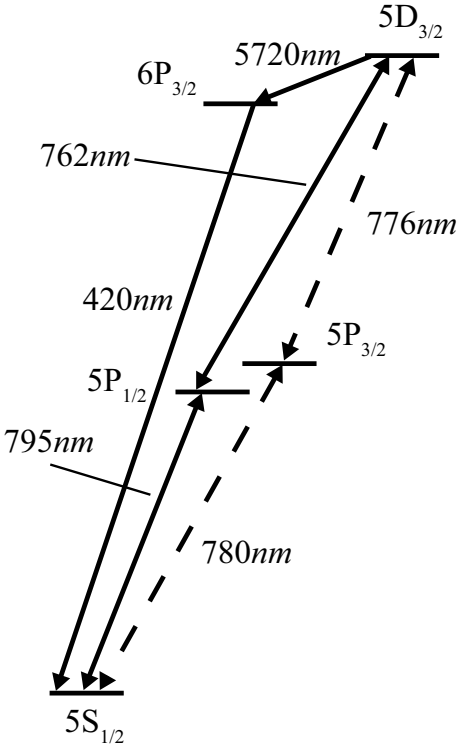

Figure 5.1: Rubidium Energy Diagram. The dashed lines show most important transitions. All lines connecting to $5P$ states lie within the bandwidth of the laser.

Four transitions lie within the bandwidth of the laser. Two of them lead from the ground state $5S$ to the intermediate levels $5P_{1/2}$ and $5P_{3/2}$. The other two transitions lead from the intermediate levels to the upper level $5D_{3/2}$. In the following experiments the transitions $5S_{1/2} \rightarrow 5P_{3/2}$ and $5P_{3/2} \rightarrow 5D_{3/2}$ are used for the EIT, all four transitions are used for the superfluorescence.

All wavelengths and dipole moments are listed in table 5.1. The dipole moment for the $5P_{1/2} \rightarrow 5D_{3/2}$ is unknown but Warren *et al.* [44] indicate that it is small in comparison to the other three of the discussed transitions.

Table 5.1: Transition Data of Rb

transition	λ / nm	dipole moment/ 10^{-29} Cm	source
$5S_{1/2} \rightarrow 5P_{1/2}$	794.7	1.967	[34]
$5S_{1/2} \rightarrow 5P_{3/2}$	780.0	4.97	[10]
$5P_{1/2} \rightarrow 5D_{3/2}$	794.7	—	[34]
$5P_{3/2} \rightarrow 5D_{3/2}$	775.9	1.50	[10]
$5D_{3/2} \rightarrow 6P_{3/2}$	5720	—	[34]
$6P_{3/2} \rightarrow 5S_{1/2}$	420.2	—	[34]

The state $6P_{3/2}$ becomes important for the measurements in the section 6.2 on superfluorescence.

Rubidium has a hyperfine structure as the nuclei have spin 5/2 (Rb-85) and 3/2 (Rb-87). The resultant energy shifts are on the order of 100 MHz. These shifts correspond to a wavelength difference of 20 pm being orders of magnitudes smaller than resolvable with the available spectrometers. Therefore all experimental data will not be able to resolve the structure.

In quantum mechanics the time evolution of a state is always relative to another state. It is proportional to the energy difference between the two states. In the case of the Rubidium the time scale for phase evolution between hyperfine levels is of the order of 100 ms which is very long in comparison to the time scales of the experiments. Hence the evolution can be neglected.

The Einstein A_{ki} coefficients for the $5S_{1/2} \rightarrow 5P_{3/2}$ and $5P_{3/2} \rightarrow 5D_{3/2}$ transitions are $3.81 \cdot 10^7\,\mathrm{s}^{-1}$ and $3.61 \cdot 10^7\,\mathrm{s}^{-1}$ respectively (taken from NIST database [34]). Calculating the lifetimes of the excited states results in about 25 ns. This means that they all are at least four orders of magnitude longer than the time scale of the experiments. For this reason spontaneous emission can be neglected during the experiment. Hence the two-level-atom approximation (see chapter 4.1) which neglects spontaneous emission applies well to the case of rubidium as long as just a single transition is excited.

The vapor pressure P_V in Torr for the liquid phase is given by

$$\log_{10} P_V = 15.882 - \frac{4529.6}{T} + 0.000586T - 2.991 \log_{10} T \tag{5.1.1}$$

with the temperature T in K. At low pressures it is satisfactory to assume an ideal gas which leads to the density-temperature diagram 5.2.

All numbers - if not indicated differently - are taken from Steck [41].

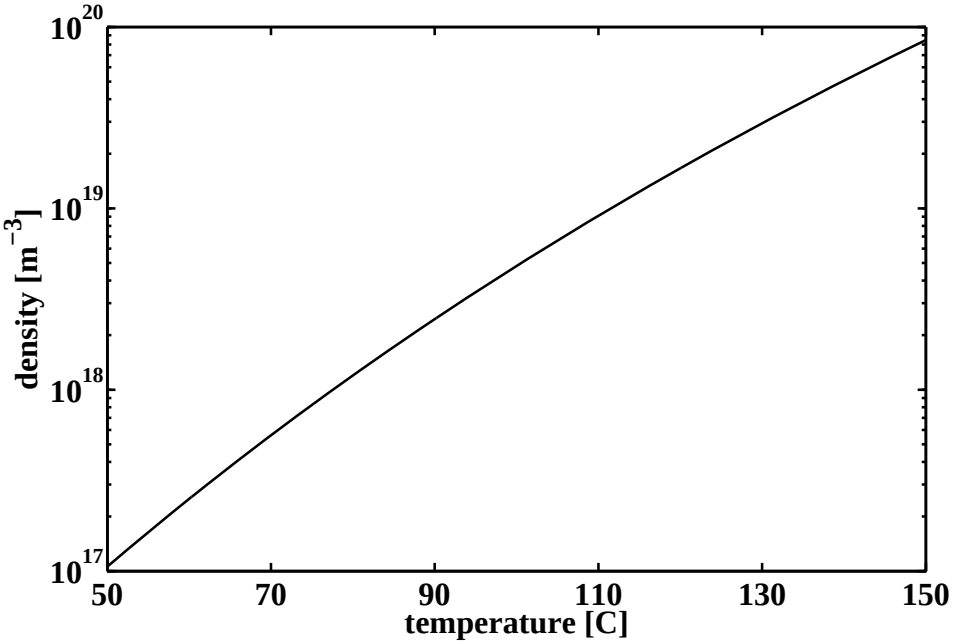

Figure 5.2: Rubidium Density Diagram. The curve shows the dependence of the rubidium density on temperature.

5.2 Electromagnetically Induced Transparency

The technique of EIT for eliminating resonant transitions has been used in many experiments. Maybe best known is the application of "slow light" [21] where EIT is used to generate a system with a very small group velocity. Nonlinear processes can profit strongly from EIT as demonstrated with second harmonic generation in hydrogen [17]. Furthermore EIT relates to topics like lasing without inversion [37].

EIT in atomic experiments can only be observed in three- (or multi) level systems. These either ladder- or lambda-type energy levels have three states which we denote $|a\rangle$, $|b\rangle$, $|c\rangle$ (compare figure 5.3). In the case of a ladder system one also finds "ground state", "intermediate state" and "excited state" in some literature. The nomenclature is chosen such that the state $|c\rangle$ always connects to both $|a\rangle$ and $|b\rangle$. The coupling transition with frequency ω_c links the states $|b\rangle$ and $|c\rangle$ and the probe transition with frequency ω_p states $|a\rangle$ and

$|c\rangle$ respectively.

There is no allowed dipole transition between $|a\rangle$ and $|b\rangle$.

Understanding EIT requires a quantum mechanical point of view. The key to the description is interference between wave functions excited to $|c\rangle$ from two different states, namely $|a\rangle$ and $|b\rangle$. If both coupling and probe fields are close to resonance on their transitions they are introducing quantum coherence between the states $|a\rangle$ and $|b\rangle$. Interference reduces the effective transfer into state $|c\rangle$ dramatically. This phenomena is called coherent population trapping (CPT) [3].

The levels in figure 5.3 are dressed by the light field. When the light field appears as off-diagonal elements in the Hamiltonian, the bare states of the atoms evolve to dressed states $|p, m\rangle$ which are coherent superposition of the bare states $|a\rangle$ and $|b\rangle$. Considering the light fields to be probe (with Rabi frequency Ω_p) and coupling (with Rabi frequency Ω_c) fields the dressed states are

$$|p, m\rangle \propto \Omega_p |b\rangle \pm \Omega_c |a\rangle \qquad (5.2.1)$$

where Ω_c and Ω_p denote the coupling and probe Rabi frequencies.

We calculate the expectation value of the dipole operator $\hat{\mu}$ for the two levels $|c\rangle$ and $|m\rangle$

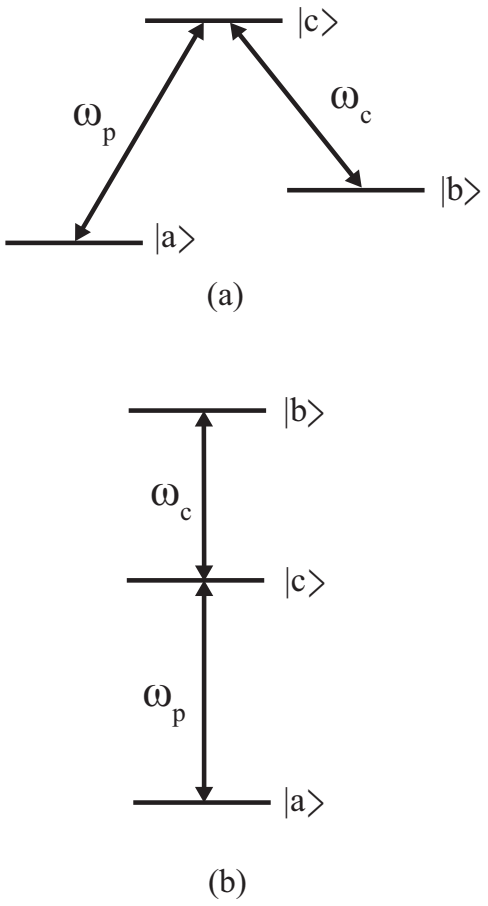

Figure 5.3: EIT Level Systems. (a) In a lambda system the levels are labeled $|a\rangle$, $|b\rangle$ and $|c\rangle$ with the coupling ω_c and probe ω_p transitions frequencies. (b) For ladder systems the $|c\rangle$ states corresponds to the intermediate state.

$$|\langle c| \hat{\mu} |m\rangle|^2 \propto |\langle c| \hat{\mu} (\Omega_p |b\rangle - \Omega_c |a\rangle)|^2 \propto |\Omega_c \Omega_p - \Omega_p \Omega_c|^2 = 0 \qquad (5.2.2)$$

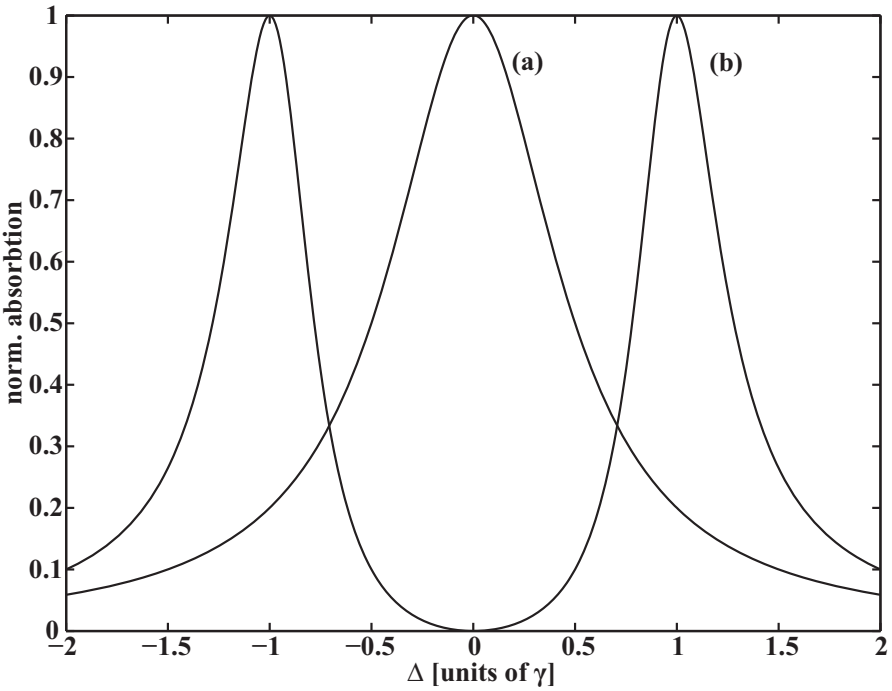

Figure 5.4: Imaginary part of the susceptibility. The absorption line for zero coupling (a) splits into two lines (b) for a coupling Rabi frequency of $\Omega_c = 2\gamma$.

The result from the vanishing expectation value of the dipole moment is that atoms put into state $|m\rangle$ cannot be excited any more to state $|c\rangle$. Consequently they do not contribute any more to absorption processes. Furthermore there is no dipole moment that connects the two superpositions $|p\rangle$ and $|m\rangle$. Hence population - once transfered to $|m\rangle$ - is trapped in this state. As the rate of population transfer into this state is nonzero for all times population accumulates in the trapped state and does not take part any more in the dynamics.

This behavior leads to EIT in the case that a coupling field ε_c introduces the coherences on the $|b\rangle \rightarrow |c\rangle$ transition. A probe field ε_p on the $|a\rangle \rightarrow |c\rangle$ transition has no population to interact with. Hence the usually optical dense transition is transparent.

The time scales on which the EIT forms depends on whether the initial state is empty or populated. For the case that states $|a\rangle$ and $|c\rangle$ are both

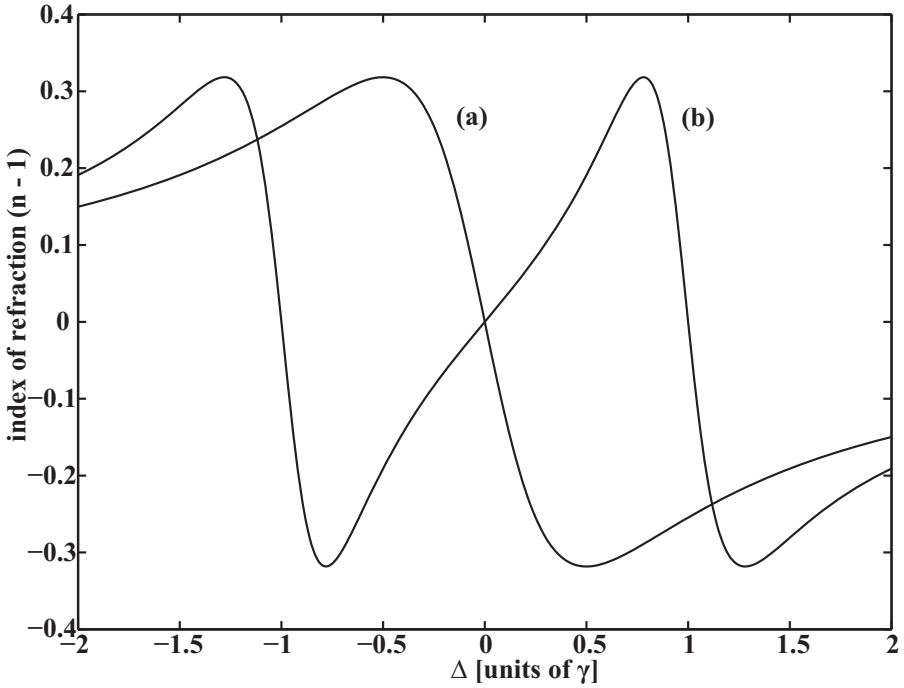

Figure 5.5: Real Part of the Susceptibility. The index of refraction without coupling (a) shows the usual changes between normal and anomalous dispersion. The shape splits like the absorption with a coupling Rabi frequency of $\Omega_c = 2\gamma$ (b) into two features and has a steep slope in the transparent region.

populated it takes several decay times of the state $|c\rangle$ to populate the trapped state [19]. In the case of just state $|a\rangle$ being populated Harris *et al.* [16] found the time for establishing the trapped state to be greater than $1/\Omega_c$.

The effect of coherent population trapping is not only used in EIT experiments, but also for example in laser cooling [28] and for atomic clocks [22].

Classical pictures describes an EIT system with two damped oscillators. Without the interaction of the coupling field both oscillators have the same oscillation frequency ω_0. Turning on the coupling field shifts one oscillation frequency up and the other down. Driving both oscillators at the frequency ω_0 causes a situation where one oscillator is driven above and one below resonance. For sufficiently large splitting between the oscillator frequencies ($>$ several resonance widths) the phases of two damped oscillators are almost opposite. The contributions cancel to a great extent.

Though this picture might be qualitatively right, it is not quantitatively. For small detunings (smaller than the resonance width) the picture does not show the right cancellation any more. Furthermore the classical picture does not explain why the cancellation of absorption can be 100%

For a correct description one has to go back to the reduced differential equations for a two-level-system and extend them to the three-level case with probe Rabi frequency Ω_p and coupling Rabi frequency Ω_c. This set of equations can be solved in the weak field regime by a perturbation expansion. With the usual rotating wave approximation and initial conditions one derives the expectation value of the induced dipole moment. This consequently leads to the polarization and hence to the susceptibility. The complete extensive derivation can be found in Boyd [9].

The real and imaginary part of the susceptibility determine the shape of the absorption line and the index of refraction. They read

$$\chi(\Delta_p) \propto \frac{\Delta_p}{\Omega_c^2 - 4\Delta_p^2 + i2\gamma_p\Delta_p} \tag{5.2.3}$$

with the detuning of the probe field $\Delta_p = \omega_p - \omega_{ac}$, the line width γ_p of the transition $|c\rangle \rightarrow |a\rangle$ and the Rabi frequency of the coupling field Ω_c. Figure 5.4 illustrates the imaginary part of the function $\chi(\Delta_p)$ for two different coupling fields. The case of zero coupling (a) shows the usual Lorentzian line shape. The corresponding index of refraction $(n-1)$ in figure 5.5 changes from normal to anomalous dispersion and back. The steep slope of the curve was interesting to explore but it is practically not accessible due to the high absorption.

In the case of the coupling Rabi frequency being twice the line width $\Omega_c = 2\gamma_p$ (b) one finds the absorption line to be split. In the middle of the two maxima the absorption goes down to zero. This feature leads to EIT. Resonant probe light encounters full transparency. The index of refraction still has a (opposite) steep slope. This can for example be used for creating slow light as the group velocity dispersion is proportional to $n - \lambda(dn/d\lambda)$.

There are numerous different EIT experiments carried out on atomic Rb. The following overview does not claim completeness but intends to point out some important works. We focus on experiments in Rb though this atomic system does not show any fundamental differences to other atoms.

The first observation of EIT in Rb was reported in 1995 by Xiao *et al.* [23]. They have reduced the absorption of the $5S_{1/2} \rightarrow 5P_{3/2}$ transition by 64.4% with a coupling field resonant on the $5P_{3/2} \rightarrow 5D_{3/2}$ transition. Another experiment uses the hyperfine structure for EIT like Scully *et al.* [36]

have demonstrated. The transparency has been established with a comb of short optical pulses introducing the discussed coherences between the hyperfine ground states. Experiments with the strong change in index of refraction have been carried out by Maleki *et al.* [42]. They have studied nonlinear optical properties of EIT in Rb and focussed on the group velocity / EIT resonance dependency on the probe intensity. Welch *et al.* [29] have demonstrated a group velocity of $v_g \approx -80\,\mathrm{m/s}$ and explored the transition of the ultraslow to ultrafast light regime.

The approach to ultrafast EIT is different than described before in the chapter and the cited papers. There is very little work on strong field EIT. The only paper dealing with strong fields is [12].

In strong field physics equation 5.2.3 does not hold true any more as the EIT is not in the pertubative limit. Two different views - a frequency and a time domain perspective - allow us to understand the new mechanisms. It is important in the following consideration that the probe pulse ($5S_{1/2} \rightarrow 5P_{3/2}$) intensity is small in comparison to the coupling pulse ($5P_{3/2} \rightarrow 5D_{3/2}$) intensity.

Sections 4.2 and 4.1 about two-level-atoms and dressed states have given insight into the strong field dynamics of atoms. Rb in our experiment is not a two-level system but a three-level ladder system (see figure 5.1). Nevertheless the theoretical results of these chapters apply here to some extent as the probe field is at least two orders of magnitude weaker than the coupling and does not dress any states.

In the frequency domain perspective the splitting of the absorption line described above for "usual" EIT is introduced by the two-level-atom dynamics. For the first approach it is reasonable to think of the coupling as so strong that it dominates the dynamics of the Rb system. Con-

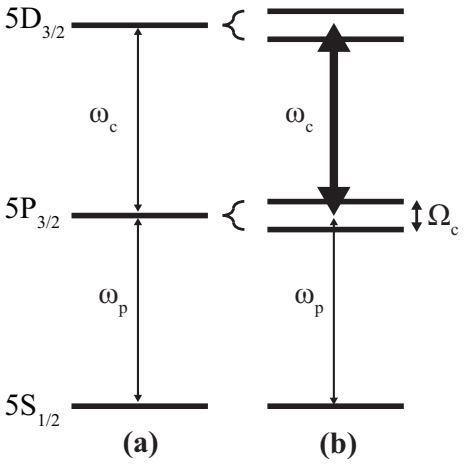

Figure 5.6: EIT Level Splitting Diagram. (a) For a weak coupling field the effect of the dressed states is neglectable and much smaller than the bandwidth of the probe pulse. (b) For a strong coupling field the state $5P_{3/2}$ splints and shifts out of resonance with the probe.

sequently the coupling field interacts with the atomic system and dresses the states of the resonant transition. The bare eigenstates $5P_{3/2}$ and $5D_{3/2}$ of figure 5.6(a) transform into the dressed states $\Psi_{\pm}$ given by equation 4.2.6.

For the coupling field, equation 4.2.3 describes the expectation value of the dipole moment. The oscillation of the dipole happens at the undressed coupling transition frequency ω_c and at two frequencies below and above the transition frequency. These new frequencies occur at $\omega_c \pm \Omega_c$ where Ω_c is the coupling field Rabi frequency. The scheme of the transition frequencies in figure 4.2 changes to the following diagram 5.6(b).

The ground state $5S_{1/2}$ in 5.6(b) remains undressed. Due to the splitting of the intermediate state $5P_{3/2}$ the transition frequency for the probe fields turns into a doublet. Its dipole moment oscillates with the new frequencies $\omega_p \pm 1/2\Omega_c$ above and below the bare resonance. The separation of the splitting is proportional to the coupling field strength.

The linewidths of the states can be neglected in this treatment. They are orders of magnitudes smaller than the bandwidths of the fields and the Rabi frequency Ω_c.

When the coupling field is sufficiently intense the splitting is wide enough to let a noticeable fraction (or the total) of the probe bandwidth pass in between the two absorption peaks corresponding to the dressed states. The width of the split absorption lines and the region of strong change in the index of refraction for a constant coupling Rabi frequency Ω_c is much smaller than the splitting itself. Hence the part of the spectrum between the split levels encounters very low absorption and a small change in group velocity. However the resonant parts of the pulse are absorbed and have a different group velocity. This splitting is known as Autler-Townes Splitting [4].

In the time domain perspective the transparency can be explained by interference of wave functions. First we recall the mechanisms of a two-level-system with the transition frequency ω_0. We define the zero energy as the energy of the ground state. The energy of the excited state is $E_{ex} = \omega_0 \hbar$ such that its phase evolves with the propagator $e^{-i(E_{ex}t/\hbar)} = e^{-i\omega_0 t}$.

We break up the light field with the frequency ω_l in lots of small parts in time. The first part of the field at t_0 excites a small fraction of the ground state to the excited state. This exited state amplitude evolves in the state and picks up a phase.

The next part of the field at $t_0 + \tau$ excites a following fraction of the wave function. Its phase is just determined by the phase of the light field as the ground state does not evolve in phase. The light field phase is proportional to its frequency such that the second fraction of the wave function has the phase

$e^{-i\omega_l \tau}$. The fraction of the wave function in the excited state has evolved in phase during the time τ by $e^{-i\omega_0 \tau}$. Both fractions add up.

If the light field is resonant, namely $\omega_l = \omega_0$, the phase evolution in the excited state exactly is matching the phase of the second excited fraction of the wave function. Without phase difference the two fractions do not interfere and add up constructively.

In the case of a non-resonant field $\omega_l = \omega_0 + \Delta$ the two fractions of the wave function add up with a phase difference of $e^{-i\Delta\tau}$. This leads to partial cancellation of the exited state amplitude. Consequently all parts of the excited wave function have different phases leading to a complete cancellation. This is an explanation of why only resonant fields can transfer population in the limit of long excitation pulse.

EIT experiments are based on the a similar cancellation of wave function. As in this case the probe is resonant, the mechanism for phase mismatch has to be based on the third state.

The probe transition from the ground state $5S_{1/2}$ to the intermediate $5P_{3/2}$ is where the cancellation takes place. At the same time the probe field excites a fraction of wave function, the coupling field takes this fraction and cycles it between the states $5P_{3/2}$ and $5D_{3/2}$. Its field strength is much higher than the probe's whereas the dipole elements are comparable. Thus the higher Rabi frequency of the coupling field implies that the cycling transfer rate is faster than the excitation from the ground state.

Parts of the wave function which come back to the intermediate state $5P_{3/2}$ after the cycling do not have their previous phase. Consequently the following probe field excitation adds up with a phase difference. Generally speaking a strong coupling field randomizes the phase of the intermediate state at a higher rate than the coherent excitation happens.

The cycling can reduce the amount of transferred population dramatically. Section 5.8 on Simulations for EIT in Rubidium shows numerical simulations proving that this mechanism can reduce the effective amount of transferred population by a factor of 50.

The two described pictures give insight into the mechanism of EIT in the strong field regime. However they are based on the assumption that probe and coupling fields just interact with their assigned transitions. Laser pulses from the amplifier system with a bandwidth of 30 nm are not suitable to act as probe and coupling pulses. The pulse shaper is able to create narrow bandwidth pulses with desired width and amplitude within the given wavelength range. Section 5.5 on the Pulse Applicator Program explains this in detail. All explanations up to now have neglected the effects of propagation. Resulting problems and ways to address them are discussed in the following section.

5.3 Simulations for EIT in Rubidium

The first approach to quantify the EIT in Rubidium is founded on simulations. The last section Electromagnetically Induced Transparency 5.2 has introduced the qualitative pictures of how a transition can be rendered transparent.

One step further from the two-level-systems towards a better understanding is the calculation of a three-level-system. To our knowledge there is no analytical treatment of such a system for short and intense pulses. Equation 4.1.7 of the two-level case becomes non-algebraic and cannot be solved analytically any more.

Nevertheless the Schrödinger equation for a three-level-system can be integrated numerically. We use a similar approach as in the two-level-atom and describe the wave function of the system as superposition of the three bare states

$$\Psi(t) = a(t)e^{-i\omega_a t}\Psi_a + c(t)e^{-i\omega_c t}\Psi_c + b(t)e^{-i\omega_b t}\Psi_b \tag{5.3.1}$$

The probabilities to find an atom in the bare states are given by $|a(t)|^2$, $|b(t)|^2$ and $|c(t)|^2$. A light field $\varepsilon(t) = \varepsilon_1(t)e^{-i\omega_1 t} + \varepsilon_2(t)e^{-i\omega_2 t}$ composed of two pulses couples the states. Two- and multiphoton processes are neglected. The time-dependent Schrödinger equation in matrix form reads

$$i\hbar\frac{d}{dt}\begin{pmatrix} a(t)e^{-i\omega_a t} \\ c(t)e^{-i\omega_c t} \\ b(t)e^{-i\omega_b t} \end{pmatrix} = \begin{pmatrix} E_a & -\mu_{ac}\varepsilon(t) & 0 \\ -\mu_{ca}\varepsilon(t) & E_c & -\mu_{cb}\varepsilon(t) \\ 0 & -\mu_{bc}\varepsilon(t) & E_b \end{pmatrix} \begin{pmatrix} a(t)e^{-i\omega_a t} \\ c(t)e^{-i\omega_c t} \\ b(t)e^{-i\omega_b t} \end{pmatrix} \tag{5.3.2}$$

This equation translates with the help of the rotating wave approximation into the equation of motion for the coefficients $a(t)$, $b(t)$ and $c(t)$

$$\frac{\partial}{\partial t}\begin{pmatrix} a(t) \\ c(t) \\ b(t) \end{pmatrix} = \begin{pmatrix} 0 & A & 0 \\ \tilde{A} & 0 & B \\ 0 & \tilde{B} & 0 \end{pmatrix} \begin{pmatrix} a(t) \\ c(t) \\ b(t) \end{pmatrix} \tag{5.3.3}$$

with the terms $A, \tilde{A}, B, \tilde{B}$ defined by the dipole moments $\mu_{ac} = \mu_{ca}$ and $\mu_{bc} = \mu_{cb}$, the two envelopes of the fields $\varepsilon_1(t)$ and $\varepsilon_2(t)$ and the detunings of the

fields 1 and 2 from the transitions $a \rightarrow c$ and $b \rightarrow c$

$$A = -\mu_{ac}\left[\varepsilon_1(t)e^{-i\Delta_{ac,1}t} + \varepsilon_2(t)e^{-i\Delta_{ac,2}t}\right] \tag{5.3.4a}$$

$$\tilde{A} = -\mu_{ac}\left[\varepsilon_1(t)e^{+i\Delta_{ac,1}t} + \varepsilon_2(t)e^{+i\Delta_{ac,2}t}\right] \tag{5.3.4b}$$

$$B = -\mu_{cb}\left[\varepsilon_1(t)e^{-i\Delta_{cb,1}t} + \varepsilon_2(t)e^{-i\Delta_{cb,2}t}\right] \tag{5.3.4c}$$

$$\tilde{B} = -\mu_{cb}\left[\varepsilon_1(t)e^{+i\Delta_{cb,1}t} + \varepsilon_2(t)e^{+i\Delta_{cb,2}t}\right] \tag{5.3.4d}$$

The first order differential equation 5.3.3 can be integrated numerically. In this case Matlab® 7.1 is used. The integration code was written to explore different important parameters for the simulation. Running the program provides either the population of the three levels in time or the final population of the levels in dependence of intensity and pulse delay between two pulses.

Goal of the program is to determine whether a coupling field (in the sense of chapter 5.2) can reduce population transfer on the probe transition. The code allows us to study how the interaction of the coupling influences the dynamics of the system. Less population transfer on the probe transition would imply a reduction of absorbed photons and hence lead to transparency. The program does not include propagation effects as the described model does not comprise changes in the field.

The code determines the electric field envelope from the two input parameters maximum field strength and wavelength full width half maximum(FWHM). The wavelength FWHM translates into a temporal FWHM via the assumption that the pulse is Gaussian in shape and has a flat phase (transform limited: $\Delta\omega \cdot \Delta t \ = 0.44$).

The actual differential equation is integrated with the built-in function ode23. This function allows us to integrate explicitly time-dependent first order differential equations given in matrix form. It would be possible to use Runge-Kutta 4^{th} order instead, but the possible gain in computing time would not compensate for the possibility to scale the ode23 in relative and absolute tolerance.

In the first operation mode the program generates a one dimensional time array which is fine enough to integrate the equations with the required accuracy. It matches the field envelopes to this time array and passes all information to ode23.

As this simulation does not comprise absorption (the electric field remains unchanged) we need to examine the atomic state dynamics to get insight about EIT. One good alternative measure for absorption is the amount of transferred population. It is proportional to the amount of absorbed photons as long as no stimulated emission occurs. To study this behavior the probe pulse is

chosen to be a π pulse (compare equations 4.1.14), meaning that it inverts the population of its transition completely. This is definitely not the way the experiment should be set up but it increases the contrast of the simulations.

Note that spontaneous emission is and can be neglected. Coupling and probe wavelength FWHM are chose to be close to experimental values as 1 nm and 0.5 nm respectively. Both pulses are centered in time such that their temporal overlap is maximal.

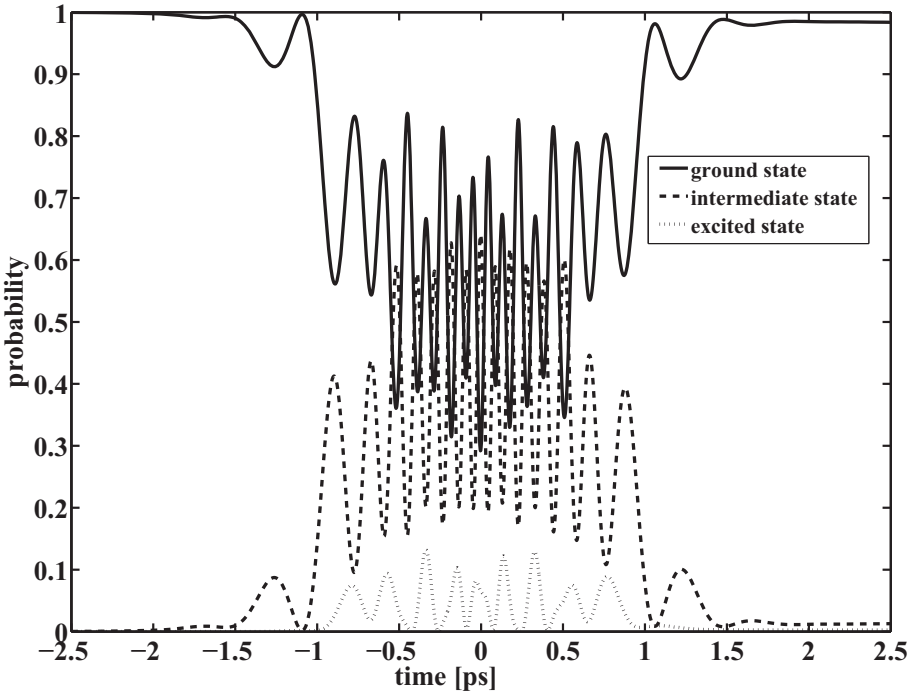

Figure 5.7: Simulation of the Time Development of the Population of Rb in EIT Experiment. The probe is a π pulse and the coupling has a field strength of $1.4 \cdot 10^8\,\mathrm{V/m}$. The coupling pulse almost completely prevents the probe from population transfer into the $5P_{3/2}$ state. In the end the population in the ground state is 98.5%.

Figure 5.7 illustrates the population dynamics with a coupling pulse with a maximum field strength of $1.4 \cdot 10^8\,\mathrm{V/m}$. This value is presumably high as the probe pulse is a π pulse. In the experiments the effects can be found for smaller field strength.

In the beginning of the interaction (negative times) population of the the ground state $5S_{1/2}$ is started to be pumped into the intermediate state $5P_{3/2}$. As soon as the coupling field turns on and cycles the $5P_{3/2} \rightarrow 5D_{3/2}$ transition, the coherence between ground $5S_{1/2}$ and intermediate state $5P_{3/2}$ is destroyed. Hence following population excited from the ground state adds up with the intermediate wave function in distorted phase. This process causes fast oscillations in the populations. In the end of the interaction the remaining population in the intermediate state $5P_{3/2}$ declines and settles at about 1.5%. The population in the excited state $5D_{3/2}$ is neglectably small. Hence the efficiency of the population transfer has been reduced by more than a factor of 50. This result leads to the expectation that the overall absorption of photons is reduced by about the same factor.

The second operation mode of the code generates a two dimensional array of time delay and field strength values. A time delay corresponds to a shift of one of the pulses in time in respect to the other. This allows us to determine how important the temporal overlap is and how the EIT appears for partial temporal overlap. In the field strength dimension, the intensity of the probe is held constant, but the coupling is ramped in strength. It gives insight in how the EIT scales with coupling intensity.

Figure 5.8 depicts the result of a time delay of -2 ps to +2 ps and a maximal field strength of $1.5 \cdot 10^8$ V/m. The time delay dimension shows that the interaction between the two pulses is on the order of 2 ps. This is a little less than the sum of the pulses FWHMs (2.67 ps) and fulfills the expectations that the effects occur when the pulses overlap significantly. With higher coupling field strengths the temporal interaction becomes longer.

The field strength dimension shows robust prevention of population transfer for field strengths greater than $3 \cdot 10^7$ V/m. We can run the simulations with smaller probe intensities decreasing the coupling threshold for prevention of population transfer a little. However the contrast of the simulations decreases as well.

We want to determine whether the influence of the coupling pulse on the $5S_{1/2} \rightarrow 5P_{3/2}$ transition is important. Therefore a modified simulation is carried out shown in figure 5.8. The new simulation suppresses the coupling pulse affecting to the probe transition and vice versa. This was done by changing the Hamiltonian in the following way. In equations 5.3.4 the terms for the far detuned field envelopes are removed and therefore the cross talking of the pulses is eliminated. The result of the new simulation is shown in figure 5.9. We find the overall behavior to be different from the other simulation. Just two peaks with highly suppressed population transfer occur, the depth of the minimum between them is strongly dependent of the coupling pulse wavelength band-

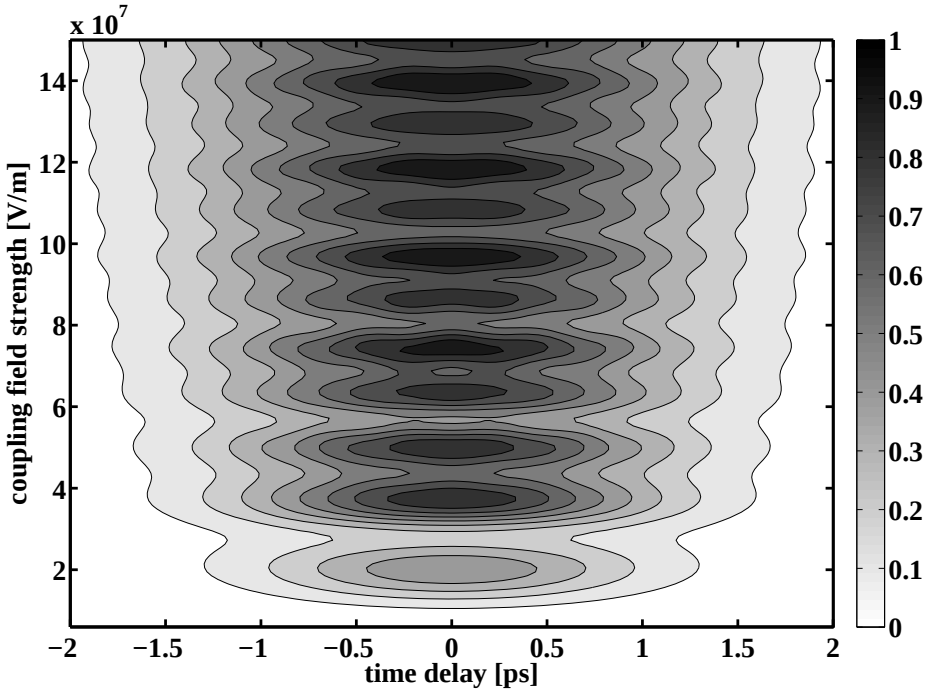

Figure 5.8: Simulation of the Population of the Ground State in Rb in EIT Experiment. For small coupling field strength the probe exhausts the ground state completely (π pulse). For strong coupling pulses the ground state population is close to one. The temporal FWHM is about $\pm 1ps$ and therefore close to the sum of the pulses FWHMs.

width. Broader bandwidth of the coupling pulse than in the simulation shown in 5.9 leads to less pronounced minima. A coupling FWHM of 3 nm fills the gaps nearly completely and hence produces a uniform population transfer suppression for the probe pulse for all coupling field strengths above the threshold of $3 \cdot 10^7$ V/m.

Our conclusion from this result is that the cross talking cannot be neglected in the experiment. Though further calculations show that coupling pulses with intensities used in the experiment do not transfer population on the probe transition, the coupling field can still enhance or degrade the suppression of population transfer depending on the choice of pulse FWHMs. Later measurements show that this is mainly due to the coupling Stark shift of the probe transition.

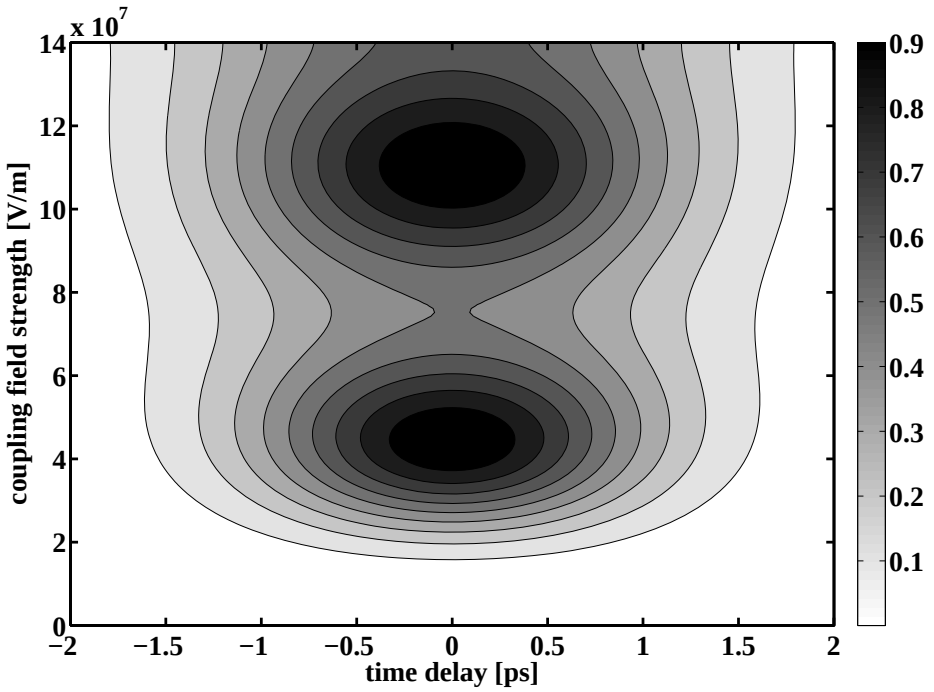

Figure 5.9: EIT Simulation Ground State 2. The coupling field just interacts with the coupling transition and the probe field just with its transition. The overall behavior is different. The simulation proves that the cross talking cannot be neglected with this set of parameters.

As mentioned before, these simulations have some limitations and assumptions which do not hold true in the experiment. The most severe one is that the simulations do not take into account propagation. Effects of the propagation effects can be guessed from figure 5.7. Though the final population of the ground state is close to 100% for intermediate times it goes down to 30% and oscialltes very fast. This behavior implies that the light field excites population by absorption on the $5S_{1/2} \rightarrow 5P_{3/2}$ in the first half of these cycles. In the second half most of the excited population is transferred back into the field by stimulated emission. This process has a strong influence on the propagation of the pulse.

The second assumption not holding true is that the time delay between the pulses is constant through the whole interaction. As a direct consequence of propagation the group velocities of the two pulses depend on the index of refraction which is coupled to the shape of the absorption line (see section 5.2 about EIT). With the atoms behaving as shown above, the probe pulse is

resonant on a populated transition and hence sees a strong structure in the index of refraction. In contrast the coupling pulse is in fact resonant, but its two transition states are almost empty (when using a probe pulse with an area $\ll \pi$). This implies that the two pulses propagate with different group velocities.

One more problem is that in the experiment the field strength of probe and coupling are not constant in space. Our beams usually have a Gaussian profile. For a setup with focusing, the longitudinal beam diameter changes as well. Both circumstances lead to intensity volume averaging.

The overall conclusion from the simulations is that there can be a robust region in the time delay - field strength space with strongly suppressed population transfer when the effects of the problems mentioned above are minimized. Absolute values for the field strength threshold for EIT cannot be named, but they indicate the order of magnitude for the field strength in the experiment. The values for time delay are reasonable and give some guidance for the experiment although they do not account for propagation.

5.4 EIT Setup

The setup of the Rb EIT experiments involves the pulse shaper, an imaging system, the Rb cell and the spectrometer. A sketch is shown in figure 5.10.

A 30 fs pulse is generated by the laser system centered at 780 nm. The pulse shaper is used to create the coupling and probe pulses at 776 nm and 780 nm respectively by cutting out narrow bandwidth fields. The next chapter 5.5 about the Pulse Applicator Program explains the process in detail.

It is important for the Rb experiment to create a long Rayleigh range for the focus of the beams in the cell. This reduces the effect of longitudinal intensity averaging. In comparison to previous setups with a strong focus into the cell we find a strongly reduced influence of the averaging with the current setup. To obtain the long Rayleigh range a 1000 mm lens is used to focus the beam coming from the pulse shaper.

The following imaging system with a 300 mm lens projects the focus into the cell with a magnification of about 3.7. This combination of optics allows us to create a reasonably small spot size with a sufficiently long Rayleigh range.

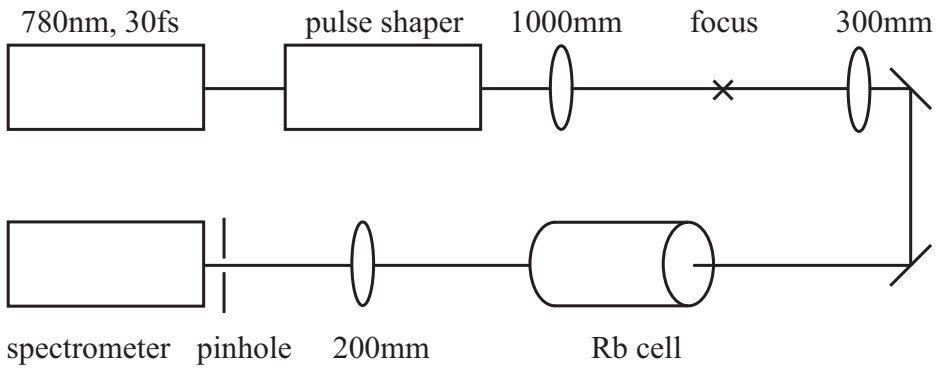

Figure 5.10: EIT Setup with Rb cell. The laser system produces a 30 fs laser pulse which the pulse shaper turns into coupling and probe pulses. A lens focuses with a long focal length. The focus is imaged into the Rb cell having a long Rayleigh length. The center of the cell is imaged onto the pinhole in front of the spectrometer.

Every Gaussian beam focused by an optic has a diffraction limited beam waist. In the limit of small angles its radius (HWHM[1]) for the electric field is

$$w_0 = \frac{\lambda f}{r\pi} \tag{5.4.1}$$

with the wavelength λ, the focal length f of the focusing optic and the beam radius r on the optic. The distance between beam waist with radius w_0 and the point where the beam radius has increased to $\sqrt{2}w_0$ is called Rayleigh range z_R

$$z_R = \frac{\pi w_0^2}{\lambda} \tag{5.4.2}$$

In an imaging setup with magnification M the new waist $w_0^{'}$ and Rayleigh range $z_0^{'}$ are

$$w_0^{'} = M w_0 \tag{5.4.3a}$$

$$z_0^{'} = M^2 z_0^{'} \tag{5.4.3b}$$

[1]half width at half maximum

Using equations 5.4.1 to 5.4.3b the resulting beam diameter in the focus in the cell is about 440 μm with a Rayleigh range of 195 mm.

The glass cell contains Rb without a buffer gas. It is heated by heating elements wrapped around the exterior of the cell. We can adjust the cell temperature between $21°C$ and $200°C$. Figure 5.2 shows the gas density as a function of temperature and equation 5.1.1 gives the vapor pressure in the cell. Aluminum foil wrapped around the heating elements and the cell insulates the setup. The windows of the cell are the only parts which cannot be shielded. To prevent them from extensive cooling, two insulated extending metal tubes have been added to the cell in the beam direction and create a buffer zone. A thermocouple measures the temperature at the outer surface of the cell. The length of the cell is 60 mm which is about 15% of twice the Rayleigh range. This implies that changes in the beam diameter throughout the interaction region are on the order of 6%.

A second imaging system projects the light from the cell onto the 75 μm pinhole in front of the spectrometer. There is no magnification. The pinhole selects the center of the beam reducing the problem of transverse intensity averaging. Furthermore the 10 μm slit of the spectrometer in the vertical plane increases the spatial selectivity in the beam. Both apertures together reduce the effect of transverse intensity averaging to a tolerable amount.

The spectrometer is the USB spectrometer HR4000 from the company OceanOptics. Its spectral range spans from 696 nm to 884 nm with a total of 3648 pixels. We measured with a slit width of 10 μm the spectral resolution to be 0.16 nm at 780 nm. The integration time can be chosen from 4 ms upwards; spectra can be averaged. An inbuilt dark signal subtraction allows us to take spectra without background signal. The noise level is according to the manufacturer below 3%. We can confirm the noise level for optimal operation but measured a slightly higher value for disadvantageous integration values and too long USB cables. In all our measurements we paid attention to avoid these problems.

5.5 Pulse Applicator Program

The EIT experiment depends strongly on the possibility to control the amplitude and phase of the light field in frequency and time. In earlier chapters (see 2.2, 3.1) the abilities and methods of manipulating the light field with an acousto-optical modulator were discussed. This chapter describes the implementation in form of a LabVIEW® program for the particular needs of the EIT experiment.

The first and most important feature of the program is the possibility to selectively vary the spectral intensity. As mentioned above, the broadband (30 nm) light of the amplifier is used to obtain multiple pulses with narrow bandwidths ($\sim$ 1 nm).

All changes induced by the AOM are controlled by a 1 GHz arbitrary waveform generator (AWG) with 1 ns sampling. This signal is created from an array of 8500 values for both time and phase which is send to an digital to analog converter. The output array length is chosen to correspond to 8500 ns such that the 3.4 cm width of the crystal is filled with the propagating acoustic wave (acoustic velocity 4200 m/s) when the light pulse arrives. This results in a mapping of the 8500 pixel of the array to first time in the high frequency signal and following via acoustic wave velocity to different spots in the crystal and hence to wavelengths. All in all pixels map to wavelengths unambiguously.

The idea behind the LabVIEW® program is to set most of the 8500 amplitude pixels to zero with the possibility to change small fractions of about 200 values in between. In this case the acoustic wave is just non-zero at particular positions in the crystal. These positions are chosen such that they pick out the right wavelengths for the experiment.

The program allows us to create three of these wavelength windows. Every window is defined by its initial and final value. As wavelength to space mapping in the crystal is very sensitive to alignment these values are not preset but can be chosen manually. Furthermore this offers the possibility of detunings. The amplitude between the initial and final value is determined by 10 amplitude sliders whose values are interpolated. This allows us to fine tune the shape of the pulse.

Additionally there are settings for an overall gain, a parallel offset of the window and a global on/off.

Figure 5.11 shows the dialog for one frequency window. The amplitude array is set high between pixels 2700 and 2900. As all sliders are up to full

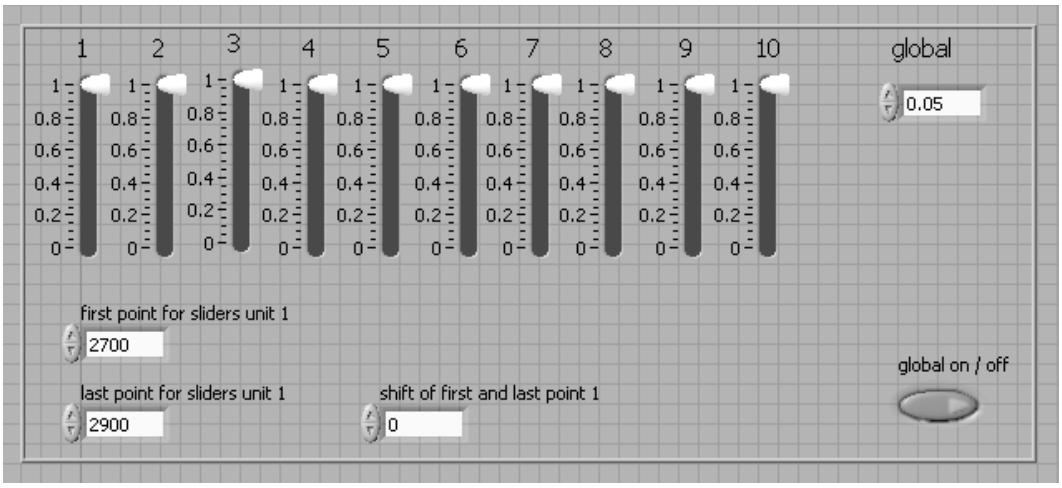

Figure 5.11: Dialog of Pulse Applicator Program. The settings allows to determine the shape of a particular part of the high frequency signal. Initial and final pixels can be set and 10 sliders dictate the amplitude shape. In addition the overall amplitude and an offset can be changed.

value the shape of the frequency window is a simple square function. The overall gain is set to 0.05, there is no offset. Three of these windows can be used for probe, coupling and a reference pulse.

The second feature of the code is the possibility to introduce a time delay between the pulses. Equation 3.1.3 has shown that a linear phase in the frequency domain translates into a proportional delay in the time domain.

Due to conservation of energy and momentum the phase of the acoustic wave in the crystal is transferred to the light field. As mentioned before every of the 8500 amplitude pixels of the array corresponds to a particular wavelength. This also holds true for phase pixels. Non-zero values for these pixels lead to a phase in the acoustic wave and hence are transferred to the light field.

The output of the AWG therefore can be written as

$$f(t) = A(t) \sin\left(\nu_0 t + \phi(t)\right) \tag{5.5.1}$$

with the amplitude pixel array A, the phase pixel array ϕ and the carrier frequency $\nu_0 = 150\,\mathrm{MHz}$. In the program ϕ is zero for all pixels in which the probe and the reference window lie. Just the coupling pulse is delayed with respect to the probe pulse by a non-zero slope in the phase array as shown in figure 5.12. The reason for this is space time coupling in the pulse shaper.

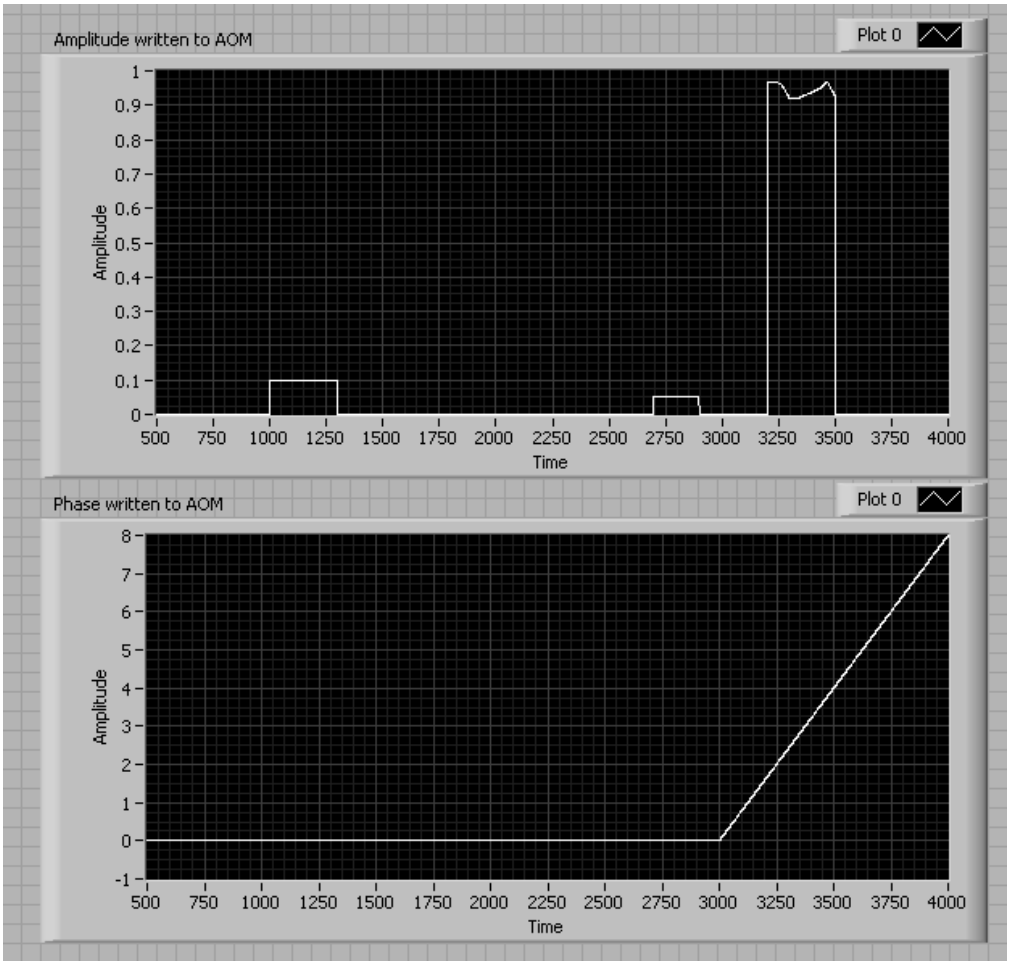

Figure 5.12: Amplitude and Phase Array. The two plots show a section of the amplitude array (upper graph) composed by three frequency windows and a section of the phase array (lower graph) with a linear phase for the coupling pulse.

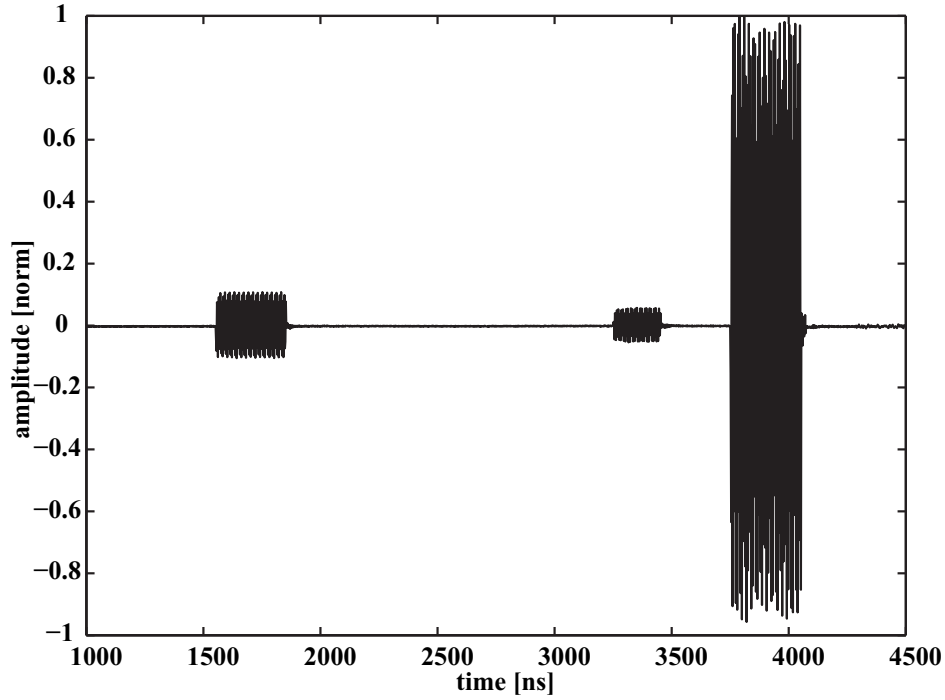

Figure 5.13: Pulse Applicator Output. The high frequency signal is measured with the scope. The zero point of the time axis does not exactly match the beginning of the wave. For the right window the amplitude is not constant like seen before in the amplitude array of figure 5.12.

Figure 5.12 shows a section of amplitude and phase array. The amplitude array (upper graph) was composed of three windows. The right window is the coupling with a shaped amplitude (sliders are not at full values). The other two are the probe and a reference pulses. The output of the AWG measured with an oscillator can be seen in figure 5.13. A change in the frequency of the carrier wave due to the phase can just be seen when zoomed in as it is small in comparison to the carrier frequency. The slope in the phase array (lower graph in figure 5.12) starts between probe and coupling pulse such that just the coupling is influenced. The calibration of the phase slope is given by 5.5.4.

The spectral FWHM of a pulse, created by a window, depends on the pixel width. For windows broader than 50 pixel the FWHM scales linearly with the width. Below 50 pixels the FWHM settles at about 0.45 nm. Figure 5.14 shows the interesting region for the experiment below 100 pixels.

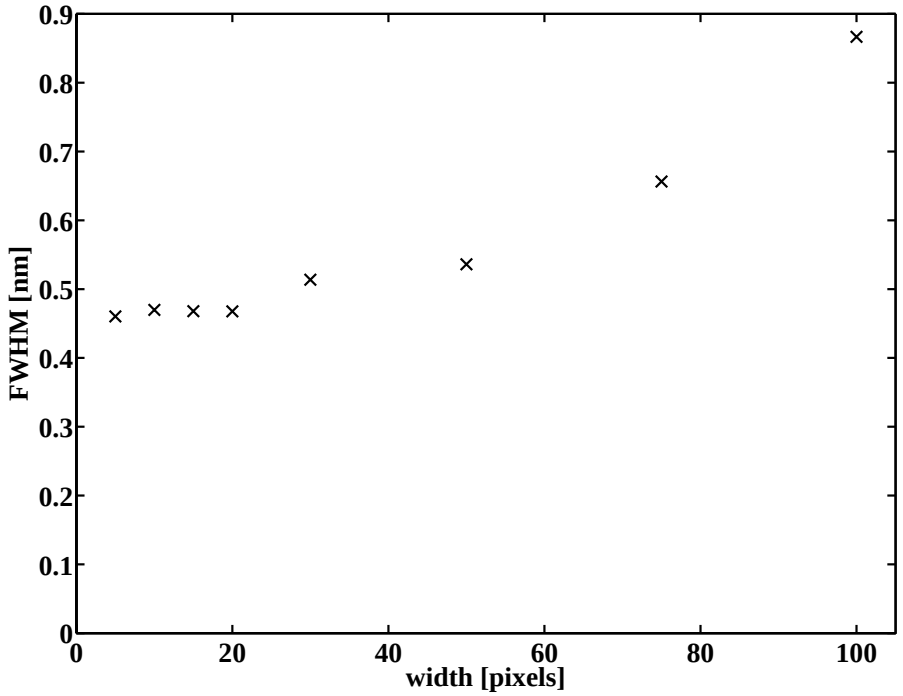

Figure 5.14: Resolution of the AOM. For windows broader than 50 pixels the wavelength FWHM scales linearly with pixels. For smaller windows the FWHM settles at about 0.45 nm.

We find that the behavior of the FWHM does not come from the AD converter or any following amplification device. The high frequency signal can resolve a few pixels.

In conjunction with this the maximal amplitude of the pulse declines rapidly for pixel width smaller than 75 pixels. Figure 5.15 shows this behavior.

The entrance slit of the AOM is about 3.3 mm long covering a total of 65 nm of the spectrum. Knowing the spectral FWHM of the AOM resolution (0.45 nm) we can calculate the spatial FWHM of the crystal resolution

$$0.034\,\mathrm{m} \cdot \frac{0.45\,\mathrm{nm}}{62\,\mathrm{nm}} = 2.3 \cdot 10^{-4}\,\mathrm{m} \tag{5.5.2}$$

Equation 5.4.1 gives the diffraction limited spot size on the AOM crystal. The mirrors of the pulse shaper have a focal length of 750 mm and the beam

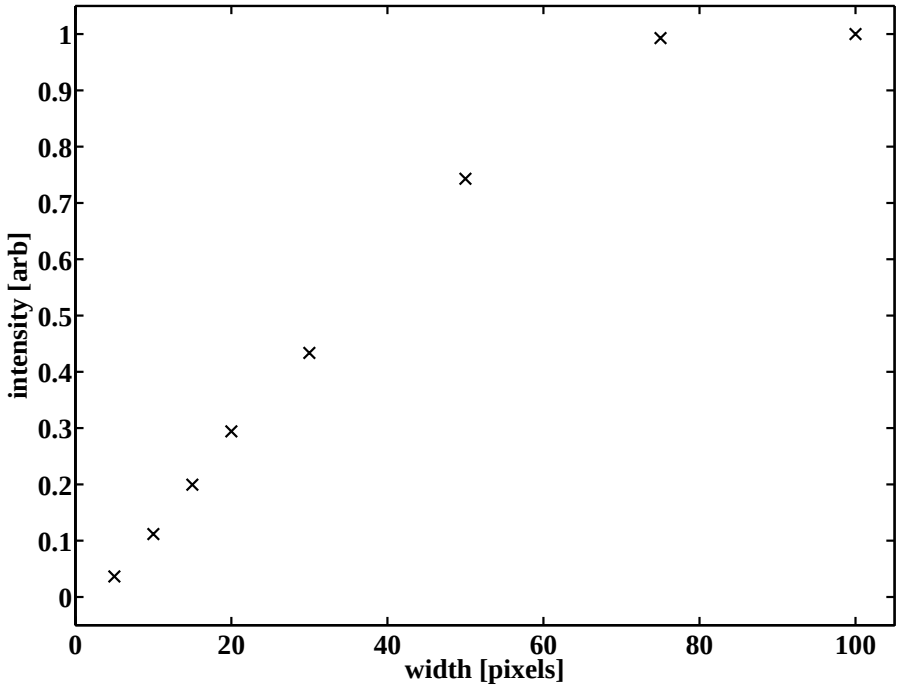

Figure 5.15: Intensity of the Diffracted Wave from the AOM. For windows smaller than 75 pixels the intensity declines almost linearly with the width showing the limitations of the diffraction process in the crystal.

size is 1.5 mm. The diameter (FWHM) for intensity at the focal point is

$$d = 2/\sqrt{2} \cdot w_0 = 1.8 \cdot 10^{-4}\,\mathrm{m} \tag{5.5.3}$$

Taking into account that the spot size is just an estimation, the mode of the laser is not perfect and the beam has a Rayleigh range it seems likely that the resolution of the pulse shaper is optically limited.

For the time delay calibration of the Pulse Applicator phase slope two delayed pulses at different wavelength were measured with the FROG. The resulting autocorrelation of two delayed pulses has four peaks. Two are at time zero (no path length difference between the two pulses) with the peaks being centered at half the wavelength of the input pulses (note: the signal is the SH light). The other two peaks are at plus and minus the delay time centered at half the average wavelength. Figure 5.16 shows a FROG trace for

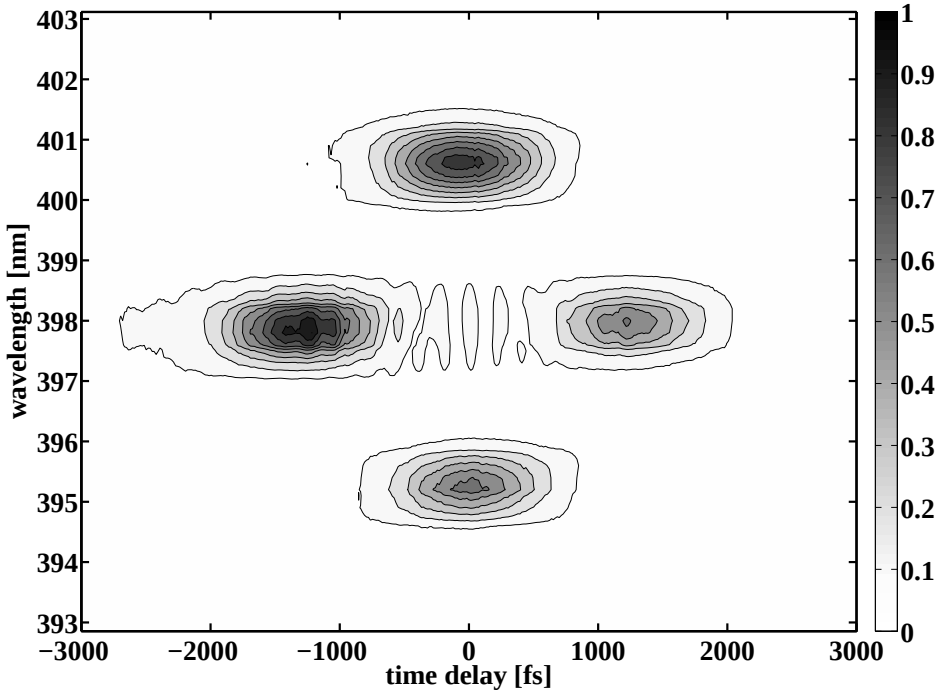

Figure 5.16: Pulse Applicator Time Delay Calibration. The FROG trace shows the autocorrelation for two pulses delayed by 1200 fs. The wavelength axis is not correct.

a phase slope of 8 in the Pulse Applicator. This corresponds to a time delay of 1200 fs. The wavelength axis is not right as the FROG program has problems to read out the spectrometer wavelength data, which is of no influence on this measurement. Six traces have been taken and give a slope delay conversion factor of

$$d_{ps} = (150 \pm 8)\,\mathrm{fs/unit\,slope} \tag{5.5.4}$$

The autocorrelation is by definition symmetric in time. For two given pulses the delay can be determined but not the order of the pulses. Hence the time delay is undefined in sign. To find the order of the pulses we measured two more correlation delay scans.

The first scan was carried out with a 150 μm BBO crystal. Two beams at different wavelength were generated and delayed in respect to each other with the pulse shaper. Both beams overlap in the crystal and produce blue SH

light. A spectrometer takes traces of the SH signal. The cooperative signal is maximal for best overlap, hence this measurement determines the phase slope at which both pulses arrive at the crystal at the same time. As predicted this value is very close to zero.

The second scan was carried out with the former setup and a 2 cm thick glass optic. It is inserted before the crystal to introduce a dispersive time delay. Glass has a normal dispersion for wavelengths around 780 nm causing the shorter wavelengths to come out later ($n_{\lambda_1} < n_{\lambda_2}$ for $\lambda_1 > \lambda_2$). In the measurement the maximum shifts towards positive delay times. This implies that for these positive numbers the pulse shaper sends out smaller wavelength first (always corresponding to the coupling pulse in our experiment).

5.6 Measurements

We carry out several measurements to characterize the effect of the coupling pulse on the interaction of the pump pulse with the Rb gas.

One assumes that the two pulses have different group velocities in the Rb cell. The probe pulse encounters a spectral structure in the index of refraction because the transition comprises the populated ground state. However the transition of the coupling pulse does not include a populated state. Therefore the probe pulse has a slower group velocity than the coupling pulse. Figure 5.17 shows a cross correlation between the two pulses before and after the Rb cell.

A second harmonic generation crystal is placed at either front or back side of the cell producing a blue doubled signal from the pulses. The cooperative signal is recorded with a spectrometer at different delay times. For best temporal overlap between probe and coupling pulse in the crystal the signal is maximal and decreases for every other delay time.

Figure 5.17 shows a maximum close to zero delay time for the crystal before the cell indicated by the dashed line. This means that the pulses are - as expected - very well overlapped without delay from the pulse shaper.

However the solid line indicates the same measurement with the crystal after the cell. We find the the probe pulse to be retarded by about 5 ps in respect to the coupling pulse. Additionally the shape of the right wing of the cross correlation has broadened implying that the probe pulse is not just slowed down but also reshaped in its temporal profile.

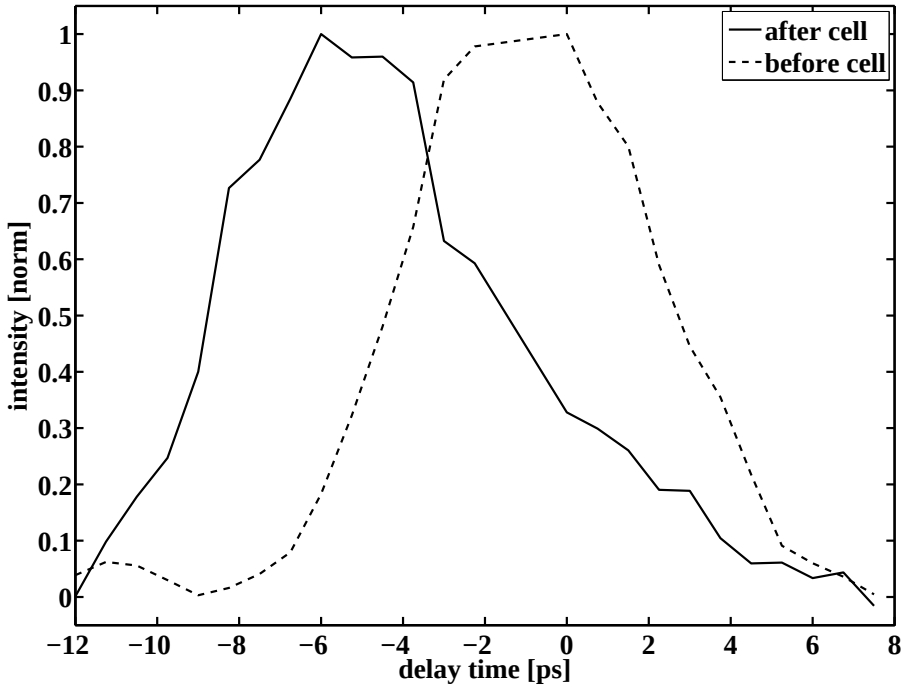

Figure 5.17: EIT Group Velocity. The two curves show the cross correlations of the pulses before and after the cell. The dashed line indicates the measurement before the cell. After the cell (solid line) the maximum in the cross correlation has shifted by 5 ps indicating that the transition through the cell delays the probe pulse by this amount.

The coupling pulse used in the following measurements has a duration of about $\tau = 3.5\,\mathrm{ps}$, the probe pulse is three times shorter. These values are derived from the cross correlation measurement shown in figure 5.17. The figure does not show the coupling pulse used in the measurement below but a similar one with smaller bandwidth. We can derive from the this measurement the pulse duration of the coupling pulse used in the 2D scan. The error of this value is about 30%.

The maximal field strength of the coupling pulse ε_{max} is estimated from the measured energy of the pulse $U = 1.6\mu\mathrm{J}$, the pulse duration τ and the radius of the spot size in the cell $r = 220\,\mu\mathrm{m}$ (see section 5.4)

$$\varepsilon_{max} \approx \frac{1}{r}\sqrt{\frac{2U}{\pi\varepsilon_0 c\tau}} = 4.7 \cdot 10^7 \mathrm{V/m} \tag{5.6.1}$$

Here c is the speed of light and ε_0 the the dielectric permittivity. There is an error of 35% on the pulse energy as the used power measuring device is operated at its very limit. Together with the error of the pulse duration these two quantities dominate the uncertainty. The total error of ε_{max} is 39%.

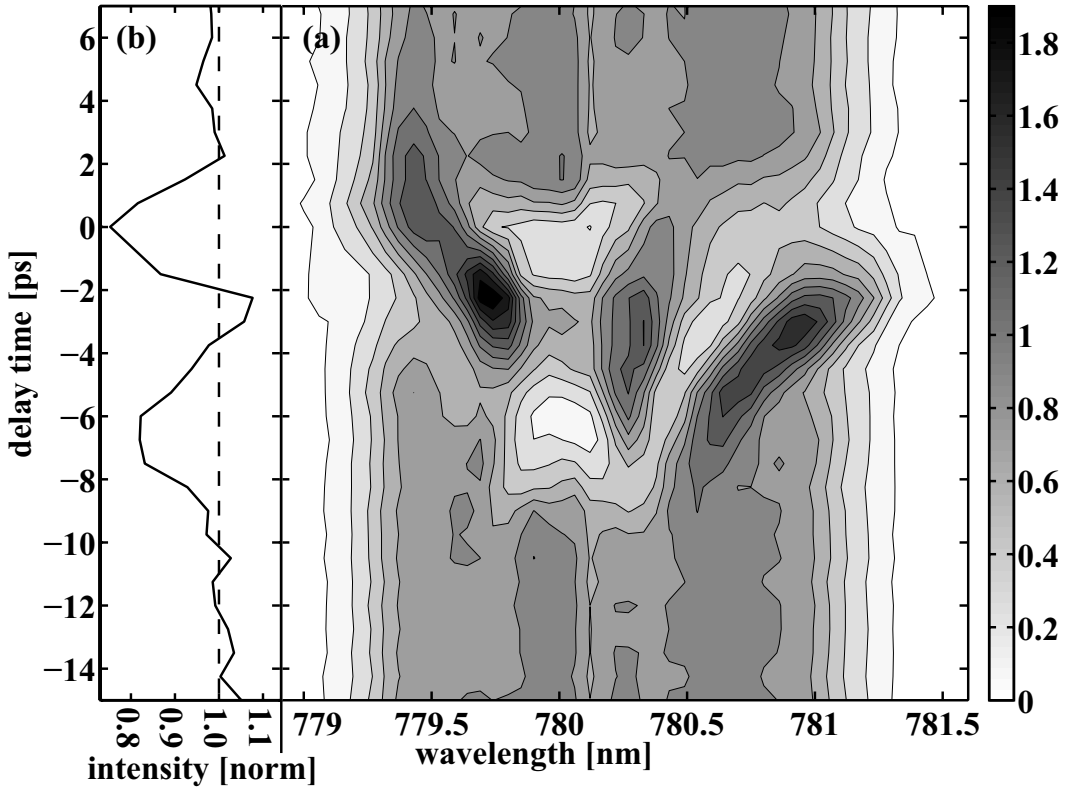

Figure 5.18: EIT Time Delay Scan. (a) shows the probe spectrum as a function of time delay between coupling and probe pulse. Around -3 ps the regular absorption line changes into a symmetric structure of three gain and two absorption regions. (b) shows the projection of the data onto the delay time axis. For 0 ps and -7 ps the probe pulse shows a reduction of 20% in integrated intensity whereas for -3 ps there is none.

The 2D scan 5.18(a) displays the spectrum of the probe pulse as a function of coupling pulse time delay. Using the pulse shaper we vary the time delay between -15 ps and +7 ps to cover all possible pulse sequences. For positive numbers the coupling pulse arrives at the cell before the probe pulse, for negative numbers vice versa.

All spectra at different delay times are normalized with a reference pulse centered at a frequency far away from the transitions (not visible in the scan). This guarantees a comparability of intensity throughout the scan.

The data shows an absorption line at 780 nm in the spectrum for extreme delay times like -14 ps or 6 ps. As discussed before in section 5.4, the 0.16 nm resolution of the spectrometer is not capable of resolving the shape of the absorption line which is much smaller. We measure the convolution of the line shape with a 0.16 nm broad distribution. This explains why the absorption line appears as a broad but shallow reduction.

For delay times around -3 ps the data indicates a strong, completely different interaction of the probe pulse with the Rb gas. This value is in good agreement with the EIT group velocity measurement (figure 5.17). The 2D scan shows the average interaction of the probe pulse for all places and hence all delay times in the cell arising from different group velocities. One expects the interactions to be strongest if the coupling pulse (which propagates faster) is retarded by the pulse shaper by half the delay of 5 ps the probe pulse picks during its passage.

The data at -3 ps shows a threefold structure slightly displaced to higher wavelengths stretching over an interaction delay range of 9 ps. The peak in the middle of the spectrum is shifted in respect to the absorption line. Two regions of absorption occur to the sides of the center peak going over to regions of stimulated emission at the edges of the probe spectrum.

We project the data on the time axis. Figure 5.18(b) shows this integrated intensity as a function of the delay time. The curve is normalized to delay times without interaction (-14 ps and +6 ps).

For times between -8 ps and -4 ps and also between -2 ps and +2 ps the probe and coupling pulses are partly overlapped and cause losses. With best overlap at -3 ps the integrated intensity has its maximum. The explanation for the behavior is developed in the following section.

The integrated intensity is good indication that the coupling pulse does not transfer population on the probe transition. If this was the case the curve would have an offset for positive delay times when the coupling pulse comes before the probe. Furthermore simulations similar to those in section 5.8 show that the coupling field is sufficiently far detuned from the probe transition to excite any significant amount of population on this transition.

Looking at lineouts of the 2D scan helps to quantify the observed structure. Figure 5.19 shows two lineouts with different delay times. The solid line is taken from -15 ps and represents the probe spectrum with the regular absorption line (broadened by the finite spectrometer resolution). The dashed line shows the spectrum at -3 ps. Its shape shows the threefold structure. The

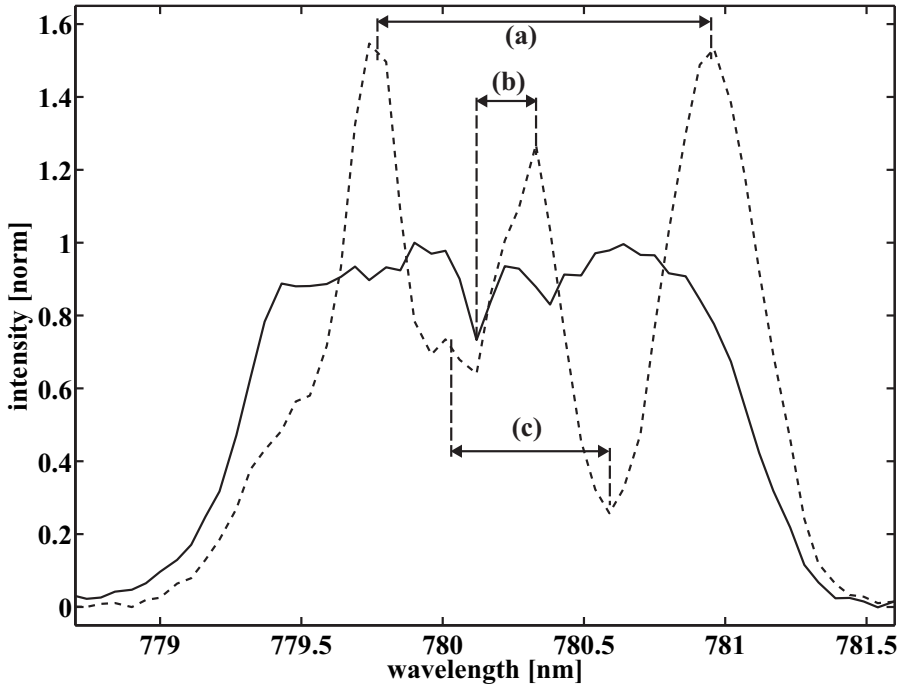

Figure 5.19: EIT Time Delay Scan Spectra. The solid line shows the spectrum for the probe pulse without interaction, the dashed line shows the spectrum at a delay time of -3 ps. Separation (a) is the splitting for the emission peaks, separation (b) indicates the Stark shift and separation (c) is the splitting between the absorption regions.

middle peak is AC Stark shifted by 0.2 nm (b) from the transition to longer wavelengths. This is caused by the coupling pulse which has a negative detuning (shorter wavelength) on the probe transition and hence pushes the probe transition towards longer wavelengths (see [43, 45]).

We calculating the AC Stark shift S_{AC} with equation 4.2.18 for the probe transition. The coupling field strength is $\varepsilon_{max} = 4.7 \cdot 10^7 \mathrm{V/m}$ and the wavelength detuning $\Delta_\lambda = 4\,\mathrm{nm}$ translates to a frequency detuning of $\Delta_\omega = 2.0\,\mathrm{THz}$. The calculation yields $S_{AC} = 0.15\,\mathrm{THz}$ corresponding to a wavelength shift of 0.30 nm. Given the fact that the two pulses shift in time in respect to each other during their passage through the cell one expects the probe to see an averaged Stark shift.

We have not solved the Maxwell-Bloch equations to describe the propagation effect. An estimation for the average intensity overlap indicates that the

actual Stark shift should be about half of the value calculated for the maximal field strength ε_{max}. Given the large uncertainty in the field strength the measured and calculated values agree.

Two regions of strong absorption occur in figure 5.19 to the sides of the middle peak separated by 0.6 nm (c). They have a width much broader than a linewidth of a transition. Even further to the sides two symmetric regions of stimulated emission appear at a separation of 1.2 nm (a). Their spectral intensities are about 50% higher than for the solid line.

The occurrence of absorption and stimulated emission symmetrically around the shifted transition is caused by the split dressed states discussed in section 5.2 on EIT. We therefore calculate the Rabi frequency, which is the splitting separation, with the coupling field strength ε_{max}. We obtain $\Omega_c = 1.1\,\mathrm{THz}$ corresponding to a wavelength splitting of 2.1 nm. Again we have to take into account that the scan averages over many different pulse delays in the cell. In this case the averaging is in the field strength which varies slower around the peak than the intensity. The measured value should be about one third smaller than the calculated value. Additionally we have to take into account that this value has got an error of 39% from the field strength.

The following section 5.7 on the time domain picture shows that the separations (a) and (c) are on the order of the maximal splitting but can be smaller by a factor of two or three. The time domain picture explains in detail the mechanisms leading to the change from absorption to stimulated emission and their relative position in the spectrum.

5.7 Time Domain Picture of Ultrafast EIT

The data presented in the last section is best understood in a time domain picture. We therefore have a closer look at the temporal evolution of the phases of the system.

When coupling and probe pulses overlap in time, state $5P_{3/2}$ splits according to section 5.2 into the dressed states such that probe pulse sees two new transition frequencies at $\omega_{d1,2}(t) = \omega_p \pm 1/2\Omega_c(t)$. Note that this frequency is - like the coupling Rabi frequency - time dependent. The probe light field however is tuned to the middle of these frequencies at ω_p.

We define the ground state as zero energy. Thus the phases of the dressed states are described by $e^{-i(\omega_{d1,2}(t))t} = e^{-i(\omega_p \pm 1/2\Omega_c(t))t}$ whereas the the light field phase is $e^{-i\omega_p t}$. One of the phases of the dressed states advances and the other falls behind the excitation field. In the rotating frame of the field its phase is

constant and the states evolve with the phase $e^{\mp i(1/2\Omega_c(t))t}$.

Usually, in the case of long excitation times, a phase mismatch like this leads to cancellation of population in the excited state. When field and state are in phase light is absorbed. The phase difference develops and a short time later field and state are π out of phase. Hence the light field stimulates emission. This alternation between absorption and emission repeats very rapidly. Averaging over many cycles for long excitation times prevents from effective population transfer. Additionally dephasing processes like for instance spontaneous emission or collisions randomize the phase such that the coherence between field and state is reduced.

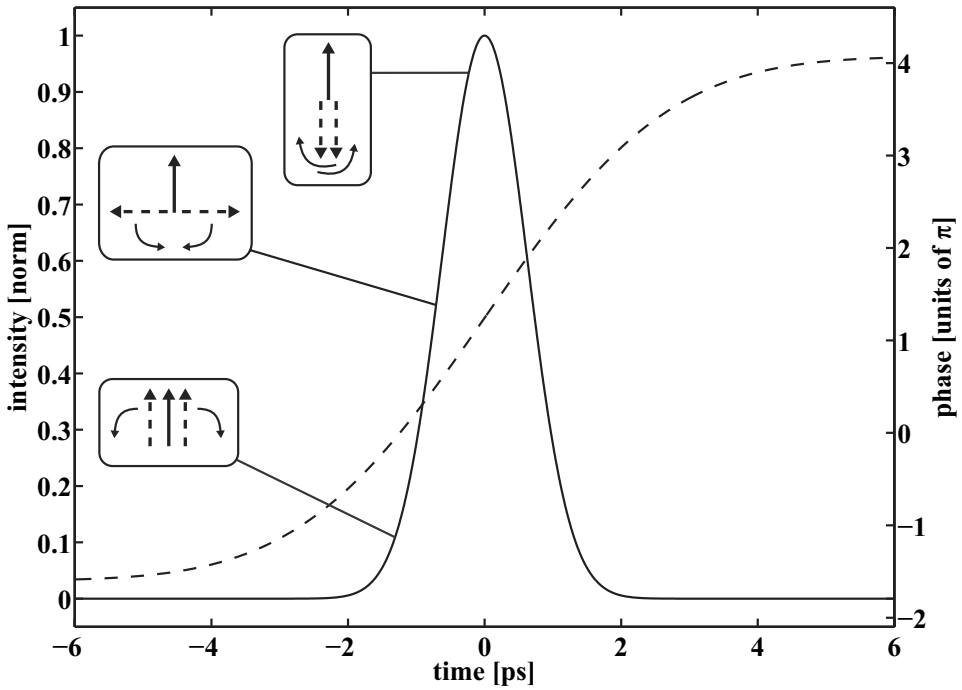

Figure 5.20: EIT Phase Evolution. The absolute value of the phase of the dressed states in the rotating frame $|\Phi_{1,2}(t)|$ is shown with the dashed line. The solid line indicates the intensity of the coupling pulse. Solid arrows in the insets represent the (constant) phase of the field, dashed arrows the phases of the dressed states. The evolution of the phases during the probe pulse duration switches between absorption and stimulated emission.

The ultrafast EIT experiment is different from this behavior in two fundamental ways:

During the short duration of the probe field the phase evolves just by a few π. In this case absorption and emission do not necessarily cancel any more. Dephasing on this time scale is very small.

Even more important is the fact that the dressed state splitting is not constant in time but changes with the time dependant coupling Rabi frequency $\Omega_c(t)$. Though the coupling pulse has a longer duration than the probe pulse its field strength changes significantly during the interaction time of the probe pulse. This means that the transition frequency between ground state and dressed states varies on the same time scale as the evolution of the phase. Consequently absorption happens at different frequencies than stimulated emission. Both processes do not cancel any more but redistribute light between frequencies.

To quantify this statement we calculate the phase of the dressed states in the rotating frame at any given point in time for pump and probe pulse having no delay

$$\Phi_{1,2}(t) = \mp 1/2 \int_{t_0}^{t} \Omega_c(\tau) d\tau \tag{5.7.1}$$

Here t_0 is the starting time of the probe pulse. We assume that both pulses have a Gaussian profile in time and use the maximal field strength ε_{max} for the coupling field. Figure 5.20 shows the phase as dashed line and the normalized intensity of the probe pulse as solid line. The zero point of the phase difference is set such that it is at the beginning of the probe pulse.

Field and states at this time are in phase such that light is absorbed (lower inset). As the coupling pulse is longer than the probe pulse its field strength is at about 60% at this time. Likewise the dressed states splitting should have developed that far. Consequently the probe pulse is being absorbed at two frequencies above and below the undressed transition frequency at about 60% of the maximal splitting $\Omega_{c\,max}$. With increasing coupling field strength the absorption lines are pushed further out leading to absorption feature much broader than usual transition lines. They can be regarded as summation of many absorption lines close to each other. Simultaneously the phases increase and reduce the strength of the absorption.

When the phases have evolved to $\pi/2$ (intermediate inset) absorption and stimulated emission cancel each other. However the excited state keep their population from the previous absorption.

The splitting and phase develop further such that now stimulated emission dominates. At the time when the probe pulse intensity is about 95% of its maximum the phase difference has evolved to π causing just stimulated emission (upper inset). The light which has been absorbed in the first part of the interaction is now reemitted. However the coupling field strength and hence the dressed states splitting is maximal now. The stimulated emission happens at frequencies even further apart from the undressed transition frequency.

This cycle between absorption and stimulated emission happens once again in the second half of the pulse. Frequencies at intermediate splittings of the dressed states are absorbed and now reemited with a smaller splitting.

This mechanisms of absorbing light at intermediate splittings and emitting it at both maximal and small splittings explains the threefold structure of figures 5.18 and 5.19. One can see in the 2D scan that the stimulated emission is not limited to the bandwidth of the probe pulse but can create new frequencies.

There is no general need for the circumstance that absorption happens at intermediate splittings and stimulated emission happens around the extremum of the splitting. The number of cycles between absorption and emission and their positions in the spectrum depends on the relation of the durations of the pulses and the field strength of the coupling pulse. These values have been given in the last section with a large error. It could well be that the phase difference in figure 5.20 during the probe pulse duration evolves over a slightly different number.

The spectrum in figure 5.19 actually might even show at the very left edge the beginning of a second absorption cycle in the probe spectrum indicating that the phase evolution is faster than calculated.

To predict the exact shape of the probe pulse after the passage through the cell we have to average once again over all delay time sequences which occur due to the different group velocities. Additional one has to take into account that probe and coupling pulses are not Gaussian in their temporal profile. To good approximation the profile is the Fourier transformations of their spectra. These are determined by the pulse shaper and tend to have steeper flanks than a Gaussian distribution. The probe pulse presumably changes its profile during the passage due to dispersion. Reliable predictions could be made with the Maxwell-Bloch equations.

For delay times with poor averaged overlap between probe and coupling pulse the phase evolution of the dressed states is much smaller. The situation occurs when the probe pulse in figure 5.20 is centered at for example $\pm 4\,\mathrm{ps}$. In this case the phase just evolves by about $\pi/2$ implying that absorption

never changes to stimulated emission. Hence the excited population stays in the state after the passage of the pulse and decay by spontaneous emission. This leads to losses in the integrated probe spectrum intensity. Figure 5.18(b) shows this behavior for delay times of -6 ps and 0 ps.

Chapter 6

Broadband Excitation in Rubidium

Up to now we have discussed the interaction of narrow bandwidth light fields with Rb atoms. The response of the system is completely different when using the entire 30 nm bandwidth of the laser. These short intense pulses can drive a population inversion on the $5S_{1/2} \rightarrow 5P_{3/2} \rightarrow 5D_{3/2}$ ladder system which leads to superfluorescence. A detailed discussion of what superfluorescence is and how it occurs follows in section 6.2.

Experiments on Rb with broadband ultrafast lasers have been carried out by several groups. Noordam *et al.* have studied the excitation along the $5S_{1/2} \rightarrow 5P_{3/2} \rightarrow 5D_{3/2}$ ladder system with frequency sweeps [10] and have explained the exact mechanism of adiabatic rapid passage (ARP) for a 9 nm bandwidth laser centered at 780 nm [25]. These experiments do not include the state $5P_{1/2}$. Sauerbrey *et al.* [31] have carried out pump-probe[1] experiments on the Rb system including the state $5P_{1/2}$ and find a strong chirp dependence of the excitation.

Our interest in the broad bandwidth excitation of Rb started with observing strong coherent emission after excitation with the full spectrum of the laser. Figure 6.1 shows a typical spectrum of the beam after the Rb cell. The excitation light is centered at 778 nm and spans from 745 nm to about 800 nm.

The spectrum shows three interesting features: (b) and (c) are lines of strong coherent emission which have not been in the spectrum before the cell. In the section 6.2 about superfluorescence we discuss the characteristics of the light. The wavelength of the two superfluorescence peaks match exactly the $5S_{1/2} \rightarrow 5P_{3/2}$ and $5S_{1/2} \rightarrow 5P_{1/2}$ transitions from the ground to the intermediate states in Rb. The absorption feature (a) is at the wavelength of the $5P_{3/2} \rightarrow 5D_{3/2}$ transition from the intermediate to the exited state.

[1] pump-probe experiments excite an atomic / molecular system with a pump pulse and explore the changes in the system with a delayed probe pulse

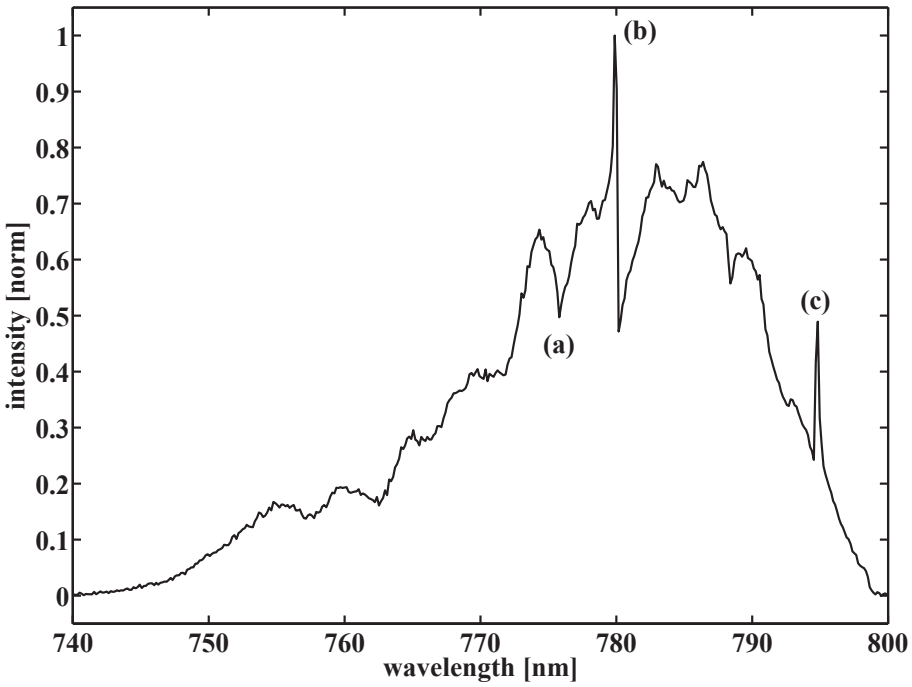

Figure 6.1: Superfluorescence at 795 nm and 780 nm. Strong coherent superfluorescence light overlays the excitation spectrum (no chirp). The two emission lines (b) and (c) are at the wavelength of the $5S_{1/2} \rightarrow 5P_{3/2}$ and $5S_{1/2} \rightarrow 5P_{1/2}$ transitions. Absorption feature (a) corresponds to the $5P_{3/2} \rightarrow 5D_{3/2}$ transition.

Line (b) furthermore shows a strong asymmetric shape with a change from emission for lower wavelength to absorption for higher wavelength. Warren *et al.* [15] have reported similar line shapes for propagation of laser pulses in optically dense Rb.

We have also found superfluorescence at 420 nm on the $6P_{3/2} \rightarrow 5S_{1/2}$ transition as shown in figure 6.2. This blue light appears when the system is excited via two photon absorption. A part of this population decays to the state $6P_{3/2}$ with emission at 5720 nm. From here the superfluorescence occurs. Work on a similar system in Na [45] has demonstrated yoked superfluorescence in a ladder system. This could also be the case in Rb, but we do not have the means to measure the light at 5720 nm.

The next sections explain superfluorescence and the excitation mechanism.

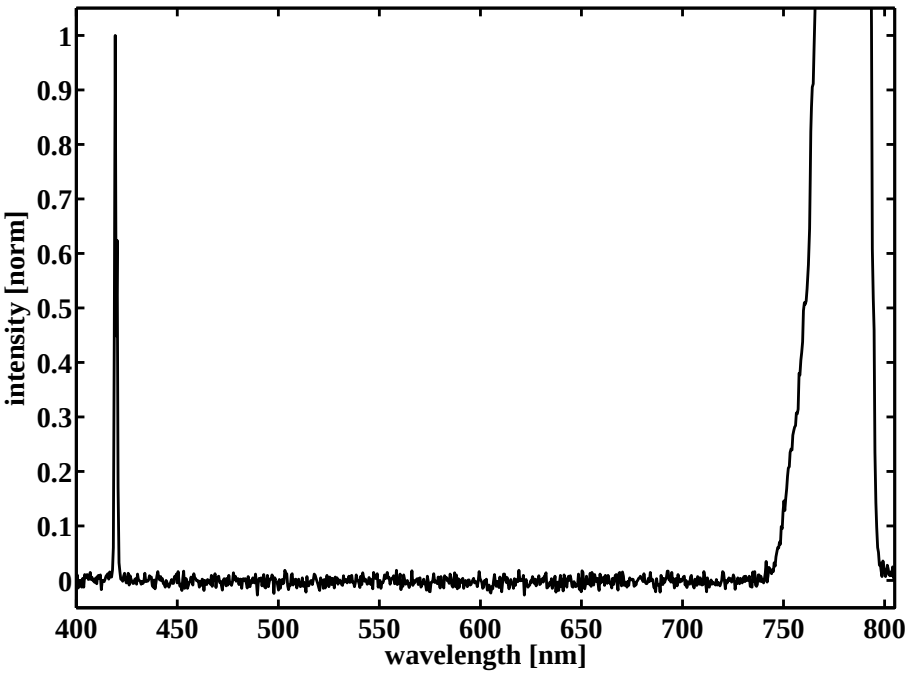

Figure 6.2: Superfluorescence at 420 nm. The spectrum shows the excitation pulse around 780 nm and the superfluorescence on the $6D_{3/2} \rightarrow 5S_{1/2}$ transition at 420 nm.

6.1 Excitation Mechanisms

The excitation mechanism is presumably an adiabatic following of dressed states. It is called adiabatic rapid passage (ARP, see for example [43]) as the time scale is fast in comparison to dephasing mechanisms. Noordam *et al.* demonstrate ARP in Rb for the $5S_{1/2} \rightarrow 5P_{3/2} \rightarrow 5D_{3/2}$ ladder [25].

We intend to understand the excitation paths along the various level in the Rb system and their nature. ARP is based on a sweep of the frequency from below the resonance to above the resonance. A chirped pulse can lead to the same effect. Therefor we carry out chirp scans and observe the emitted light.

Like all other lasing processes we assume the superfluorescence to be non-linear in the population inversion. Therefore it is not well suited as indicator

for the absolute amount of transferred population. However the superfluorescence intensity should be monotonically increasing with inversion and indicates significant population transfer.

We define the intensity $I_0 = \frac{1}{2} c\varepsilon_0 \left(\varepsilon(t)\right)^2 = 3.3 \cdot 10^{12}\,\mathrm{W/m^2}$ with the dielectric permittivity ε_0 as the minimal intensity of the excitation pulse for observing superfluorescence in figure 6.1.

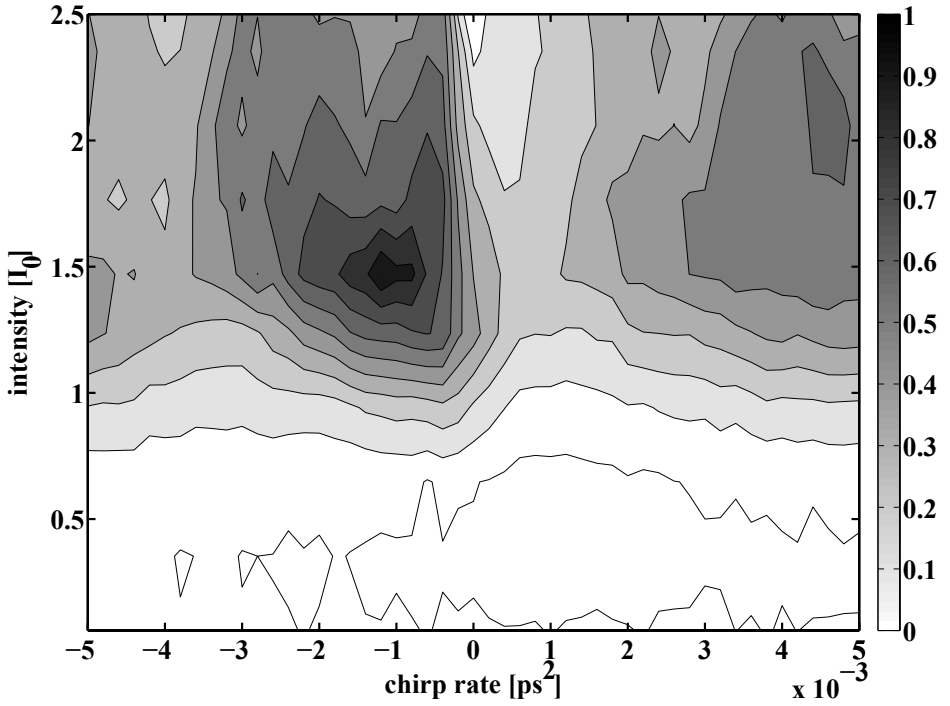

Figure 6.3: Superfluorescence Scan at 780 nm. The amount of coherently emitted light on the $5S_{1/2} \rightarrow 5P_{3/2}$ transition (780 nm) is maximal for small negative chirp rates at $1.5I_0$. Positive chirp rates are less effective where small positive chirp rates have poor transfer. Efficient emission begins with the defined intensity I_0.

Figure 6.3 shows a chirp scan on superfluorescence at the $5S_{1/2} \rightarrow 5P_{3/2}$ transition (780 nm). The energy in the superfluorescence peak on the spectrum is measured and plotted against the chirp rate and the intensity of the excitation pulse. Neighboring wavelength are used to subtract out the excitation light such that just the peak on top of the spectrum is integrated. The figure shows the results for chirp rates between -0.005 ps^2 to 0.005 ps^2 with an

intensity between zero and $2.5I_0$.

Appearance of superfluorescence starts with I_0. The most efficient production of superfluorescence happens for small negative chirp rates. The effect increases with intensity up to about $1.5I_0$ and declines for higher intensities. Positive chirp rates also are producing superfluorescence, however they are less effective. Especially small chirp rates do not yield much emission.

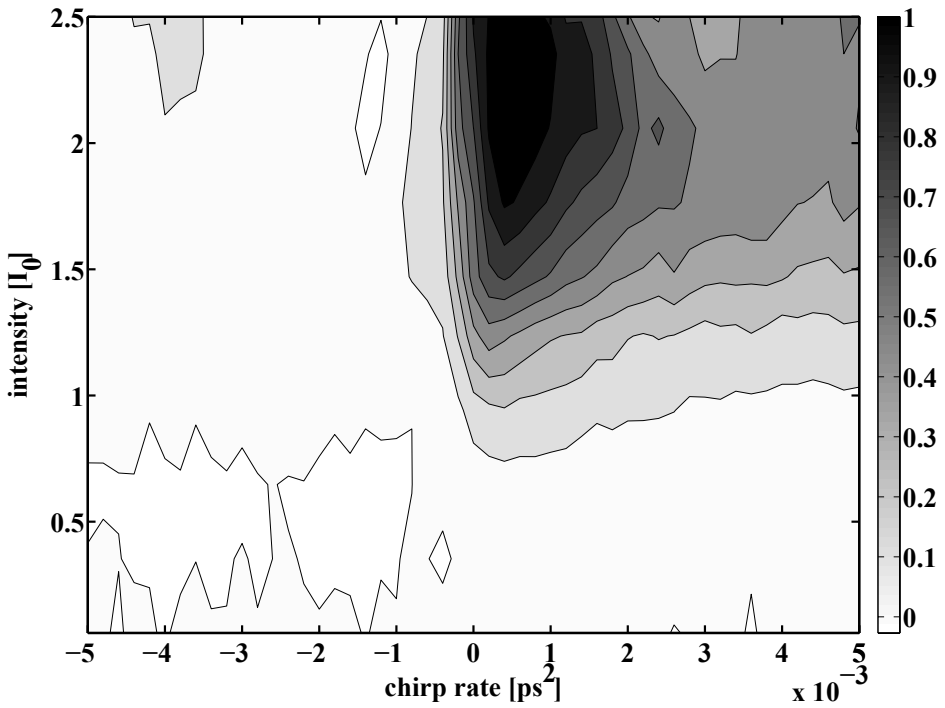

Figure 6.4: Superfluorescence Scan at 795 nm. The amount of coherently emitted light on the $5S_{1/2} \rightarrow 5P_{1/2}$ transition (795 nm) shows a very pronounced asymmetry. Positive chirp rates excite efficiently and lead to superfluorescence, negative chirp rates suppress the population transfer completely such that no superfluorescence occurs.

Figure 6.4 is the corresponding scan for the $5S_{1/2} \rightarrow 5P_{1/2}$ transition (795 nm). The plot shows a strong asymmetry in the superfluorescence yield. Positive chirp rates lead to strong emission without a clear optimal intensity as in the case of the previous $5S_{1/2} \rightarrow 5P_{3/2}$ transition. For negative chirp rates there is no light implying that population transfer to the state $5P_{1/2}$ does not exceed the superfluorescence threshold.

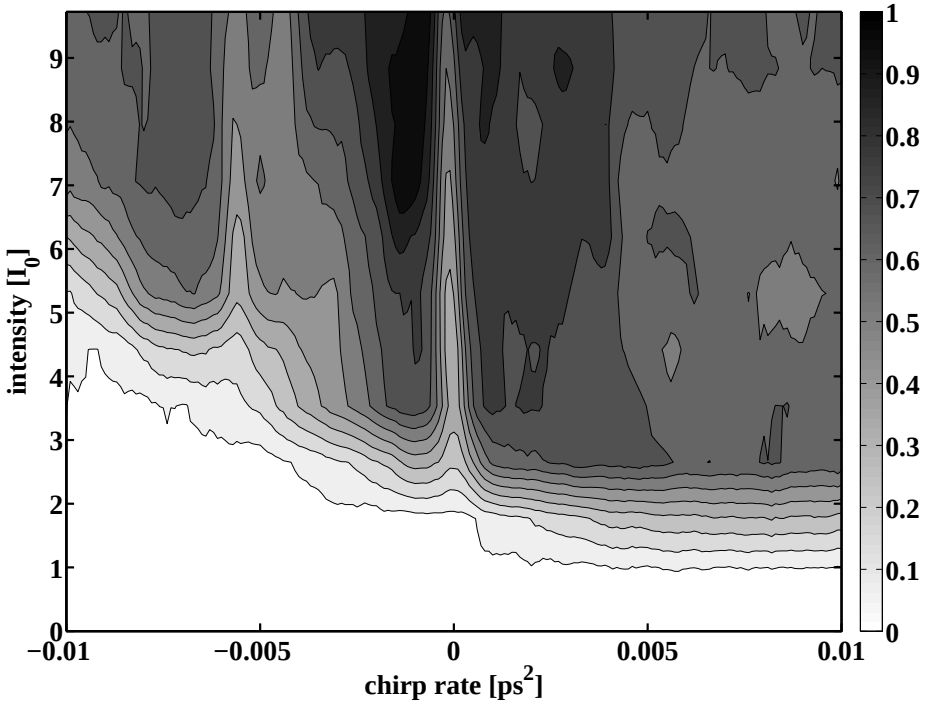

Figure 6.5: Superfluorescence Scan at 420 nm. The amount of coherently emitted light on the $6P_{3/2} \rightarrow 5S_{1/2}$ transition (420 nm) is a measure for the population in the excited state $5D_{3/2}$. For positive chirp rates the system is excited almost chirp independently for intensities higher than $1.5I_0$. For negative chirp rates the system stays much longer in diabatic states and is transfered for intensities higher than $2.5I_0$ to $5I_0$.

Population from state $5D_{3/2}$ decays along the ladder $5D_{3/2} \rightarrow 6P_{3/2} \rightarrow 5S_{1/2}$. The transition $6D_{3/2} \rightarrow 5S_{1/2}$ has a wavelength of 420 nm which we measure as superfluorescence. (Scholten *et al.* [27] have reported on blue upconversion in Rb with light at 420 nm.) With the current setup we do not have the means to measure the light at 5720 nm from the $5D_{3/2} \rightarrow 6P_{3/2}$ transition.

Figure 6.5 shows the chirp scan on the blue light. The scan ranges from -0.01 ps^2 to 0.01 ps^2 with an intensity between zero and $9.6I_0$. For positive chirp rates the emission from state $6P_{3/2}$ starts for intensities of about $1.5I_0$. Small chirp rates lead to slightly better yields than greater ones, but the overall dependence on the chirp rate is not very strong. From about $2.5I_0$ the superfluorescence almost saturates.

For negative chirp rates the turn on is shifted to higher intensities. Efficient production of superfluorescence happens dependent on the chirp rate for intensities between $2.5I_0$ and $5I_0$. The best transfer is again found for small values. This behavior for negative chirp rates is in agreement with Noordam [25]. For pulses with zero chirp rate the population transfer efficiency is reduced.

To understand the detailed dynamics of the system we examine the Rb system in the dressed state picture discussed in chapter 4.2. With four levels and four transitions the system is too complex for analytical approaches like the two-level-atom. Numerical results however can be retrieved from the Hamiltonian in the interaction picture.

We consider the Hamiltonian for the Rb system with all four levels for the light field $\varepsilon(t) = \frac{1}{2}\varepsilon_0(t)\,(e^{-i\omega t} + e^{+i\omega t})$. The dipole moments for the transitions are given in table 5.1. $\mu_{P_{1/2}\to D_{3/2}}$ has to be estimated and is set to be $1/5\,\mu_{P_{3/2}\to D_{3/2}}$.

$$H(t) = \begin{pmatrix} E_{S_{1/2}} & \mu_{S_{1/2}\to P_{3/2}}\varepsilon(t) & \mu_{S_{1/2}\to P_{1/2}}\varepsilon(t) & 0 \\ \mu_{S_{1/2}\to P_{3/2}}\varepsilon(t) & E_{P_{3/2}} & 0 & \mu_{P_{3/2}\to D_{3/2}}\varepsilon(t) \\ \mu_{S_{1/2}\to P_{1/2}}\varepsilon(t) & 0 & E_{P_{1/2}} & \mu_{P_{1/2}\to D_{3/2}}\varepsilon(t) \\ 0 & \mu_{P_{3/2}\to D_{3/2}}\varepsilon(t) & \mu_{P_{1/2}\to D_{3/2}}\varepsilon(t) & E_{D_{3/2}} \end{pmatrix} \tag{6.1.1}$$

The rotation matrix U for the transformation into the interaction picture redefines the zero energy at the state $5P_{3/2}$ and shifts the remaining levels such that their energy is given by their detuning.

$$U(t) = \begin{pmatrix} A & 0 & 0 & 0 \\ 0 & B & 0 & 0 \\ 0 & 0 & C & 0 \\ 0 & 0 & 0 & D \end{pmatrix} \tag{6.1.2}$$

with the coefficients

$$A = \exp\left[-i\left(-\omega_{S_{1/2}} + \Delta_{S_{1/2}\to P_{3/2}}\right)t\right] \tag{6.1.3a}$$

$$B = \exp\left[-i\left(-\omega_{P_{3/2}}\right)t\right] \tag{6.1.3b}$$

$$C = \exp\left[-i\left(-\omega_{P_{1/2}} + \Delta_{S_{1/2}\to P_{3/2}} - \Delta_{S_{1/2}\to P_{1/2}}\right)t\right] \tag{6.1.3c}$$

$$D = \exp\left[-i\left(-\omega_{P_{3/2}} - \Delta_{D_{3/2}\to P_{3/2}}\right)t\right] \tag{6.1.3d}$$

We apply the transformation $H_i = U^{-1}(t)H_s(t)U(t) - i\hbar U(t)\dot{U}^{-1}(t)$ and then the rotating wave approximation. The resulting interaction Hamiltonian is similar to 4.2.13 and reads

$$H_i(t) = \frac{\hbar}{2}\begin{pmatrix} 2\Delta_{S_{1/2}\to P_{3/2}} & \Omega_{S_{1/2}\to P_{3/2}}(t) & \Omega_{S_{1/2}\to P_{1/2}}(t) & 0 \\ \Omega_{S_{1/2}\to P_{3/2}}(t) & 0 & 0 & \Omega_{P_{3/2}\to D_{3/2}}(t) \\ \Omega_{S_{1/2}\to P_{1/2}}(t) & 0 & 2\left(\Delta_{S_{1/2}\to P_{3/2}} - \Delta_{S_{1/2}\to P_{1/2}}\right) & \Omega_{P_{1/2}\to D_{3/2}}(t) \\ 0 & \Omega_{P_{3/2}\to D_{3/2}}(t) & \Omega_{P_{1/2}\to D_{3/2}}(t) & -2\Delta_{P_{3/2}\to D_{3/2}} \end{pmatrix} \tag{6.1.4}$$

The eigenenergies of the four dressed states can be obtained by diagonalizing the Hamiltonian H_i. We are particularly interested in the change of the eigenenergies with central wavelength of the pulse. In the case of a chirped pulse (see chapter 3.1 on chirped pulses) the light field starts at one end of the spectrum and sweeps through to the other.

Figure 6.6 illustrates the numerical results for diagonalizing this interaction Hamiltonian for a field strength of $\varepsilon_0 = 5 \cdot 10^7\,\mathrm{V/m}$ which corresponds to the intensity I_0.

The central wavelength spans from 775 nm to 805 nm covering all avoided crossings in the states. Solid lines show the eigenenergies of the dressed states. For comparison the dotted lines show the energies of the bare states.

The figure explains the transfer mechanisms, especially for chirped pulses. For negative chirp rates (short to long wavelength) the system follows the dashed arrow (a). The population starts in the ground state $5S_{1/2}$ with short wavelengths. It continues along the dressed state with increasing wavelength. At the first avoided crossing the system can go both ways: remaining in the dressed state or pass diabatically to the neighboring dressed state. For long wavelengths in the end of the pulse one finds the system in both the intermediate state $5P_{3/2}$ and the excited state $5D_{3/2}$.

The avoided crossing to the third dressed state (ending in the $5P_{1/2}$ state for long wavelength) is so pronounced that population transfer along the diabatic states is very unlikely.

The conclusion from this scheme is that population transfer along the ladder system $5S_{1/2} \to 5P_{3/2} \to 5D_{3/2}$ happens effectively for adiabatic negative chirp rates. Both excited states are populated. On the other hand transfer to the state $5P_{1/2}$ is very unlikely. Furthermore for adiabatic transfers there is no way for the population to stay in the ground state $5S_{1/2}$ implying that the ground state will be emptied to a great extent.

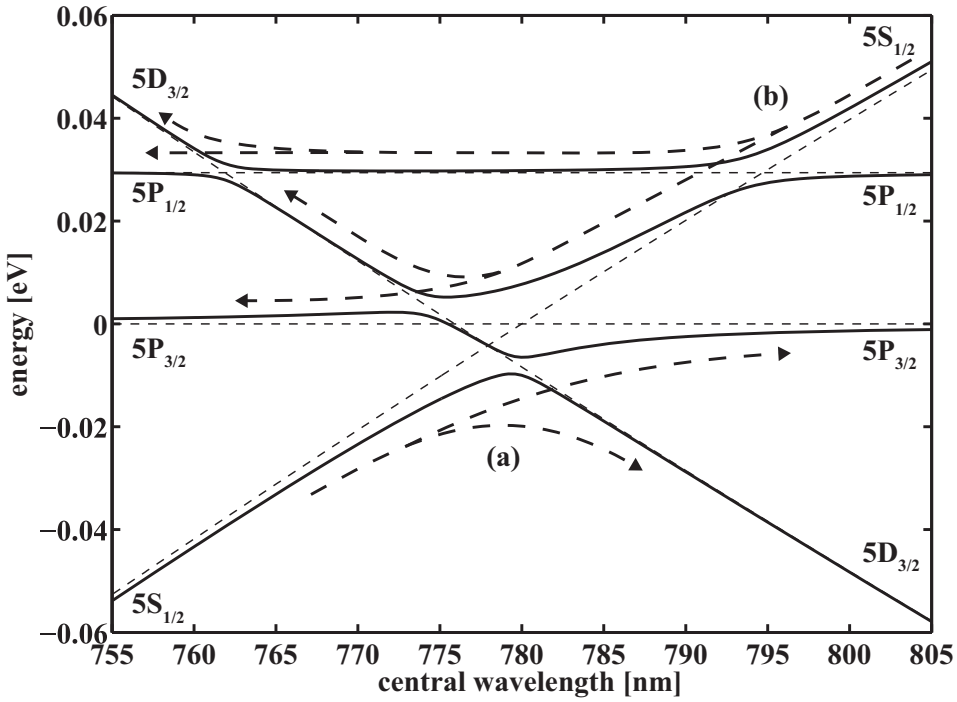

Figure 6.6: Eigenenergies of Dressed States. The solid lines show the eigenenergies for the Hamiltonian in the interaction picture in dependence of the central wavelength of the pulse. Dotted lines show the corresponding bare states.

We observe this behavior in the three chirp scans shown before. Both the scan 6.3 on 780 nm light from state $5P_{3/2}$ to the ground state and the scan 6.5 on 420 nm emission coming from the decay $5D_{3/2} \rightarrow 6P_{3/2}$ show fluorescence for negative chirps rates. The scan 6.4 for 795 nm ($5P_{1/2}$) has like predicted no superfluorescence yield.

The shifted turn on in scan 6.5 on 420 nm emission for negative chirp rates results from the fact that the system stays in the diabatic states up to higher excitation intensities than in the case of positive chirp rates.

For positive chirp rates the system follows the dashed arrow (b). Again the population starts in the ground state $5S_{1/2}$ - now at long wavelengths. At the first avoided crossing (the intersection of the diabatic states $5S_{1/2}$ and $5P_{1/2}$) the system can go along the original dressed state or pass to the neighboring dressed state. The transfer through this avoided crossing is strong for great

positive chirp rates and weak for small positive chirp rates. The following avoided crossing in the upper branch at the intersection of the diabatic states $5D_{3/2}$ and $5P_{1/2}$ is very weak as the dipole moment for the corresponding transition is small. The system can take both ways here and ends up for small wavelengths in either intermediate states $5P_{1/2}$ or excited state $5D_{3/2}$.

The lower branch splits once again at the the intersection of the diabatic states $5D_{3/2}$ and $5P_{3/2}$. For transfer to the neighboring the dressed states the system ends in the intermediate state $5P_{3/2}$. If the system follows its dressed state it retuns to the upper branch.

Consequently the system can end in both intermediate states $5P_{1/2}$ and $5P_{3/2}$ and the excited state $5D_{3/2}$. Like in the case of negative chirp rates there is no way for the population to stay in the ground state $5S_{1/2}$ for adiabatic transfer.

Here again the measurements agree with the predictions. All three scans show superfluorescence for positive chirp rates. The small yield in scan 6.3 on 780 nm emission is result from the two avoided crossings which the population has to pass. A passage to the state $5P_{1/2}$ is much easier as the avoided crossing is small. The corresponding chirp scan 6.4 on the 795 nm light shows very pronounced superfluorescence for positive chirp rates.

Sauerbrey *et al.* [31] find a similar chirp dependence in the excitation of the Rb system in their pump-probe experiment for positive and negative chirp rates. They do not observe superfluorescence but explore the population transfer with a weak probe pulse after exciting with a much stronger pump pulse. In agreement with the presented data they measure population transfer to the state $5P_{1/2}$ for positive chirp rates and to the state $5P_{3/2}$ for negative chirp rates.

6.2 Superfluorescence

The emission process from the excited states cannot be explained by the picture of a partly excited states emitting spontaneously photons. The measured light in the emission features in figures 6.1 and 6.2 has two characteristics: it is spectrally narrow and highly directional.

Two different emission mechanism explain these characteristics in ensembles of exited atoms: amplified spontaneous emission (ASE) and superfluorescence / superradiance. Both processes lead to a collective response of the system. The main difference is the degree of coherence in the phases of the

excited atoms. A study of similarities and differences of the effects has been published by Boyd *et al.* [26].

ASE is observed in incoherently excited optical media with high gain. Initially spontaneous emitted photons experience strong amplification along their way through the medium and build up light fields. The power of the emitted ASE scales with the number of atoms N. All phases of the excited atoms are randomly distributed meaning their dipole moments oscillate without any relation in respect to each other. Summing over all dipole moments yields a vanishing macroscopic dipole moment. The beam can be regarded as accumulation of spontaneous seeded and stimulated amplified light fields. Hence its temporal coherence is smaller than in processes starting with a single seed.

For media with a large aspect ratio the resulting beams can have significant spatial coherence. Photons with k-vectors along the long axis of the medium undergo high amplification without seeing any absorption. All photons with off-axis k-vectors run out of the gain region and experience strong absorption. Consequently forward and backward amplified beams dominate the process. Allen and Peters have studied various ASE attributes in their paper series starting with [33]. The threshold condition for the lowest density N_0 to observe the effect is derived to be

$$N_0 = \frac{8\pi\Delta\nu_D\,\tau_l}{3L\lambda^2\alpha} \tag{6.2.1}$$

with the lifetime of the excited state τ_l, the Doppler broadened line width $\Delta\nu_D$, the length of the active region L, the emission wavelength λ and the branching ration α. It cannot be regarded as sharp threshold but is rather diffuse.

Dicke [13] and Rehler and Eberly [35] have calculated many attributes of superradiance and superfluorescence. It occurs if the atoms are excited coherently. The first spontaneously emitted photons couple the atoms in the gain region and rearrange their phases. This synchronization of their phases can only take place if the rearrangement happens faster than the dephasing mechanisms. Hence the ensemble of atoms develops a macroscopic dipole moment. The following collective emission releases a strong and short pulse of spatial and temporal coherent light. Its time duration τ_{SF} and delay time τ_D are given in [26]. For many systems the delay time is in the ps-range implying that the superfluorescence pulse already starts to propagate while the short excitation pulse still passes through the medium.

In contrast to ASE the superfluorescence power scales with the square of the number of atoms N^2. Its peak intensity is higher and its pulse duration

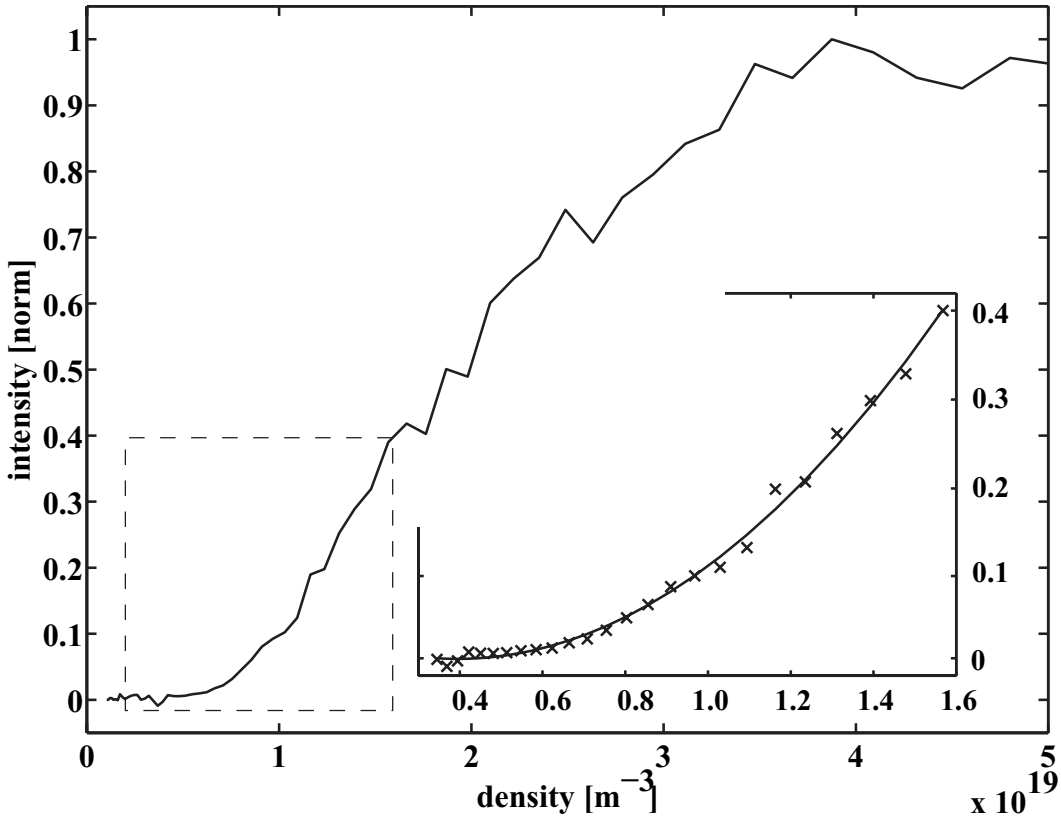

Figure 6.7: Superfluorescence Intensity vs. Density. The emission of light on the $5S_{1/2} \rightarrow 6P_{3/2}$ transition at 420 nm starts at a threshold density of about $0.4 \cdot 10^{19}\,\mathrm{m}^{-3}$. The dependence is quadratic up to a density of $1.6 \cdot 10^{19}\,\mathrm{m}^{-3}$ (see inset for quadratic fit). Higher densities show a saturation.

much shorter. Due to its time delay and the synchronized phases the superfluorescence usually propagates just into excitation direction but not backwards.

In our experiment a beam with diameter 440 μm excites a 60 mm long region in the Rb cell. Consequently the aspect ratio of the gain region is 1:136. This value is suitable for both mechanisms to produce highly directional beams.

Figure 6.7 shows the dependence of the amount of light from the $5S_{1/2} \rightarrow 5P_{3/2}$ transition at 420 nm as a function of the cell density. The blue beam coming out of the cell is filtered with a red blocking and blue transmitting filter[2]

[2]BG39

and measured with a photodiode. A thermocouple reads the temperature from which the density is calculated with equation 5.1.1. The blue light at 420 nm is just observed in the forward direction.

Assuming that the threshold condition 6.2.1 holds true for both ASE and superfluorescence we calculate a minimal density of $N_0 = 0.24 \cdot 10^{19}\,\mathrm{m}^{-3}$. The graph starts to be nonzero from a value of about $0.4 \cdot 10^{19}\,\mathrm{m}^{-3}$. Given a fairly large uncertainty in this number and the threshold condition being slightly diffuse both values agree.

In the density region between $0.4 \cdot 10^{19}\,\mathrm{m}^{-3}$ and $1.6 \cdot 10^{19}\,\mathrm{m}^{-3}$ the curve is fitted well with a quadratic function (see inset). For higher densities the curve shows a saturation effect. One possible explanation might be that the used photodiode works a non-linear region.

Likewise there is the possibility of being limited by the amount of photons. For high densities the number of resonant photons in the light field is much smaller than the number of gas atoms in the active region of the cell than. In this case a further increase of the density would not show the N^2 dependency but a saturation.

The measurements indicate that we have observed superfluorescence ans not ASE. A measurement of the temporal characteristics is not possible. The ps-regime is not accessible with photodiodes as their rise and fall times are too slow. The FROG however is limited by the stepper motor and does not work reliable for longer times than 10 ps.

Apart from the effect of superfluorescence figures 6.1 and 6.2 imply another interesting detail about the system. For any kind of lasing the population of the medium has to meet the inversion condition. All three emission features happen along transitions to the ground state $5S_{1/2}$ implying that this state has lower population than the intermediate states $5P_{1/2}$, $5P_{3/2}$ and $6P_{3/2}$. Trallero [45] has demonstrated in a similar atomic system in Na a threshold of 0.66 for the population of the upper level of the superfluorescence transition. We presume that this condition is close to the condition for Rb. As seen in the previous section these high transfer efficiencies are best achieved with chirped pulses.

There is no superfluorescence observed at the transitions from the excited state $5D_{3/2}$ to the intermediate states $5P_{1/2}$ and $5P_{3/2}$. The explanation is that the mechanism distributes the population among the states such that the population condition is not met. Figures 6.3 and 6.4 indicate significant population in the corresponding states $5P_{1/2}$ and $5P_{3/2}$. State $5D_{3/2}$ is not populated highly enough to show superfluorescence.

In the case that all resonant light from the excitation pulse has been absorbed the following superfluorescence could maximal be as intense as the resonant excitation light. Hence the absorption line in the excitation spectrum could at most be completely filled with light from the superfluorescence.

In contrast to this we find peaks at the transition frequencies. The spectral density in the peaks in figure 6.1 is at least 20% higher than in the excitation light. This phenomena is proof for non-resonant absorption for short pulses with following ressonant emission. It leads to redistribution of frequencies. Especially feature (b) in figure 6.1 illustrates how frequencies in the neighboring surroundings of the transition are absorbed and emitted at the transition frequency.

Chapter 7

Future Work

7.1 Future Work on EIT

The chapter 5 about EIT in Rb has left several questions. One problem we encountered during interpretation of the measured data was the influence of propagation effects. As soon as the system not only absorbs photons but also puts them back into the light field the description based on two- and multi-level-atoms does not account for the reemitted light.

The physical correct description for the dynamics along the path through the cell is given by the coupled Maxwell-Bloch-equations. Basic idea behind these equations is that the Bloch equations are the equations of motion for the density matrix when interacting with a light field (see for example Metcalf [28]). In combination with the Maxwell equations they allow to determine the interplay between field and atoms. In particular they predict the changes to the field during propagation. The basic concept is explained in Boyd [8]. Solving these equations would possibly answer some of the remaining questions.

According to the physical picture in section 5.7 about the time domain picture of EIT the mechanisms gives a certain possibility to redistribute colors in a spectrum. This might lead to interesting applications. One could for example collect light from a broad spectrum and reemit in a narrow bandwidth or vice versa. The required coupling pulse has to be tailored in temporal amplitude and central frequency. A local control algorithm could possibly find simple pulse shapes in theory or a genetic algorithm pulse shapes in an experiment.

All data for the EIT experiments has been taken with a USB spectrometer with limited resolution but in real time availability. A spectrometer which can resolve the line width of the probe absorption line would give insight

into the development of the structure of the line. We have tried to use a high resolution spectrometer but encountered several problems. The first is an undetected source for noise. Maybe more problematic in general is the fact that the quality of the data of the current setup is fairly dependent on imaging the right part of the cell. The beam cannot be focused onto the spectrometer input but has to be filtered by the pinhole. The live feedback of the USB spectrometer has been very helpful for proper alignment. With the high resolution spectrometer comes no possibility to have a live feedback on the signal, hence the alignment will be tedious.

When describing the emission of blue light at 420 nm we have not paid much attention to the emission at 5720 nm because we do not have the means to detect it. A very interesting experiment in regard to this radiation and to EIT would be to characterize the behavior of a beam with both the light at 5270 nm and at 420 nm pass through a second Rb cell. The cascading emission effect may introduce a time delay between the two fields. An experiment could possibly detect EIT for the light at 420 nm in the second cell as the light at 5720 nm comes first and dresses the states of the system. Pichler *et al.* [48] have just recently demonstrated EIT for the blue light at 420 nm in Rb with a coupling field at 5720 nm. It is also possible that the superfluorescence is yoked [11] which would mean that both fields come at the same time.

The problem arising for the setup is the material of the cells. All windows of our cell are presumably made from BK7 or Pyrex®. These two glasses glass are just transparent to wavelength of 2 μm to 3 μm. Hence this experiment would need two new cell with windows transparent at 5720 nm. Sapphire is the only window material meeting this requirement.

7.2 Future Work on Broadband Excitation

The characterization of the superfluorescence has so far just been based on the dependence of the intensity on the density and the direction. A measurement of the time delay and duration would be helpful to further validate the ASE characteristics of the observed light. However the setup for the time measurement is difficult as the time scale is on the order of 10 ps to 100 ps. Fast photo diodes cannot resolve this regime. The FROG is limited by the range of the stepper motor and does not work reliable for times longer than 10 ps.

In a similar experiment on sodium (Na) [46] strong and highly directional coherent light has been observed. The atomic level scheme resembles the scheme for the blue light at 420 nm but with a non-resonant intermediate state. Photons follow the $3S \rightarrow 3P \rightarrow 4P$ ladder system and can decay back the same way to the ground state. The state $3P$ is non-resonant but the state $4P$ is two photon resonant. When decaying back along the $3S \rightarrow 3P$ transition (Na D-line) strong coherent light is emitted in the forward direction which has been characterized as superfluorescence. A direct comparison of the two systems might reveal similarities and differences in their responses.

Chapter 8

Conclusions

In this thesis we have treated the configuration and calibration of the autocorrelator GRENOUILLE, a time domain perspective on ultrafast EIT and a broadband excitation experiment.

The GREOUILLE allows the group to monitor the pulse of the amplifier in a very convenient and fast way. The device can resolve the pulses in time and frequency with a CCD camera. Certain constraints of the setup prevent from reconstructing the field in phase and time. Nevertheless the established calibration in conjunction with a LabVIEW program determines the pulse duration in real time. The mechanism is robust and does not require time consuming alignment so that the GRENOUILLE is used on a daily basis.

Our ultrafast EIT experiments provide a time domain perspective on a mechanism which has been explored in a frequency domain before. We demonstrate a complex interplay between coupling pulse, probe pulse and Rb system. The physical explanation is based on a modified two-level system approach and a phase difference evolution between field and states. Two new aspects are distinctive for the dynamics in comparison to regular EIT: a time dependent couling Rabi frequency and the interplay between absorption and stimulated emission.

It arises the question whether the measured dynamics still can be named EIT. Cons are that regular EIT is a phenomenon which is described in the frequency domain. No time domain picture and varying coupling Rabi frequency are required. Its explanation lies in the population trapped states and the shape of the susceptibility of the transition. Pros are that the spectral intensity at the transition frequency does not get reduced and the fact that the setup requires the same three-level system and probe and coupling field as regular EIT. The lack of absorption at the transition can be called transparency. It is

induced by the electromagnetic coupling field, hence the experiment matches exactly the name of electromagnetically induced transparency.

We do not want to rule in favor of one or the other at this point. The observed dynamics are different, but lead to a similar result. Thus the name of the last section has been chosen with care in regard to this question. We suggest to refer to a "time domain picture of ultrafast EIT".

The broadband excitation experiment gives detailed insight into a mostly adiabatic excitation mechanisms. We measure population transfer in a four-level system with chirped pulses. The resulting scans show significant differences between positive and negative chirp rates. A theoretical description can be given in the dressed states picture applied to chirped pulses.

The measured superfluorescence indicates that the excitation transfers presumably much more than 66% of the population from the ground to excited states. Further experiments demonstrate the characteristics of superfluorescence.

Bibliography

[1] Akturk, S., Kimmel, M., O'Shea, P., and Trebino, R. (2003). Measuring pulse-front tilt in ultrashort pulses using grenouille. *Opt. Express*, 11(5):491–501.

[2] Akturk, S., Kimmel, M., O'Shea, P., and Trebino, R. (2004). Extremely simple device for measuring 20–fs pulses. *Opt. Lett.*, 29(9):1025–1027.

[3] Arimondo, E. (1996). Coherent population trapping in laser spectroscopy. *Progress in Optics*, 35:257.

[4] Autler, S. H. and Townes, C. H. (1955). Stark effect in rapidly varying fields. *Phys. Rev.*, 100(2):703–.

[5] Backus, S., Bartels, R., Thompson, S., Dollinger, R., Kapteyn, H. C., and Murnane, M. M. (2001). High-efficiency, single-stage 7-khz high-average-power ultrafast laser system. *Opt. Lett.*, 26(7):465–467.

[6] Backus, S., III, C. G. D., Murnane, M. M., and Kapteyn, H. C. (1998). High power ultrafast lasers. *Review of Scientific Instruments*, 69(3):1207–1223.

[7] Boller, K.-J., Imamolu, A., and Harris, S. E. (1991). Observation of electromagnetically induced transparency. *Phys. Rev. Lett.*, 66(20):2593–2596.

[8] Boyd, R. W. (2002). *Nonlinear Optics*. Academic Press, San Diego, 2 edition.

[9] Boyd, R. W. (2008). *Nonlinear Optics*. Academic Press, San Diego, 3 edition.

[10] Broers, B., van Linden van den Heuvell, H., and Noordam, L. (1992). Efficient population transfer in a three-level ladder system by frequency-swept ultrashort laser pulses. *Phys. Rev. Lett.*, 69(14):2062.

[11] Brownell, J. H., Lu, X., and Hartmann, S. R. (1995). Yoked superfluorescence. *Phys. Rev. Lett.*, 75(18):3265–.

[12] Buth, C., Santra, R., and Young, L. (2007). Electromagnetically induced transparency for x rays. *Physical Review Letters*, 98(25):253001.

[13] Dicke, R. H. (1954). Coherence in spontaneous radiation processes. *Phys. Rev.*, 93(1):99–.

[14] Dugan, M. A., Tull, J. X., and Warren, W. S. (1997). High–resolution acousto–optic shaping of unamplified and amplified femtosecond laser pulses. *J. Opt. Soc. Am. B*, 14(9):2348–2358.

[15] Fetterman, M., Davis, J., Goswami, D., Yang, W., and Warren, W. (1999). Propagation of complex laser pulses in optically dense media. *Physical Review Letters*, 82(20):3984.

[16] Field, J. E., Hahn, K. H., and Harris, S. E. (1991). Observation of electromagnetically induced transparency in collisionally broadened lead vapor. *Phys. Rev. Lett.*, 67(22):3062–.

[17] Hakuta, K., Marmet, L., and Stoicheff, B. P. (1991). Electric-field-induced second-harmonic generation with reduced absorption in atomic hydrogen. *Phys. Rev. Lett.*, 66(5):596–.

[18] Ham, B. S., Shahriar, M. S., and Hemmer, P. R. (1997). Enhanced nondegenerate four-wave mixing owing to electromagnetically induced transparency in a spectral hole-burning crystal. *Opt. Lett.*, 22(15):1138–1140.

[19] Harris, S. E. (1997). Electromagnetically induced transparency. *Physics Today*, 50(7):36.

[20] Harris, S. E., Field, J. E., and Imamolu, A. (1990). Nonlinear optical process using electromagnetically induced transparency. *Phys. Rev. Lett.*, 64(10):1107 – 1110.

[21] Hau, L. V., Harris, S. E., Dutton, Z., and Behroozi, C. H. (1999). Light speed reduction to 17 metres per second in an ultracold atomic. *Nature*, 397(6720):594–598.

[22] Knappe, S., Wynands, R., Kitching, J., Robinson, H. G., and Hollberg, L. (2001). Characterization of coherent population-trapping resonances as atomic frequency references. *J. Opt. Soc. Am. B*, 18(11):1545–1553.

[23] Li, Y.-q., Jin, S.-z., and Xiao, M. (1995). Observation of an electromagnetically induced change of absorption in multilevel rubidium atoms. *Phys. Rev. A*, 51(3):R1754–.

[24] Lozovoy, V. V., Pastirk, I., and Dantus, M. (2004). Multiphoton intrapulse interference. ultrashort laserpulse spectral phase characterization and compensation. *Opt. Lett.*, 29(7):775–777.

[25] Maas, D. J., Rella, C. W., Antoine, P., Toma, E. S., and Noordam, L. D. (1999). Population transfer via adiabatic passage in the rubidium quantum ladder system. *Phys. Rev. A*, 59(2):1374–.

[26] Malcuit, M. S., Maki, J. J., Simkin, D. J., and Boyd, W. R. (1987). Transition from superfluorescence to amplified spontaneous emission. *Phys. Rev. Lett.*, 59(11):1189–.

[27] Meijer, T., White, J. D., Smeets, B., Jeppesen, M., and Scholten, R. E. (2006). Blue five-level frequency-upconversion system in rubidium. *Opt. Lett.*, 31(7):1002–1004.

[28] Metcalf, H. J. and v. d. Straten, P. (1999). *Laser Cooling and Trapping*. Springer-Verlag New York.

[29] Mikhailov, E. E., Sautenkov, V. A., Novikova, I., and Welch, G. R. (2004). Large negative and positive delay of optical pulses in coherently prepared dense rb vapor with buffer gas. *Phys. Rev. A*, 69(6):063808–.

[30] Mollow, B. R. (1969). Power spectrum of light scattered by two-level systems. *Phys. Rev.*, 188(5):1969–.

[31] Netz, R., Feurer, T., Roberts, G., and Sauerbrey, R. (2002). Coherent population dynamics of a three-level atom in spacetime. *Phys. Rev. A*, 65(4):043406–.

[32] O'Shea, P., Akturk, S., Kimmel, M., and Trebino, R. (2004). Practical issues in ultra-short-pulse measurements with grenouille. *Applied Physics B: Lasers and Optics*, 79(6):683–691.

[33] Peters, G. I. and Allen, L. (1971). Amplified spontaneous emission i. the threshold condition. *Journal of Physics A: General Physics*, 4(2):238–243.

[34] Ralchenko, Y., Jou, F. C., Kelleher, D. E., Kramida, A. E., Musgrove, A., Reader, J., Wiese, W. L., and Olsen, K. (2006). Nist atomic spectra

database (version 3.1.0), available at http://physics.nist.gov/asd3. In *NIST Atomic Spectra Database, NIST Standard Reference Database Number 78*. National Institute of Standards and Technology, Gaithersburg MD, 20899. http://physics.nist.gov/PhysRefData/ASD/.

[35] Rehler, N. E. and Eberly, J. H. (1971). Superradiance. *Phys. Rev. A*, 3(5):1735–.

[36] Sautenkov, V. A., Rostovtsev, Y. V., Ye, C. Y., Welch, G. R., Kocharovskaya, O., and Scully, M. O. (2005). Electromagnetically induced transparency in rubidium vapor prepared by a comb of short optical pulses. *Phys. Rev. A*, 71(6):063804–4.

[37] Scully, M. O., Zhu, S.-Y., and Gavrielides, A. (1989). Degenerate quantum-beat laser: Lasing without inversion and inversion without lasing. *Phys. Rev. Lett.*, 62(24):2813–.

[38] Shuman, T., Walmsley, I. A., Waxer, L., Anderson, M., Iaconis, C., and Bromage, J. (1999). Real–time spider: ultrashort pulse characterization at 20 hz. *Opt. Express*, 5(6):134–143.

[39] Spence, D. E., Evans, J. M., Sleat, W. E., and Sibbett, W. (1991a). Regeneratively initiated self-mode-locked ti:sapphire laser. *Opt. Lett.*, 16(22):1762.

[40] Spence, D. E., Kean, P. N., and Sibbett, W. (1991b). 60-fsec pulse generation from a self-mode-locked ti:sapphire laser. *Opt. Lett.*, 16(1):42.

[41] Steck, D. A. (2001). *Rubidium 87 D Line Data*. PhD thesis, Los Alamos National Laboratory, Los Alamos, NM 87545.

[42] Strekalov, D., Matsko, A. B., and Maleki, L. (2005). Nonlinear properties of electromagnetically induced transparency in rubidium vapor. *J. Opt. Soc. Am. B*, 22(1):65–71.

[43] Tannor, D. (2005). *Introduction to Quantum Mechanics: A Time-Dependent Perspective*. University Science Books, Herndon, VA.

[44] Tian, P., Keusters, D., Suzaki, Y., and Warren, W. S. (2003). Femtosecond phase-coherent two-dimensional spectroscopy. *Science*, 300(5625):1553–1555.

[45] Trallero, C. A. (2007). *Strong Field Coherent Control*. PhD thesis, SUNY Stony Brook.

[46] Trallero-Herrero, C., Clow, S. D., Bergeman, T., and Weinacht, T. (2008). Strong field coherent control of atomic population transfer. *Journal of Physics B: Atomic, Molecular and Optical Physics*, 41(7):074014 (8pp).

[47] Trebino, R., DeLong, K. W., Fittinghoff, D. N., Sweetser, J. N., Krumbugel, M. A., Richman, B. A., and Kane, D. J. (1997). Measuring ultrashort laser pulses in the time–frequency domain using frequency–resolved optical gating. *Rev. Sci. Instrum.*, 68(9):3277–3295.

[48] Vdovic, S., Ban, T., Aumiler, D., and Pichler, G. (2007). Eit at $5^2s_{1/2} \rightarrow 6^2p_{3/2}$ transition in a mismatched v-type rubidium system. *Optics Communications*, 272(2):407–413.

Index